

NASA/CR—2018–220127



# **ECLSS Universal Waste Management System (UWMS) Metal Materials Compatibility Study**

## **Elgiloy: Electrochemical and Crevice Corrosion Evaluation**

*R.E. Lee*

*Jacobs ESSSA Group/Bevilacqua Research Corporation  
Marshall Space Flight Center, Huntsville, Alabama*

Prepared for Marshall Space Flight Center  
under Contract NNM12AA41C

**November 2018**

## The NASA STI Program...in Profile

Since its founding, NASA has been dedicated to the advancement of aeronautics and space science. The NASA Scientific and Technical Information (STI) Program Office plays a key part in helping NASA maintain this important role.

The NASA STI Program Office is operated by Langley Research Center, the lead center for NASA's scientific and technical information. The NASA STI Program Office provides access to the NASA STI Database, the largest collection of aeronautical and space science STI in the world. The Program Office is also NASA's institutional mechanism for disseminating the results of its research and development activities. These results are published by NASA in the NASA STI Report Series, which includes the following report types:

- **TECHNICAL PUBLICATION.** Reports of completed research or a major significant phase of research that present the results of NASA programs and include extensive data or theoretical analysis. Includes compilations of significant scientific and technical data and information deemed to be of continuing reference value. NASA's counterpart of peer-reviewed formal professional papers but has less stringent limitations on manuscript length and extent of graphic presentations.
- **TECHNICAL MEMORANDUM.** Scientific and technical findings that are preliminary or of specialized interest, e.g., quick release reports, working papers, and bibliographies that contain minimal annotation. Does not contain extensive analysis.
- **CONTRACTOR REPORT.** Scientific and technical findings by NASA-sponsored contractors and grantees.
- **CONFERENCE PUBLICATION.** Collected papers from scientific and technical conferences, symposia, seminars, or other meetings sponsored or cosponsored by NASA.
- **SPECIAL PUBLICATION.** Scientific, technical, or historical information from NASA programs, projects, and mission, often concerned with subjects having substantial public interest.
- **TECHNICAL TRANSLATION.** English-language translations of foreign scientific and technical material pertinent to NASA's mission.

Specialized services that complement the STI Program Office's diverse offerings include creating custom thesauri, building customized databases, organizing and publishing research results...even providing videos.

For more information about the NASA STI Program Office, see the following:

- Access the NASA STI program home page at <http://www.sti.nasa.gov>
- E-mail your question via the Internet to [help@sti.nasa.gov](mailto:help@sti.nasa.gov)
- Phone the NASA STI Help Desk at 757-864-9658
- Write to:  
NASA STI Information Desk  
Mail Stop 148  
NASA Langley Research Center  
Hampton, VA 23681-2199, USA

NASA/CR—2018–220127



# **ECLSS Universal Waste Management System (UWMS) Metal Materials Compatibility Study**

## **Elgiloy: Electrochemical and Crevice Corrosion Evaluation**

*R.E. Lee*

*Jacobs ESSSA Group/Bevilacqua Research Corporation  
Marshall Space Flight Center, Huntsville, Alabama*

Prepared for Marshall Space Flight Center  
under Contract NNM12AA41C

National Aeronautics and  
Space Administration

Marshall Space Flight Center • Huntsville, Alabama 35812

---

**November 2018**

Available from:

NASA STI Information Desk  
Mail Stop 148  
NASA Langley Research Center  
Hampton, VA 23681-2199, USA  
757-864-9658

This report is also available in electronic form at  
<<http://www.sti.nasa.gov>>

## TABLE OF CONTENTS

1. INTRODUCTION .....	1
1.1 Background and Summary .....	1
1.2 Polarization Concepts .....	2
2. EXPERIMENTAL .....	2
2.1 Test Sample Preparation .....	2
2.2 Procedures and Techniques .....	3
3. RESULTS OF CORROSION TESTING .....	8
3.1 Crevice Corrosion Assessment .....	8
3.2 Electrochemical Assessment .....	10
3.3 Summary and Conclusions .....	23
APPENDIX .....	24
A.1 Electrochemistry Concepts .....	24
A.2 Test Configuration and Parameter Definition .....	24
A.3 The Polarization Curve .....	26
A.4 The Butler-Volmer Equation .....	27
A.5 Faraday's Law and Oxidation Rates .....	29
A.6 Estimation of Currents and Rates .....	30
A.7 Analysis of Cyclic Polarization Curves .....	35
A.8 Semi-Log vs. Normal Cyclic Polarization Plots .....	38
A.9 Special Method for Determination of Electron Exchange Equivalents .....	40
A.10 Model Development for Pitting Rates and Penetration Depths Over Time .....	43
A.11 Increasing Solution pH Over Time .....	46
A.12 Special Method for Estimating Corrosion Susceptibilities .....	49
A.13 Passive Films as Pseudo-Capacitors and Semiconductors .....	53
A.14 Anomalies on Nickel Alloys under Extreme Test Conditions .....	54
REFERENCES .....	61

## LIST OF FIGURES

1.	Images of a (a) Gamry 3000 potentiostat test system, (b) ParStat 3000 potentiostat test unit and (c) flat test cell which can be attached to either system .....	4
2a.	Typical workstation and test cell configuration showing four Gamry 3000 ready for use.....	5
2b.	Two views of a connected Flat Test Cell containing Pretreat solution and attached test sample during a polarization test run .....	5
3.	Incremental flow sequence for polarization testing .....	7
4a.	Images with descriptions of crevice sample surfaces after six months in the test solutions .....	9
4b.	Images with descriptions of crevice sample surfaces after one year storage .....	9
5.	Linear polarization test plot and analysis for Elgiloy in Concentrated Pretreat .....	11
6.	Tafel polarization test plot and analysis for Elgiloy in Diluted Pretreat .....	12
7.	Cyclic polarization test plot with parameter descriptions for Elgiloy in Concentrated Pretreat .....	16
A1.	Simple diagram of the PAR potentiostat – and flat cell connections used in this project .....	25
A2.	Current versus potential plot for one of the Cronidur samples showing anodic and cathodic branches .....	26
A3.	Linear polarization test plot and analysis for Hastelloy C276 in Concentrated Pretreat .....	32
A4.	Semi-log Tafel polarization test plot and analysis for Titanium 6Al-4V in Diluted Pretreat .....	33
A5.	Possible pathways of Titanium, Chromium and Nickel in acidic solution .....	34
A6.	Cyclic polarization test results and analysis for Hastelloy in brine .....	36

## LIST OF FIGURES (Continued)

A7.	Cyclic polarization test results and analysis for Cronidur in pretreat .....	36
A8.	Method for evaluation of critical pitting and repassivation parameters using semi-log and normal plots .....	39
A9.	(a) Depth profile of the passive layer on Inconel 700 contrasting the relative metallic concentrations in the base metal and the passive oxide <sup>[11]</sup> . (b) Depth profile of the passive layer on 316 stainless steel contrasting the relative metallic concentrations in the base metal and the passive oxide <sup>[12]</sup> .....	40
A10.	Average model composition and equivalents for the Hastelloy-oxide system in acidic solution .....	42
A11.	Example of modelled pitting penetration depths and rates for Cronidur 30 and Titanium LI .....	45
A12.	Simplified depiction of passive layer formation on a chromium alloy in air .....	46
A13.	Illustration of a passivated chromium alloy a few seconds after immersion in an acid electrolyte .....	47
A14.	Illustration of a chromium alloy several minutes after immersion .....	47
A15.	Example Open Circuit Potential curve obtained from previous studies .....	48
A16.	Pitting initiation plots for three of the test metals in pretreat showing the respective active areas .....	50
A17.	Cyclic plot for Titanium LI showing possible relationships between conductivity and susceptibility .....	51
A18.	Cyclic plot for Cronidur 30 showing possible relationships between conductivity and susceptibility .....	51
A19.	Possible reactions for a chromium substrate leading to conduction, oxide production and dissolution. Cr = metal atom in base metal, $V_{Cr}^{3-}$ = cation vacancy in oxide lattice, $Cr_{Cr}$ = metal cation at cation site in oxide lattice, $v_{Cr}$ = vacancy in base metal, $Cr_i^{3+}$ = interstitial cation in oxide lattice, $Vo^{\bullet\bullet}$ = oxygen vacancy in oxide lattice, $Cr^{6+}$ (aq) = fully oxidized metal cation in solution, $O_o$ = oxygen anion in oxygen lattice, and $CrO_{3/2} = \frac{1}{2} Cr_2O_3 = Cr_{Cr} + 1\frac{1}{2} Vo^{\bullet\bullet}$ .....	53

## LIST OF FIGURES (Continued)

A20.	Hastelloy sample surface after cyclic polarization scan in pretreat with $-0.75V$ cathodic conditioning .....	54
A21.	Illustration of possible polarization paths during and after primary passivation .....	57
A22.	Illustration of possible processes during anodic passivation of Ni-Cr alloys under reverse bias .....	58
A23.	Cyclic polarization scan for the anomalous Hastelloy sample shown in Figure 35 ....	59



## LIST OF TABLES

1.	Reduced Data Summary for Linear and Tafel Polarization Analysis .....	13
2.	Reduced Data Summary for Cyclic Polarization Analysis .....	18
3.	Summary of Special Factors and Correlation Ratios for Cyclic Polarization Analysis .....	19
4.	Reduced Data Summary for Galvanic Coupling Evaluations .....	22
A1.	Average representative values utilized for $\epsilon_r$ and $\Delta E_f^0$ during estimation of relative susceptibilities .....	52



## CONTRACTOR REPORT

### ECLSS UNIVERSAL WASTE MANAGEMENT SYSTEM (UWMS) METAL MATERIALS COMPATIBILITY STUDY ELGILOY: ELECTROCHEMICAL AND CREVICE CORROSION EVALUATION

#### 1.0 Introduction

#### 1.1 Background and Summary

On the ISS, potable water is generated from the ECLSS module as waste liquids are ‘pretreated’ with an acid stabilizer formula in a process that ultimately leads to the recovery of about 75-85% of the water. ECLSS construction materials must withstand long-term exposures to these solutions. A Mid-Term Briefing was provided in March 2018 covering information that was available at that time. This Final Report can be considered as a concluding extension to that effort.

In this work, the entire set of electrochemical and crevice corrosion test results are presented for samples of the metal Elgiloy which comprises the fourth candidate in this UWMS series of evaluations. The three metals tested previously included Inconel 625, Hastelloy C276 and Titanium 6Al-4V in which all three were demonstrated to be distinctly corrosion-resistant and quite compatible with each other in the subject test solutions. All four candidates have now been evaluated in the two acidic test solutions which are being proposed as alternatives to the existing formulations for pretreatment of ECLSS waste liquids. Test methods consisted of general and localized corrosion evaluations utilizing DC polarization, including Linear, Tafel, Cyclic and Galvanic Coupling analysis with reference to ASTM G102. Crevice evaluations utilized double plate, sandwich-type assemblies simulating both parallel and angled crevice configurations for assessing long-term performance of the metals after 6-month and 1-year immersion in both solutions. These techniques loosely follow ASM G78.

The two test solutions for this study consisted of:

- (1) ~25% chromic acid (w/w) + ~55% phosphoric acid (w/w) which is identified as ‘concentrated alternate pretreat stabilizer solution’.
- (2) ~7% solution of the concentrated solution (v/v) which is identified as ‘diluted alternate pretreat stabilizer solution’.

Mid-Term results for Elgiloy revealed no visible signs of corrosive activity or electrochemical tendencies associated with general corrosion, pitting or crevicing for any of the metals in either of the test solutions. This final synopsis provides additional support to the Mid-Term evaluations as the results have fully demonstrated that Elgiloy, along with the previous three metals, is very resistant to general and localized corrosion, and is also galvanically compatible with each other metals in both solutions. This was clear throughout the electrochemical evaluation as no surface anomalies or unusual behavior were indicated throughout the testing phase. The final data analysis confirms these observations. The high nobilities and low corrosion susceptibilities apparent for these four metals are in accordance with their established positions indicated in most Potential and Galvanic Series published throughout the literature. All four of these metals spontaneously form tenacious, self-repairing, passive oxide layers on their surfaces which provide extraordinary nobility and protection in very corrosive environments. These naturally-forming oxide layers are exclusively responsible for their superior corrosion resistance.

## **1.2 Polarization Concepts**

Whenever the potential (voltage) and electric current (or current density) are measured and evaluated together, the potential becomes an indication of nobility with respect to the tendency, probability or susceptibility for corrosion to occur. The current is directly proportional to the rate of oxidation, a quantity which can be converted into units indicating how fast the base metal is recessing *and* how fast the oxide thickness is changing. In most cases, base metal recession (etching) and oxide growth (passivation) are mutually inclusive processes. A high breakdown potential infers high nobility with low susceptibility to corrosion, while a large pitting current indicates a high pitting rate. A high corrosion potential typically implies a high susceptibility to general corrosion while a high repassivation current indicates a robust oxide-restoration and recovery process (repassivation) which is ready to ‘kick into gear’ the moment the oxide layer is breached.

## **2.0 Experimental**

### **2.1 Test Sample Preparation**

#### **2.1.1 Machining and Finishing of Test Samples**

All test samples were machined from bulk metal stock into approximately 3' X 3" X 1/2" plates. This size was deemed appropriate for all of the polarization, galvanic and crevice corrosion testing as mandated by the ECLSS project to satisfy the requirements for evaluating the performance and compatibility of each metal candidate of interest. All the metal samples were degreased, rinsed and dried, and then liberally rinsed with DI water, solvent rinsed and air dried in ambient atmosphere (68-72°F and 30-40% R.H.) to promote natural development of their native surface oxide layers prior to testing.

#### **2.1.2 Crevice Sample Assembly Configuration**

Samples for evaluating crevice corrosion effects were assembled in two different configurations. Even though the procedure loosely followed ASTM G78, the specific test approach utilized throughout these studies was developed in-house at Marshall Space Flight Center several years back.

##### **Angled Crevice Sample Configuration**

Sandwich-type assemblies consisted of two sample plates clamped together and separated by a small rectangular-shaped, single layer of filter paper near one side of the clamped assembly to create a tiny *angled crevice gap* between the two plates.

##### **Parallel Crevice Sample Configuration**

Sandwich-type assemblies consisted of two sample plates clamped together and separated by a larger square-shaped, single layer of filter paper centered in the assembly to create a tiny *parallel crevice gap* around the edges between the two plates.

## **2.2 Procedures and Techniques**

### **2.2.1 Crevice Corrosion Evaluations**

Test assemblies of all three metals were immersed in each of the two test solutions for up to one year. Samples were monitored periodically throughout. Half of the samples were removed after 6 months storage and were carefully cleaned and evaluated. At the end of the one year period, the other half was removed, cleaned and evaluated. After removal from the test solutions and thorough rinsing, each sample was subjected to visual and microscopic evaluation to check for signs of corrosion, surface growth, pitting, base metal degradation and/or any anomaly of relevance.

### **2.2.2 Polarization Workstations and Equipment**

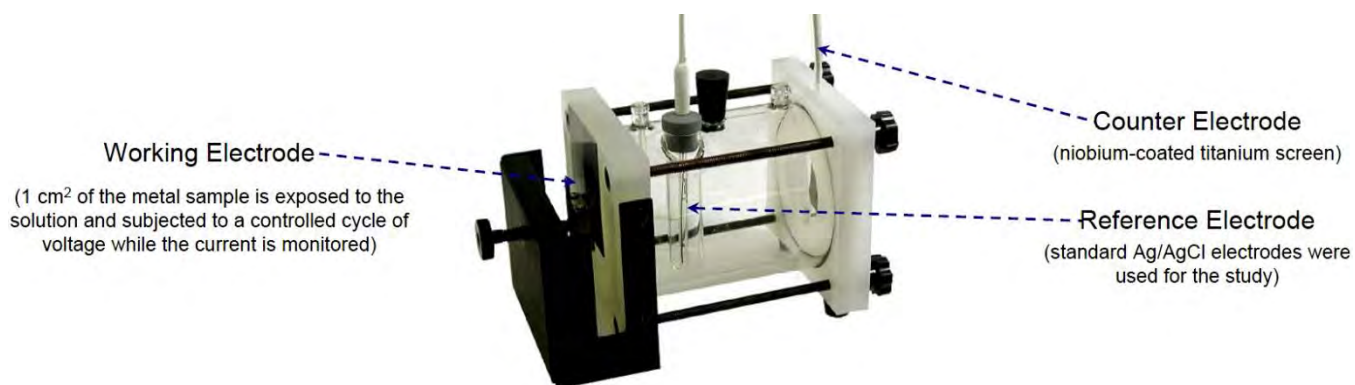
Electrochemical measurements were carried out utilizing computer-controlled potentiostat workstations supplied by Gamry Instruments and Princeton Applied Research (PAR). Four Gamry 3000 models and two PARSTAT 3000's were available throughout the study. Both of these systems included their own proprietary software for data collection and analysis. Test solutions and metal samples were accommodated using Flat Test Cells throughout the project which included 1 cm<sup>2</sup> exposure holes on one end for polarization routines and 1 cm<sup>2</sup> exposure holes on both ends for galvanic coupling. Reference electrodes bases on Ag/AgCl were used throughout these studies. The equipment, experimental configurations and workstations are depicted in Figures 1 and 2 below.



(a) Gamry 3000



(b) ParStat 3000



(c) Flat Test Cell

Figure 1: Images of a (a) Gamry 3000 potentiostat test system, (b) ParStat 3000 potentiostat test unit and (c) flat test cell which can be attached to either system.



Figure 2a: Typical workstation and test cell configuration showing four Gamry 3000 ready for use.

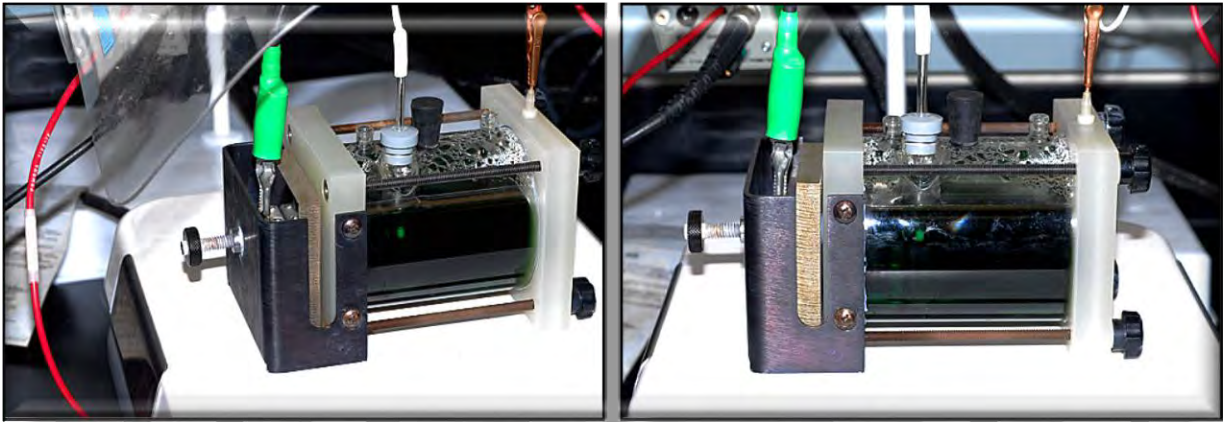


Figure 2b: Two views of a connected Flat Test Cell containing Pretreat solution and attached test sample during a polarization test run.

The flat cell offers flexibility for a variety of DC electrochemical studies including Open Circuit, Linear, Tafel, Cyclic polarization and Galvanic Coupling measurements. For Galvanic Coupling tests, the cell is re-assembled using a second 1cm<sup>2</sup> sample area end-cap for the other metal so that both samples are connected across the test solution. The second metal is grounded and interacts with the first metal which is monitored for voltage and current changes.

### 2.2.3 DC Polarization Test Descriptions

Electrochemical test descriptions employed for these studies are given below.

Open Circuit Analysis (OCP) – Nondestructively measures the steady state open circuit potential  $E_{OC}$  as a single metal is exposed to the solution over time with no power applied. Provides potentiostatic information regarding the relative nobility of a metal in terms of its open circuit voltage while being exposed to the test solution under static, nonpolarizing conditions.

Linear and Tafel Polarization – Nondestructively measures the resulting current response when a very small voltage is applied relative to the OCP. Provides the corrosion resistance  $R_{Cor}$ , corrosion current  $I_{Cor}$ , the beta Tafel parameters and the corrosion rate  $k_{Cor}$ . These results provide indications regarding the propensity for general corrosion to occur under steady state conditions. A very small, voltage ramp is applied from the cathodic region to the anodic region under slightly polarizing conditions ( $\pm 20$ -200mV)

Cyclic Polarization – Measures the resulting current response over a wide voltage range with possible sample surface alterations. Provides potentiodynamic information regarding corrosion tendencies when the metal is exposed to the test solution while a complete voltage loop is applied from a preselected cathodic point across the entire anodic region. The ramp takes the metal beyond its Tafel zone and through its breakdown potential  $E_{Brk}$  to a preselected ‘vertex’ potential and then back down through the repassivation zone. A hysteresis loop is usually generated. Pitting phenomena, passive oxide growth and oxide destabilization as well as repassivation protection and recovery mechanisms are explored. Supplemental general corrosion information may also be obtained from cyclic polarization data.

Note: For clarity, it should be realized that the microstructures comprising the passive oxides on these metals are not always damaged catastrophically at  $E_{Brk}$ , but rather their electrical insulation properties undergo a rapid transformation as resistance drops off and conduction increases across the layer possibly allowing external corrosive agents to interact directly with the metal surface which could lead to pit initiation. This is due to the rapid increase in the mobility of charge carriers near  $E_{Brk}$ . As the voltage is further increased, tunneling of the electrons may occur and then at some point beyond  $E_{Brk}$ , the oxide structures may physically fail while the fractured remnants begin dissolving in the test solution.

Galvanic Coupling – Nondestructively measures the steady state galvanic potential  $E_{OCG}$  and galvanic current  $I_g$  as two metals interact across the test solution under open circuit conditions with no power applied. Provides information regarding changes in nobility (potential) and passivation response (via current) for the test metal relative to a counter metal in a simulated galvanic couple situation.

Many researchers may include, in their testing strategy, a cathodic conditioning step on the sample prior to or at the beginning of the test run by starting the scan at a potential far below the pre-measured open circuit potential (OCP). The effect of such conditioning is to cathodically strip the existing native oxide layer from the metal surface and then allow a new passive layer to form within the solution. This newly-formed (solution-driven) oxide layer may be very similar to the air-formed coating, but it is not necessarily the same. The intent of these current studies is to evaluate the material ‘as-is’ in their post-



machining state and with their air-formed oxide layers in their original condition as this is considered to be more representative of the material that is actually utilized to assemble the ECLSS structures.

In any event, the air-formed oxide layer will tend to adapt to the new environment over the first few minutes of immersion, possibly undergoing slight changes in surface composition and/or microstructure. Since cathodic conditioning is not applied to ECLSS components prior to immersion in the ECLSS fluids on the ISS, such treatments are considered to be inapplicable and possibly misleading regarding the goals of these experiments. Alternatively, our preparation approach included vigorous rinsing steps for the samples in DI water and organic solvent followed by 24 hours of ambient air drying under controlled conditions (68°-72°F, 40-60% R.H.) in order to encourage a clean, robust natural passive layer to form on the surfaces prior to testing. When available, a few complementary test samples were intentionally subjected to negative cathodic voltages during cyclic testing as part of the overall evaluation approach in order to better understand the effects of extreme corrosive applications.

#### 2.2.4 Polarization Test Sequence

Metal candidates were subjected to the test sequence depicted in Figure 3 below. Depending on required data accuracy, 4 to 12 independent test sample areas were evaluated for each candidate metal in order to obtain the best averages possible.

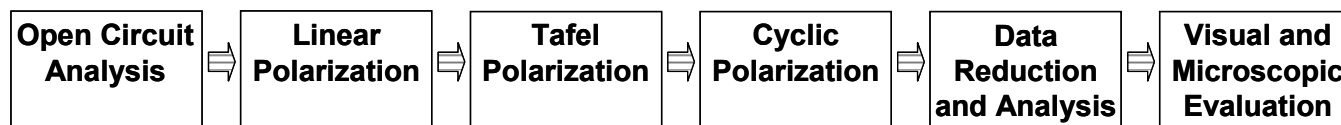


Figure 3: Incremental flow sequence for polarization testing.

#### 2.2.5 Galvanic Coupling

In this phase of the testing, test cells are mounted with two metal samples, one acting as the ‘Test’ or ‘Working’ electrode and the other as the ‘Counter’ electrode. The test assembly is allowed to sit under open circuit conditions with no power applied while the Test sample is monitored by the potentiostat for voltage and current changes as it responds to the presence of the Counter sample. For all the metals in this study, galvanic changes were very small, most being in the nano-amp ranges. Increases in either potential, current or both indicate that the test metal is anodic (less noble) to the counter metal. This generally results in a slight increase in potential relative to the test metal’s Open Circuit Potential (OCP) along with possible rate increases for base metal recession and passivation as the test metal’s self-protective mechanisms intensify (slightly). If the working metal is cathodic to the counter metal, its OCP is somewhat reduced while the rate of passivation decreases. Cathodic behavior indicates that the working metal is nobler than the counter metal as the working metal’s corrosion protection requirements are relaxed. Since no power is applied to the cell during this test, no degradation or discoloration on either of the exposed surfaces takes place (generally), at least for the four noble metals evaluated during these studies. For galvanic coupling pairs, 6 to 20 independent test runs were conducted for each metal-to-metal configuration. This included many ‘test repeats’ in order to obtain the necessary degree of accuracy throughout the averaging and analysis process.

### **3.0 Results of Corrosion Testing**

#### **3.1 Crevice Corrosion Assessment**

As described previously, test samples for each metal were stored in each of the two test solutions for 6 months and 12 month time intervals. At 6 and 12 month intervals, designated samples were removed, carefully cleaned and visually inspected under magnification. Six month test results were presented at the Mid-Term Briefing and indicated no corrosion issues. Results of the twelve month samples were visibly identical to the six month group with no anomalies noted on any sample surface for either of the test solutions. Group images showing one side of each angled and parallel sample surface for both solutions are given in Figures 4a and 4b. Since both interfaces in each double-plate assembly were identical, only one of the plate surfaces for each test assembly are shown.

The pH of each storage solution was measured at the start of the test and then after the 6 and 12 month test periods. In general, slight increases in pH were observed over time. Nevertheless, overall changes in solution pH indicated no anomalies which could be attributed to corrosion events since no corrosion was observed on any surface in any solution. Acidic solutions are generally anodic as they tend to dissolve the passive oxide. This intensifies the metal's anti-corrosion mechanisms by increasing the regeneration of protective oxide (while base metal is consumed). Observed increases in pH during exposure to the subject test solutions are due to consumption (reduction) of acidic hydrogens to form molecular hydrogen (which bubbles away) as metal ions comprising the oxide are solvated into solution. For noble metals such as these, a steady state condition is eventually established between the rates of passive layer dissolution and passive oxide regeneration. An example of this scenario is graphically illustrated in the Appendix section of this report.

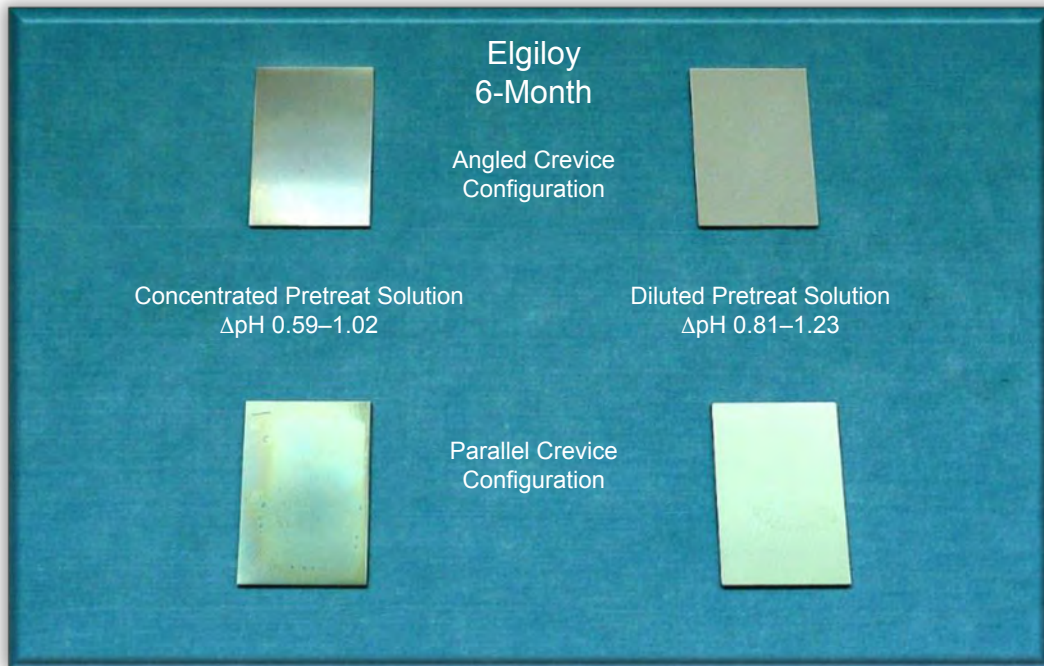


Figure 4a: Images with descriptions of crevice sample surfaces after six months in the test solutions.

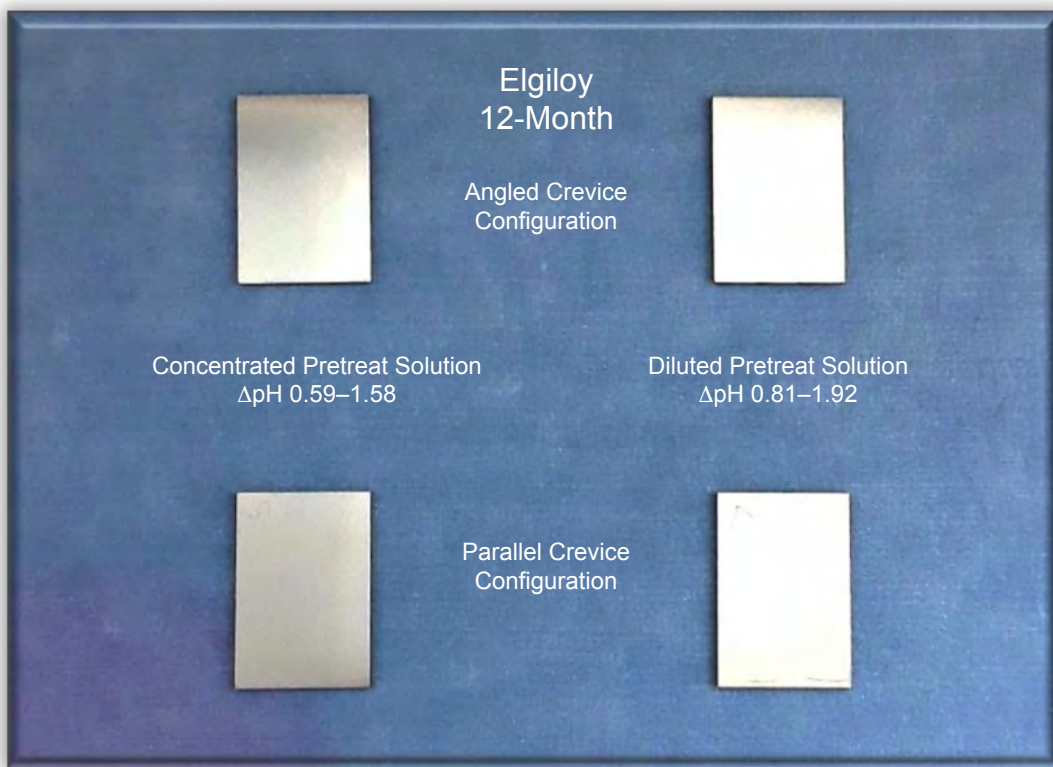


Figure 4b: Images with descriptions of crevice sample surfaces after one year storage.

### 3.2 Electrochemical Assessment

Compared to localized forms of corrosion such as pitting or crevice formation, ‘general’ corrosion or general etching involves larger or more general areas of the base metal which interact with the environment via oxidation. A classic corrosion example is the rusting of iron alloys. Industrial use of the term ‘Corrosion Rate’ refers to the rate of etching or recession into the base metal as a result of corrosive oxidation reactions occurring with the base metal producing metal oxides and hydroxide precipitates on the surface. For corroding metals, such as the low alloy steels, the oxide-hydroxide products that form on the surface are frail and structurally unorganized. These products will often spall, erode, solvate or wash away under ambient conditions. They provide no corrosion protection to the base metal.

However, for strongly passivating metals, such as the candidates under study here, the oxidation products rapidly evolve into structurally organized, semi-crystalline oxide layers which provide an astounding level of protection toward destructive oxidation. In these cases, the base metal recession depth or inward volume that is generated becomes occupied with protective oxide, preventing further exposure of the metal surface. With this understanding, the terms ‘corrosion rate’ and ‘recession rate’ may sometimes be used interchangeably for metals protected by passivation. Even though the three noble metals under study here did not undergo destructive corrosion, the base metal did recede inward a little while protective oxide growth filled the recessed volume thereby preempting sustained corrosive reactions to the metal. In short, recession rates for these metals are due to growth of the protective oxide layer rather than corrosive degradation of the base metal. All metals evaluated thus far, including Elgiloy, have indicated very strong anti-corrosion properties in both of the solutions evaluated.

In terms of base metal recession rates, all of these metal candidates appeared to be at least one order of magnitude higher than the ‘Outstanding’ rating for general corrosion which is the noblest rating recognized in the corrosion industry (i.e., Elgiloy and the other three metals exhibited very low recession rates). Overall, these findings are in good agreement with published Galvanic Series in seawater as mentioned earlier. Indeed, the corrosion-resistance properties for all of these metals was comparable to that of silver. The oxide layer associated with the titanium alloy appeared to form more rapidly and exhibit greater tenacity than the passive layers on the two nickel-chromium alloys, while Elgiloy appeared to perform better than the nickel alloys but not quite as good as the titanium candidate. It should be recognized that, in its unprotected/nonpassivated form, the galvanic activity of Titanium is almost identical to that of nonpassivated aluminum. Indeed, the superior nobility of the Titanium alloys is due exclusively to the extraordinary protective passive layer that forms on their surfaces. There is no other passivating metal readily available which produces a protective oxide layer as resilient and rapidly self-repairing as the TiO<sub>2</sub> layer on the titanium alloys.

On the whole, Open Circuit Potential, Linear and Tafel polarization pertain primarily to general (areal) corrosion effects while cyclic polarization often provides information with respect to pitting and localized corrosion events but also indicates general corrosion information in many respects as it typically supports the results obtained from Linear/Tafel analysis.

### 3.2.1 Results for Linear and Tafel Polarization

Linear and Tafel Polarization measure the current response when a small voltage scan is applied relative to the OCP. Values for the corrosion potential  $E_{Cor}$ , corrosion current  $I_{Cor}$  and corrosion resistance  $R_{Cor}$  are extracted. These data permit estimation of the Steady State time-rates for base metal recession depth utilizing Faraday's law, the Stern-Geary method and Butler-Volmer's equations. Also, with application of special estimation techniques developed uniquely for these studies, time-rates for passive oxide thickness growth can also be derived. A couple of test runs from the Elgiloy evaluations are given in Figures 5 and 6 as examples of the Linear and Tafel analyses conducted in this study.

Linear Polarization and Analysis

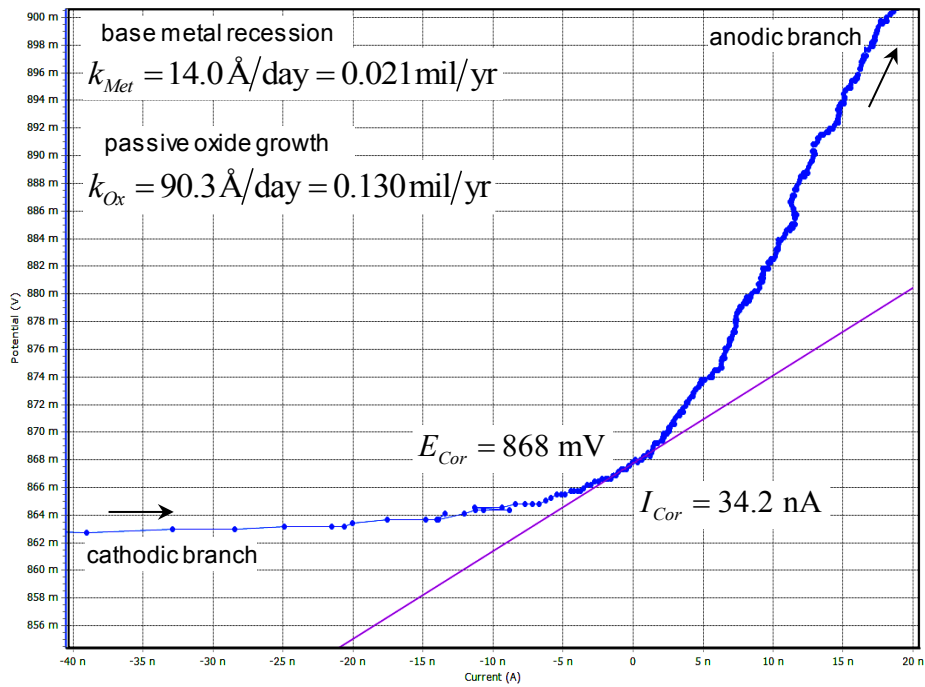


Figure 5: Linear polarization test plot and analysis for Elgiloy in Concentrated Pretreat.

\* Estimation techniques, approaches and methodologies are covered in the Appendix

## Tafel Polarization and Analysis

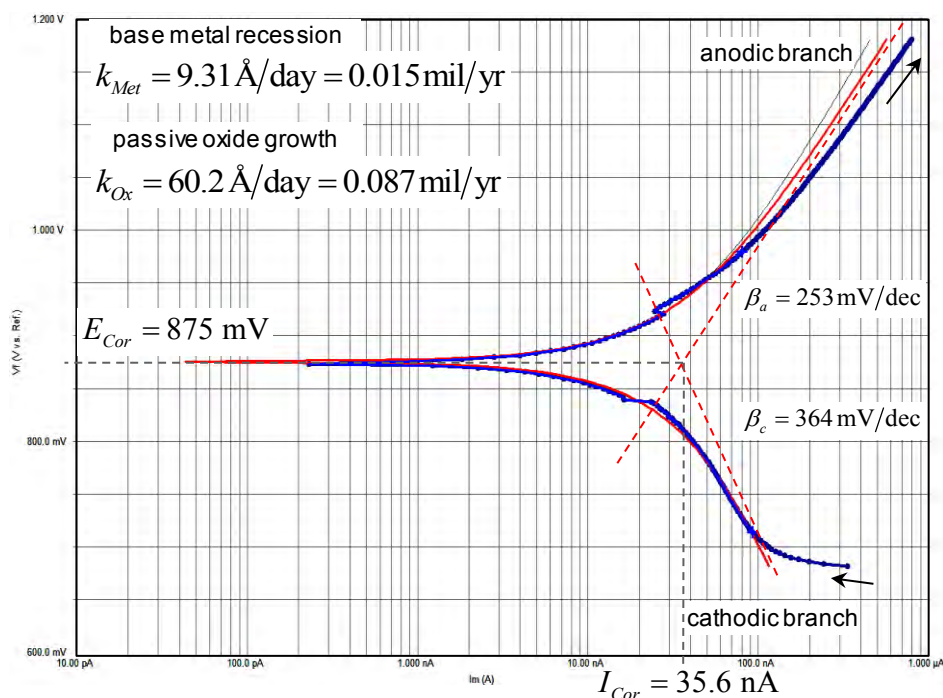


Figure 6: Tafel polarization test plot and analysis for Elgiloy in Diluted Pretreat.

In general, electrochemical potential is an indication of the tendency or susceptibility for corrosion to occur, while the current (or current density) is directly proportional to the rates of corrosion or oxidation. Under ambient, open circuit conditions, acids will very slowly dissolve the passive oxide layer as new oxide is being generated. The dissolution process continues, almost at a constant rate, during polarizing events. Again, none of the UWMS metals tend to undergo destructive corrosion but instead, their natural oxide layers grow and strengthen (consuming base metal), until adequate protection is achieved. This typically pertains to a point in which the rates of metal recession, oxide growth and oxide dissolution reach equilibrium at a stable Steady State.

In the laboratory, the actual number of polarization tests conducted per metal candidate ranged from 4 to 12 depending on the degree of accuracy needed. This approach was followed throughout in order to obtain the most representative averages for each test. These refined results were then utilized during the procedures for data reduction and consolidation, and parameter correlation. Prior to the start of the polarization testing phase, the open circuit potential (OCP) for each sample was obtained as described earlier. Table 1 provides the reduced averages and summaries covering Linear and Tafel polarization evaluations for the four UWMS metal candidates evaluated to date in the two subject test solutions. Entries for Elgiloy are highlighted in green. Results for Elgiloy were incorporated into the existing table of averages for the three previously evaluate candidates in order to compare all four metals ‘side-by-side’.

Table1: Reduced Data Summary for Linear and Tafel Polarization Analysis

**Apparent Relative Nobility**

**Depth and Thickness Rates at Steady State**

**Open Circuit Test Averages**

**Linear and Tafel Polarization Test Averages**

**Concentrated Pretreat Stabilizer Solution**

	Open Circuit Potential ( $V_{AgCl}$ )	Stabilization Period (hours)	Corrosion Susceptibility (%)	Corrosion Potential $E_{Cor}$ ( $V_{AgCl}$ )	Base Metal Recession Analogous to 'Corrosion Rate'		Passive Oxide Growth Oxide layer Strengthening	
					(Å/day)	(mil/year)	(Å/day)	(mil/year)
Titanium 6Al-4V	0.964	2.0	0.32%	0.909	10.6	0.0152	35.2	0.0506
Elgiloy	1.000	3.2	0.74%	1.062	12.2	0.0104	46.8	0.0673
Inconel 625	1.050	2.7	1.00%	1.047	13.4	0.0193	64.9	0.0933
Hastelloy C-276	1.062	2.0	1.04%	1.057	15.9	0.0228	73.7	0.1059

Ranked from lowest recession rate at  $E_{Cor}$

**Diluted Pretreat Stabilizer Solution**

	Open Circuit Potential ( $V_{AgCl}$ )	Stabilization Period (hours)	Corrosion Susceptibility (%)	Corrosion Potential $E_{Cor}$ ( $V_{AgCl}$ )	Base Metal Recession Analogous to 'Corrosion Rate'		Passive Oxide Growth Oxide layer Strengthening	
					(Å/day)	(mil/year)	(Å/day)	(mil/year)
Titanium 6Al-4V	0.522	5.9	0.35%	0.463	4.6	0.0067	15.4	0.0222
Elgiloy	0.604	7.0	0.82%	0.554	5.5	0.0054	24.3	0.0349
Inconel 625	0.611	5.4	1.14%	0.570	7.4	0.0107	35.9	0.0516
Hastelloy C-276	0.623	7.6	1.20%	0.791	6.5	0.0094	30.3	0.0436

Ranked from lowest recession rate at  $E_{Cor}$

Examination of Table 1 indicates that, overall, the properties for the four metals are comparable with each other. While the Titanium alloy appears to be slightly lower in relative nobility, the other three alloys must work harder in order to provide the same level of protection as indicated by their higher recession and passivation rates. Corrosion Susceptibilities are based on the OCP and dielectric constant of the respective passive oxide layers. Susceptibility concepts and estimation methods are covered in the Appendix. In previous studies, trends pertaining to the relative rates obtained for these same metals evaluated in pretreated ECLSS waste and solutions and brines were similar but more substantial. This was likely due the higher levels of chloride ion in these solutions which is well known for its destructive effects on passive oxide layers. On the other hand, the current test media consist only of the straight pretreat acid formulations prior to merging with the ECLSS liquids. While the lower pH of these straight solutions could negatively affect the rate of oxide dissolution, the absence of chloride ions significantly reduces the degradation effects that are associated with the waste solutions.

All in all, the results obtained in this study are reflective of metals possessing very strong anti-corrosion properties. Compared to the more active metals in the Galvanic Series, oxidation rates for these candidates are extremely small and the relative consumption of base metal due to recession (i.e. the 'corrosion rate') is minuscule. The tenacity of the passive oxide layers on these metals along with their capabilities to regenerate new oxide 'at-will' appear to be quite extraordinary. It should be noted that this data pertains to the Steady State condition when the reaction rates for metal oxidation, hydrogen reduction and oxide dissolution are all in equilibrium (after the metal has been exposure to the solution for some time). The Steady State may or may not reflect the behavior patterns under aggressive conditions when

rates are rapidly changing. The Steady State condition is more representative of static field situations when the system is in equilibrium with its surroundings. While corrosion rates are often characterized utilizing parabolic rate kinetics,  $x = (kt)^{1/2}$ , results from this studies have shown that depth and thickness time-rates due to metal recession, oxide growth and dissolution are best represented with modified Weibull functions, ex.:  $x = A(B - Ce^{-kt})^D$ , which can be empirically developed from the data. This approach is covered in the Appendix.



### 3.2.2 Results for Cyclic Polarization

Cyclic polarization is an accelerated test that can sometimes impart a certain degree of damage to the exposed sample area since it is subjected to higher anodic voltages than Linear or Tafel polarization. For most noble metals, this damage is usually not apparent when cyclic test parameters are kept within moderate ranges. However, if applied voltages are intentionally or inadvertently carried to extreme limits, observed damages may reveal oxide failure followed by etching or pitting of the base metal. None of the four metals evaluated during this study indicated any such anomalies under normal test conditions. However, for purposes of inquisitiveness, a few samples were taken to potentials well above their breakdown points in order to explore their properties under radically induced failure conditions.

Under extreme test conditions, samples of Inconel 625 and Hastelloy C276 underwent minor general etching while the Titanium and Elgiloy samples showed no damage at all. However, pitting or crevicing were not observed in any of the extreme test samples. Again, the absence of localized corrosion in the current study is attributed to the lack of halide contaminants in the particular test acids evaluated. Traditionally, traces of chloride or fluoride are leading factors for pit initiation since these ions will easily breach the passive oxide layers on all metals. During earlier projects evaluating these three particular metals in pretreated ECLSS waste and brine solutions (which were laden with halides), both pitting and etching were observed on Inconel and Hastelloy samples after extreme testing runs while again, the Titanium samples showed no surface damage even after potentials were taken to several volts above their apparent breakdown potential. Cyclic Polarization applies a complete hysteretic voltage loop to the sample surface from a starting potential that is cathodic to the original OCP, then across the primary corrosion potential, through anodic breakdown of the oxide, repassivation, recovery and finally, back down to a new stable cathodic point. A test run for one of the Elgiloy samples is given in Figure 7.

## Cyclic Polarization and Analysis

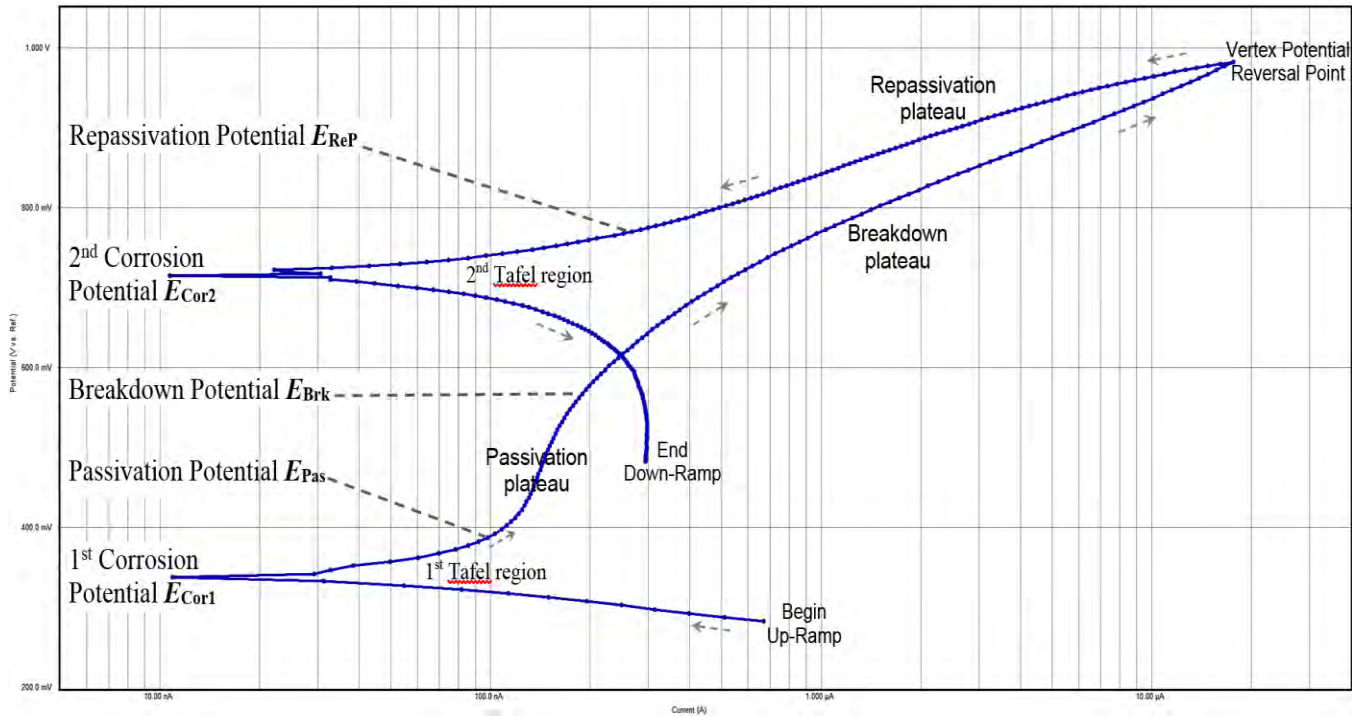


Figure 7: Cyclic polarization test plot with parameter descriptions for Elgiloy in Concentrated Pretreat.

The important test regions utilized in cyclic polarization, as indicated in Figure 7, provide the data required to fully evaluate the performance of passivating metals. These fields can be further defined to facilitate their understanding and to provide the links between the cyclic polarization data curve for each candidate and their reduced averages which will be presented later.

**First Corrosion Potential,  $E_{Cor1}$**  – Pre-breakdown equilibrium point corresponding to kinetic-dominated, low level steady state oxidation.  $E_{Cor1}$  is roughly equivalent to the original open circuit condition.

**Passivation Potential,  $E_{Pas}$**  – Point of maximum oxide growth. Transition point where reactions become diffusion-controlled while the oxide layer thickens. Marks the beginning of the 'passive plateau.

**Breakdown Potential,  $E_{Brk}$**  – Point corresponding to dielectric breakdown of the passive oxide layer. Transition point where kinetic-controlled metal recession prevails and the passive layer disintegrates.

**Repassivation Potential,  $E_{ReP}$**  – Point where repassivation subsides after recovery is complete prior to  $E_{Cor2}$ . Transition point where oxidation becomes diffusion-controlled due to regrowth of the oxide layer.

**Second Corrosion Potential,  $E_{Cor2}$**  – Post-breakdown equilibrium point corresponding to kinetic-dominated low level steady state oxidation. An elevated steady state open circuit condition that is attained at the end of the recovery process. The recovery  $E_{Cor2}$  is analogous to the ground state  $E_{Cor1}$ .

The analysis was conducted utilizing the traditional semi-log plots as shown in Figure 7 and normal plots (as indicated in the Appendix). During the first branch of the cycle shown in Figure 7, voltage is

applied at the beginning of the Up-Ramp and increases up to the Vertex Potential where the voltage begins to decrease. The First Corrosion Potential is roughly equivalent to the Open Circuit Potential measured previously. It is a stable equilibrium state in which the rates of chemical reduction and oxidation are exactly equal. Thus, the rates of base metal recession and passive oxide growth cannot be distinguished, directly measured or analytically derived at  $E_{Cor1}$ .

The Stern-Geary method is customarily used to estimate these rates and this technique is covered in the Appendix. Passive oxide growth is aggressively occurring at  $E_{Cor1}$  and beyond until the position marked as the Passivation Potential is reached (bend or elbow in the curve). At this point, oxide growth begins to level off and then becomes approximately constant along the Passivation Plateau where stable passive oxide growth occurs. As the region of Breakdown is approached, oxidation/reduction rates begin to waver while oxide stability diminishes and meta-stable pitting/etching become possible. At the Breakdown Potential, the applied voltage becomes high enough to cause the oxide to fail. Here, the protection properties of the oxide deteriorate and its microstructure may begin to disintegrate.

At and just beyond  $E_{Brk}$ , the base metal is unprotected and susceptible to attack by the solution. In some cases, this may result in obvious etching or pitting of the base metal. After the Vertex point, the potential reverses and begins to decrease along the second branch of the cycle while repassivation forces kick-in and the recovery stage begins to dominate. For the four noble metals under study, the onset of repassivation occurs almost instantly at the Vertex while re-growth of the oxide is very rapid and robust. This is indicative of the powerful protection mechanisms these metals possess. It is along this region where the maximum rate of repassivation occurs. At the point identified as the Repassivation Potential (bend or elbow in the curve on the linear plot), the recovery reactions begin to wind down as the system approaches a new stable point of equilibrium referred to as the Second Corrosion Potential. Thus, as the metal is powered up through Breakdown and Recovery, a higher point of stability is attained with respect to the original open circuit state.

As indicated in Table 2, Elgiloy, along with the three previously qualified candidates, exhibited outstanding corrosion protection properties. Nevertheless, relative to Inconel 625 and Hastelloy C276, the high Breakdown Potential for Titanium as well as its ability to repassivate rapidly when attacked, indicate a certain level superiority in terms of passive oxide protection. Elgiloy, on the other hand, appears to perform quite well relative to the two nickel-chromium alloys and generally runs a distant second to Titanium. All in all, evaluations leading to the results given in Table 2 have demonstrated that all four of these metals exhibit superior corrosion protection properties in terms of the rates for base metal recession, passivation and repassivation. These attributes are indicative of each metal's ability to counteract general and local corrosive forces by accelerating the process of passive oxide generation 'on-demand' and then rapid oxide regeneration whenever the layer is threatened by mechanical or environmental forces.

Table2: Reduced Data Summary for Cyclic Polarization Analysis

**Concentrated Pretreat**

**Concentrated Pretreat**

<b>Relative Electrochemical Potentials</b>					
	1st Corrosion Potential $E_{Cor1}$ Cathode <sup>+</sup> ->Anode <sup>-</sup> Polarity Change ( $V_{Ag/AgCl}$ )	Passivation Potential $E_{Pas}$ Diffusion Threshold ( $V_{Ag/AgCl}$ )	Breakdown Potential $E_{Brk}$ Weakening or Failure of Passive Layer ( $V_{Ag/AgCl}$ )	Repassivation Potential $E_{ReP}$ Diffusion Threshold ( $V_{Ag/AgCl}$ )	2nd Corrosion Potential $E_{Cor2}$ Anode <sup>-</sup> ->Cathode <sup>+</sup> Polarity Change ( $V_{Ag/AgCl}$ )
Titanium 6Al-4V	1.001	1.085	2.243	1.852	1.275
Hastelloy C276	0.990	1.029	1.308	1.282	1.164
Elgiloy	0.944	1.046	1.301	1.257	1.043
Inconel 625	0.978	1.010	1.241	1.130	1.087

Ranked from highest breakdown potential

<b>Rates for Metal Recession and Passivation Growth</b>										
	At $E_{Cor1}$		At $E_{Pas}$		At $E_{Brk}$		At $E_{ReP}$		At $E_{Cor2}$	
	Recession (mil/year)	Passivation (mil/year)	Recession* (mil/year)	Passivation* (mil/year)	Recession* (mil/year)	Oxide Prod* (grams/year)	Recession* (mil/year)	Passivation* (mil/year)	Recession (mil/year)	Passivation (mil/year)
Titanium 6Al-4V	0.008	0.027	0.017	0.056	0.433	0.01	0.018	0.060	0.008	0.028
Elgiloy	0.010	0.063	0.023	0.148	5.92	0.43	2.40	15.5	0.086	0.557
Hastelloy C276	0.011	0.051	0.028	0.128	37.5	1.87	66.2	307	0.142	0.660
Inconel 625	0.011	0.034	0.025	0.119	45.9	2.29	57.0	276	0.095	0.459

Ranked from lowest recession rate at breakdown

**Diluted Pretreat**

**Diluted Pretreat**

<b>Relative Electrochemical Potentials</b>					
	1st Corrosion Potential $E_{Cor1}$ Cathode <sup>+</sup> ->Anode <sup>-</sup> Polarity Change ( $V_{Ag/AgCl}$ )	Passivation Potential $E_{Pas}$ Diffusion Threshold ( $V_{Ag/AgCl}$ )	Breakdown Potential $E_{Brk}$ Weakening or Failure of Passive Layer ( $V_{Ag/AgCl}$ )	Repassivation Potential $E_{ReP}$ Diffusion Threshold ( $V_{Ag/AgCl}$ )	2nd Corrosion Potential $E_{Cor2}$ Anode <sup>-</sup> ->Cathode <sup>+</sup> Polarity Change ( $V_{Ag/AgCl}$ )
Titanium 6Al-4V	0.431	0.526	2.510	1.922	0.949
Inconel 625	0.459	0.640	1.222	1.182	0.658
Elgiloy	0.455	0.660	1.072	1.143	0.697
Hastelloy C276	0.503	0.667	1.057	1.031	0.730

<b>Rates for Metal Recession and Passivation Growth</b>										
	At $E_{Cor1}$		At $E_{Pas}$		At $E_{Brk}$		At $E_{ReP}$		At $E_{Cor2}$	
	Recession (mil/year)	Passivation (mil/year)	Recession* (mil/year)	Passivation* (mil/year)	Recession* (mil/year)	Oxide Prod* (grams/year)	Recession* (mil/year)	Passivation* (mil/year)	Recession (mil/year)	Passivation (mil/year)
Titanium 6Al-4V	0.006	0.021	0.021	0.069	1.11	0.04	0.08	0.26	0.006	0.019
Elgiloy	0.007	0.046	0.014	0.092	3.83	0.28	2.91	18.8	0.017	0.108
Inconel 625	0.008	0.041	0.027	0.129	31.8	1.59	94.3	457	0.063	0.146
Hastelloy C276	0.010	0.045	0.038	0.175	45.9	2.29	117	545	0.106	0.493

\* Approximate



Estimation techniques, approaches and methodologies are covered in the Appendix

The voltage-current hysteresis loop generated from a complete Cyclic polarization test run can reveal how well a metal either protects itself and recovers (most noble passivating metals) or fails as a result of the breakdown forces (most aluminum alloys). To supplement the evaluation, a number of special factors and correlation ratios were developed throughout these studies intended to reflect the relative performance characteristics between the candidates and to support the baseline polarization data given in Table 2. Averages of these special factors are presented in Table 3 and their descriptions follow.

Table 3: Summary of Special Factors and Correlation Ratios for Cyclic Polarization Analysis

	<b>Concentrated Pretreat</b>				<b>Concentrated Pretreat</b>		
	Area of Hysteresis (approximate) $H_A$ (mV-A)	Susceptibility for Pitting Initiation $S_I$ $f(E_{Brk}-E_{Pas}, \epsilon)$	Susceptibility for Sustained Pitting $S_S$ $f(E_{Brk}-E_{ReP}, \epsilon)$	Susceptibility General Corrosion $S_G$ $f(E_{Cor2}-E_{Cor1}, \epsilon)$	Breakdown Recovery Index $BRI$ $R_{Brk}/R_{ReP}$	General Recovery Index $GRI$ $R_{Cor1}/R_{Cor2}$	Activity Recovery Index $ARI$ $I_{Cor1}/I_{Cor2}$
Titanium 6Al-4V	-255	1.2%	0.05%	0.54%	5.53	1.31	2.86
Elgiloy	-249	7.1%	0.22%	1.85%	0.39	no data	0.48
Hastelloy C276	-44	11.7%	0.66%	2.54%	0.49	0.24	0.30
Inconel 625	-22	14.5%	0.40%	2.74%	0.43	0.43	0.21

Ranked from lowest susceptibility

	<b>Diluted Pretreat</b>				<b>Diluted Pretreat</b>		
	Area of Hysteresis (approximate) $H_A$ (mV-A)	Susceptibility for Pitting Initiation $S_I$ $f(E_{Brk}-E_{Pas}, \epsilon)$	Susceptibility for Sustained Pitting $S_S$ $f(E_{Brk}-E_{ReP}, \epsilon)$	Susceptibility General Corrosion $S_G$ $f(E_{Cor2}-E_{Cor1}, \epsilon)$	Breakdown Recovery Index $BRI$ $R_{Brk}/R_{ReP}$	General Recovery Index $GRI$ $R_{Cor1}/R_{Cor2}$	Activity Recovery Index $ARI$ $I_{Cor1}/I_{Cor2}$
Titanium 6Al-4V	-441	0.7%	0.08%	0.47%	8.48	4.77	1.39
Elgiloy	-120	5.8%	0.09%	2.22%	2.63	no data	0.98
Hastelloy C276	-64	6.0%	0.15%	3.67%	0.97	0.84	0.63
Inconel 625	-49	8.3%	0.25%	2.84%	0.94	0.61	0.81

$H_A$  indicates how well the metal recovers or succumbs after the oxide layer has failed. Negative values infer strong repassivation/recovery forces while positive values indicate poor recovery forces. All four candidates indicate negative hysteresis and exhibit unique anti-corrosion self-healing mechanisms.

$S_I$  provides a relative indication of how well the original passive layer might prevent the onset of corrosion near the breakdown point. Modified Weibull function of  $E_{Brk}$ ,  $E_{Pas}$  and  $\epsilon_r$ .

$S_S$  provides a relative indication of how well the repassivation repair mechanism might prevent sustained corrosion after breakdown has occurred. Modified Weibull function of  $E_{Brk}$ ,  $E_{ReP}$  and  $\epsilon_r$ .

$S_G$  provides a relative indication of how well the repassivation repair mechanism might prevent general corrosion after recovery at  $E_{Cor2}$ . Modified Weibull function of  $E_{Cor1}$ ,  $E_{Cor2}$  and  $\epsilon_r$ .

**BRI**: If  $> 1$ , resistance to oxide failure is enhanced as the repassivation recovery forces prevail through the breakdown point. If slightly  $< 1$ , resistance to oxide failure may be less than desirable as the recovery forces tend to struggle just after  $E_{Brk}$  but eventually take over along the repassivation plateau.

**GRI:** If  $> 1$ , resistance to general corrosion resistance may be enhanced after breakdown and recovery are complete at  $E_{Cor2}$  (analogous to anodizing). If  $< 1$ , general corrosion resistance may be lessened after breakdown and recovery.

**ARI:** If  $> 1$ , general oxidation rates may be reduced after breakdown, repassivation/recovery and stabilization are complete at  $E_{Cor2}$ . If  $< 1$ , reaction rates are stabilized but at a heightened activity level when  $E_{Cor2}$  is attained.

For the current study, hysteresis area values are only approximate since the software program did not specifically provide this capability. Susceptibility concepts were empirically-developed for these studies and are generally based on modified Weibull expressions utilizing specific potential points along the cyclic curve (as indicated in Figure 7). These formulas are also tied to the passive oxide's composite dielectric constant. Recovery index values are basically ratios of corrosion resistance or the associated current intended to reflect the relative behavior or state of the candidates following the breakdown event. Analytical and estimation methods are covered in the Appendix. The comparative indicators given in Table 3 correspond well with results from the Table 2 as they highlight the relative differences between the four metals. Again, Elgiloy, along with the other three metals exhibit strong anti-corrosion traits while Titanium appears to dominate the group.

### 3.2.3 Results for Galvanic Coupling Analysis

Galvanic interactions between dissimilar metals across a conducting solution will typically cause voltage differences and current flows that alter the relative electrochemical behavior of the metals involved. In our case, the two acid pretreat solutions were the conducting media. For galvanic coupling measurements, a metal is attached to one end of the cell and monitored for voltage and current changes as it responds to the presence of a second metal which is attached to the other end of the cell. The metal that is monitored is designated as the 'Test Metal' while the opposite metal is referred to as the 'Counter Metal'. For this test series, each metal was individually evaluated in both the 'Test' position and 'Counter' position in each solution until galvanic measurements in both directions for all four metals were accomplished. Many test repeats were conducted for each configuration. As stated previously, all four of these metals are strong passivating (self-protecting) metals so any changes observed are expected to be small. When two materials are in a coupled condition, one metal typically becomes the inferior anode of the pair as it elevates its protection mechanisms by slightly increasing its Open Circuit Potential (OCP) and/or recession/passivation rates, while the other metal behaves as the nobler cathode resulting in slight reductions in its OCP and passivation rate or no activity at all.

When an active metal at ambient is placed or forced into an anodic state galvanically or from the environment, its protection mechanisms 'kick-in', as the metal begins to generate additional protective oxide to compensate. When a nobler metal becomes cathodic, its passive layer may tend to thin out or dissolve slightly, or it may begin stripping away since its protection requirements are reduced. In some instances, when metal ions are available in the local solution whose reduction potential is greater than that of the couple *and* that of water, plating or metallization onto the cathode surface can occur (the Standard Electrode Potential for the reduction of water is  $-0.83\text{V}$ ;  $2\text{H}_2\text{O} + 2e^- \rightarrow \text{H}_2 + 2\text{OH}^-$ ). It should be noted that visual and microscopic examination of the exposed sample surfaces on all four metals evaluated in both test solutions revealed no signs pitting, recession, plating, surface growth, degradation, discoloration or any other anomalies.

When two metals are placed into a galvanic couple situation, several electrochemical processes occur simultaneously as the two metals attempt to adjust to the new conditions. Each metal attempts to approach its original (stable) Open Circuit Potential (OCP), but this is counteracted by the presence of the second metal so that ultimately, an intermediary OCP is attained which becomes the net galvanic couple OCP (GOCP). At the steady state GOCP condition, electrochemical reactions are again at equilibrium. The adjustment period may take anywhere from an hour to several days to reach a steady state plateau. During the adjustment stage, chemical and physical changes take place to the inner barrier sublayer (the primary oxide protection layer) and the outer porous hydrated layer on each metal surface. The thicknesses of these two sublayers will increase or decrease in response to the common current generated and the resultant potential field established.

In general, the rate of acid dissolution/hydrolysis of the passive oxide layers attains a relatively small and near constant value, which depends on the characteristics of the test solution (pH, ionic activity, polarity, etc.) and the properties of the oxide (solubility, type of bonding, heat of formation, etc.). Dissolution of the passive oxide layer on a metal surface takes place continuously as long as metal is in contact with an active solution regardless of whether the metal is isolated or coupled with other metals. Regeneration of new protective oxide (i.e., repassivation) and the corresponding recession of the base metal are driven by the dissolution process. The reactions of dissolution occur simultaneously and in addition to any cathodic, reduction and polarization reactions which might be taking place whenever the metal is galvanically influenced by the activity of other surrounding metals. The dissolution rate is analogous to the steady state Passive Oxide Growth rates given in Table 1 earlier in which the rates of oxide growth and oxide dissolution are in equilibrium. The currents and thus the reaction rates for passivation and dissolution are in equilibrium at the steady state.

Now for galvanic test runs where the test metal is forced into a less noble (more anodic) state under the influence of the counter metal, current is directed into the sample while electrons are flowing outward (indicated by positive current values). In these situations, the test metal is regenerating new oxide to 'keep up' with both the dissolution process and the cathodic influence of the counter metal. This is analogous to anodizing where the current-driven production of new oxide far outweighs the loss of oxide from dissolution. For cases where the test metal becomes more noble (more cathodic), current is directed out of the sample while electrons flow inward (indicated by negative current values). In these situations, the test metal needs less oxide for protection, so solution-driven oxide dissolution dominates as the oxide layer diminishes. This is analogous to cathodic stripping. These changes would be much larger for metal pairs with wide spreads between their OCPs, but due to the closeness in the nobilities for the particular metals under evaluation, all changes are expected to be relatively small. For this analysis, negative current values translate into negative rates for passivation (with no base metal recession) which implies that the oxide layer is thinning out as its protection requirements are reduced. Likewise, positive currents (and rates) imply that new oxide is being generated as the process consumes base metal which recesses inward. Table 4 gives a reduced summary of the change averages obtained during galvanic coupling analysis.

Table 4: Reduced Data Summary for Galvanic Coupling Evaluations

Changes in Nobility, Base Metal Etching and Corrosion Protection Relative to Open Circuit Conditions												
Potential	Recession	Passivation	Potential	Recession	Passivation	Potential	Recession	Passivation	Potential	Recession	Passivation	
$V_{AgCl}$	mil/year	mil/year	$V_{AgCl}$	mil/year	mil/year	$V_{AgCl}$	mil/year	mil/year	$V_{AgCl}$	mil/year	mil/year	
<b>Concentrated Pretreat</b>												
Test Metal →	Inconel 625			Hastelloy C276			Titanium 6Al-4V			Elgiloy		
↓ Counter Metal ↓												
Inconel 625	⊗	⊗	⊗	-0.0077	0.0000	-0.0517	-0.1076	0.0000	-0.1082	-0.0998	0.0000	-0.0489
Hastelloy C276	0.0028	0.0067	0.0325	⊗	⊗	⊗	-0.0821	0.0000	-0.1681	-0.0148	0.0105	0.0682
Titanium 6Al-4V	0.0803	0.0228	0.1103	0.1273	0.0257	0.1192	⊗	⊗	⊗	0.0052	0.0083	0.0538
Elgiloy	0.0303	0.0062	0.0302	0.0023	0.0129	0.0597	-0.0081	0.0000	-0.0128	⊗	⊗	⊗
<b>Diluted Pretreat</b>												
Test Metal →	Inconel 625			Hastelloy C276			Titanium 6Al-4V			Elgiloy		
↓ Counter Metal ↓												
Inconel 625	⊗	⊗	⊗	-0.0096	0.0000	-0.0537	-0.0776	0.0000	-0.0452	-0.0543	0.0000	-0.0051
Hastelloy C276	0.0079	0.0000	-0.0281	⊗	⊗	⊗	-0.0476	0.0000	-0.1072	-0.0043	0.0000	-0.0494
Titanium 6Al-4V	0.0544	0.0185	0.0895	0.0954	0.0207	0.0961	⊗	⊗	⊗	-0.0002	0.0005	0.0030
Elgiloy	0.0289	0.0008	0.0039	0.0380	0.0202	0.0936	0.0109	0.0000	-0.0132	⊗	⊗	⊗

Recall that currents are a measure of the rates associated with the chemical oxidation and reduction reactions occurring during the corrosion process, which are then converted into dimensional rates representing growth of the passive oxide layer and corresponding recession of the base metal as metal atoms undergo oxidation. In short, positive rates reflect metal recession and oxide growth while negative rates indicate dissolution of oxide. In cathodic states, oxide loss may occur but these reactions are not accompanied by any metal thickness changes so recession rates are treated as zero.

**Potential Shifts:** Negative potential shifts imply that the Test Metal is noble (cathodic) to the Counter Metal as the Test Metal relaxes its defense mechanisms. Positive potential shifts imply that the Test Metal is inferior (anodic) to the Counter Metal as the Test Metal increases its defense mechanisms.

**Rate Shifts:** Negative rate shifts imply that the Test Metal is less active than the Counter Metal as the Test Metal relaxes its rate of passivation (no recession of the base metal occurs). Positive rate shifts imply that the Test Metal is more active than the Counter Metal since the Test Metal increases its rates for passive oxidation and base metal recession as more protection is required.

Overall, potential and rate (or current) shifts were quite small, generally being in the milli-volt and nano-inch ranges. It should be noted that these changes are often within the margin of error so in many cases, galvanic differences between the metals are essentially insignificant or irrelevant. They are well within the 250mV limit provided in Table 2 of NASA-STD-6012 (there was less than 0.1V total range in potential difference all around). In conclusion, Galvanic Coupling analysis has demonstrated that Elgiloy and the other three metals are all compatible with each other as the data reveals only minute shifts in potential and oxidation rates for each metal when paired up (coupled) with each of the other metals, one at a time. The Titanium alloy seems to be the most noble of the four candidates in both solutions while Elgiloy appears to outshine Inconel 625 and Hastelloy C276.



### **3.3 Summary and Conclusions**

#### **Crevice Corrosion Evaluations:**

Visual and microscopic examination revealed no signs of pitting, crevicing, corrosion, surface growth, discolorations, patterns or surface anomalies on any surface of the angled or parallel plate test assemblies for any of four subject test metals (including Elgiloy) in either of the subject test solutions after 6-month and 12-month immersion/storage at ambient conditions.

The appearance of all sample surfaces was essentially identical to their respective surfaces prior to immersion. Also, neither of the test solutions indicated any signs of metal dissolution. Since these metals generally produce colored ions in solution, this would be further evidence that acid etching of the metal surface did not occur either locally or generally after long-term exposure to these solutions.

#### **Potentiostatic Polarization Evaluations:**

Linear and Tafel polarization tests indicated that Elgiloy (as well as all three of the previous metals evaluated) exhibited corrosion-resistance properties that were in the 'Outstanding' category according to industry standards. Cyclic polarization analysis revealed no tendencies for pitting or etching on Elgiloy or any of the other metal candidates under standard testing conditions. The Titanium alloy appeared to be the best performer of all four candidates in terms of resistance to passive oxide breakdown and regeneration of the passive layer while Elgiloy exhibited corrosion protection properties that appeared to be superior to the two nickel alloys.

Thus, it has been demonstrated that the general anti-corrosion protection properties, mechanisms for passivation, self-healing repassivation and breakdown recovery back to a stable protective state are exceptional for Elgiloy and the other three metals in both test solutions. These results correspond well with their established nobilities for various corrosive media.

For the subject acid pretreat formulations evaluated, depth and thickness rates for base metal recession and passive oxide growth appeared to be lower than those evaluated in previous studies at MSFC examining chloride-adulterated ECLSS pretreated waste liquids and brine solutions. Note: While the current test solutions were very strong acids with low pH, they are halide-free and chromium-rich. Lack of halide precludes environmental oxide breakdown while chromium ions may tend to enhance regrowth activity of the passive layer under certain conditions.

#### **Galvanic Coupling Evaluations:**

Galvanic Coupling analysis revealed that Elgiloy is compatible with all three of the metal candidates evaluated previously in both test solutions. Changes in galvanic potential and oxidation rate (shifts relative to their original open circuit values) were very small, indicating strong compatibility attributes. These conclusions support the fact that all four metals are very close to each other at the upper end of the Galvanic Series.

# Appendix

Please note that the content provided in this Appendix may be based on current and/or previous testing programs at MSFC for ECLSS which may include examples depicting metal candidates evaluated in studies other than the current project. This is done for expediency in order to representatively present the particular concepts of relevance. The intent in this section is to focus on the analytical, statistical and theoretical techniques which have been applied throughout all of these studies and may not necessarily be specific to the exact metals evaluated in the current study. Many approaches and estimation practices were taken from established methodologies and standard technical resources while some were uniquely developed for these studies over the course of ECLSS testing at MSFC during the last several years.

## A.1 Electrochemistry Concepts

The following summary represents the classical methodology employed throughout the industry and academia regarding the analysis of polarization data and the principles which have established to understand and evaluation polarization-induced corrosion phenomena. These same principles and experimental approaches have been utilized throughout all the studies conducted at MSFC.

## A.2 Test Configuration and Parameter Definition

For the situations of interest here, anodes refer to positively charged sites on the electrode (the test metal) which attract anions, while cathodes refer to negatively charged sites which attract cations. Oxidation reactions occur at the anode sites as electrons are extracted into the solution causing the sites to become positive, while reduction reactions take place at cathode sites leading to negatively charged sites. Anodes invite oxidation processes such as anodizing, passivation and rust, while cathodes invite reduction reactions which promote metal deposition and chemical reduction of the oxide as it cathodically dissolves in the solution. Thus, during electrochemical reactions, electrons flow from anodic sites to cathodic sites while electric current flows from cathodic sites to anodic sites. Once the electrical double layer (EDL) forms, anodic surfaces become negative due to the accumulation of departing electrons at the solution interface while the local interfacing solution becomes more positive as a result of dissolved metal ions.

On a larger scale, a common three-electrode test configuration was employed for this study in which electrons are supplied by the potentiostat to a counter electrode (comprised of platinum). The counter electrode polarizes the working electrode (the test sample), causing oxidation at that electrode which loses electrons to the solution. This results in an overvoltage between the working electrode and a selected reference electrode placed in close proximity to the working electrode surface. A simplified diagram of the current-voltage measurement configuration used in this work is provided in Figure A1.

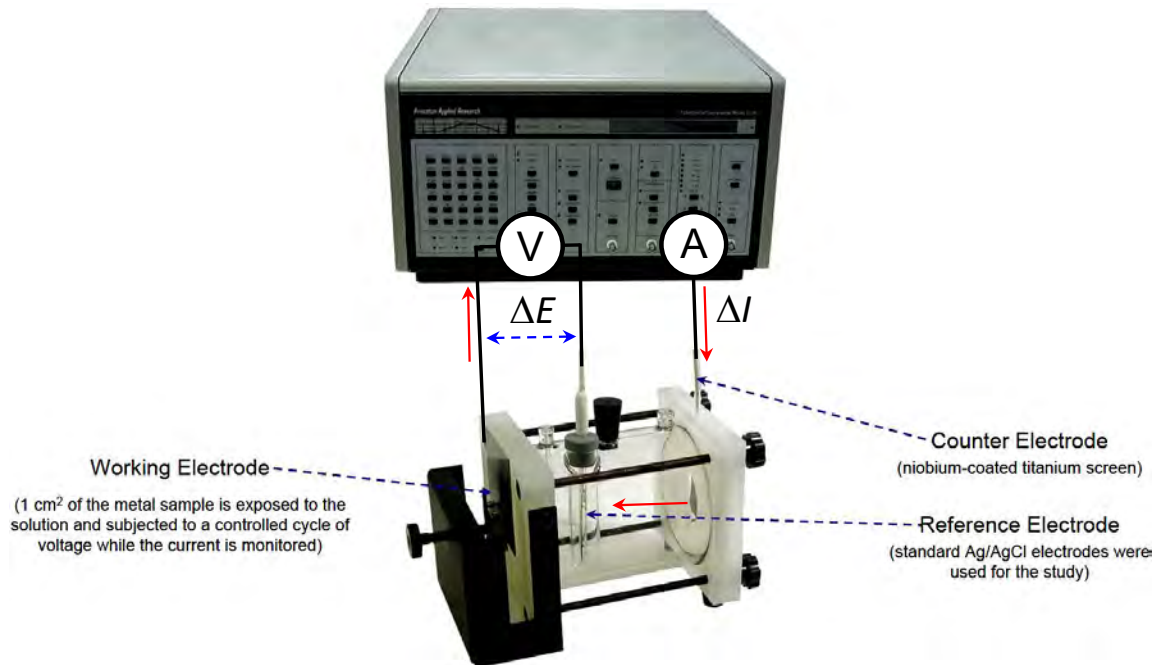


Figure A1: Simple diagram of the PAR potentiostat – and flat cell connections used in this project.

Since there is no absolute potential reference, the quantitative meaning of the measured voltage is dependent on the specific reference electrode that is used to make the measurement. The most common reference electrodes for electrochemical testing include the standard hydrogen electrode (SHE), the standard calomel electrode (SCE) and the silver/silver chloride electrode (Ag/AgCl) with the latter being used throughout these studies. In most electrolytic test cells, the resistance of the test solution skews the measurements. In order to minimize the ohmic drop due to solution resistivity, a special Luggin capillary tube was utilized which connected the reference electrode chamber to within a couple of milliliters of the sample surface. This configuration was standard as provided with the PAR Flat Cell apparatus. Also, the exposed sample test area in the flat cell configuration utilized throughout this work was exactly  $1\text{cm}^2$ . With this understanding, the terms current and current density are sometimes used interchangeably.

Within the test cell and throughout every DC polarization test cycle, the current is always directed from the counter electrode to the working electrode (the sample) while electrons are always flowing out of the working electrode. If a small voltage  $E$  is applied that is below the OCP (or  $E_{OC}$ ), the sample becomes cathodically charged with an excess of electrons and a corresponding cathodic current  $I_c$ . This overpotential can be represented as  $\eta = E - E_{OC}$ . As the applied voltage is increased back toward  $E_{OC}$  (which is also recognized as  $E_{Cor}$ ), the sample becomes less cathodic and the outflow of excess electrons diminishes. This is not chemical oxidation since the departing electrons are provided by a pool of excess conduction electrons, not valence electrons. At  $E_{Cor}$ , the net electron flow becomes zero as the anodic and cathodic currents are exactly equal. When the voltage continues above  $E_{Cor}$ , valence electrons begin leaving the sample which changes polarity and starts to anodically oxidize as it is driven by the anodic current  $I_a$ . In either case, the sample becomes polarized when its potential is forced away from its equilibrium value at OCP and the net current  $I_{net}$  becomes a mixture of  $I_c$  and  $I_a$ .

### A.3 The Polarization Curve

At the equilibrium steady state defined by  $E_{Cor}$ , the net current is zero since  $I_a = I_c$ . This is often referred to as the exchange current  $I_e$ , (equivalent to  $I_{Cor}$ ) which is a measure of the rate of electron transfer from metal to either oxygen molecules, hydrogen ions or other electrophiles within the test solution. The exchange or corrosion current is proportional to the oxidation rate (the corrosion rate) at the steady state where equilibriums exist between oxidation of metal atoms at anodic sites,



and reduction of molecular oxygen and/or hydrogen ions at cathodic sites,



Since the forward oxidation and reduction rates cancel each other at  $E_{Cor}$ , it becomes impossible to directly determine  $I_e$  or  $I_{Cor}$  as well as the desired recession, corrosion and oxide growth rates. Beyond about 50mV on either side of  $I_{Cor}$ , the process becomes dominated by either the anodic or cathodic reactions. These concepts are illustrated in Figure A2 showing a linear polarization data plot (in blue) for one of the Cronidur 30 samples (a high Fe-Cr alloy) which was conducted from -15V to +15V (vs. Ag/AgCl) relative to the OCP in brine solution. As will be demonstrated shortly, linear polarization techniques permit the determination of  $I_{Cor}$  and hence the desired oxidation/recession rates.

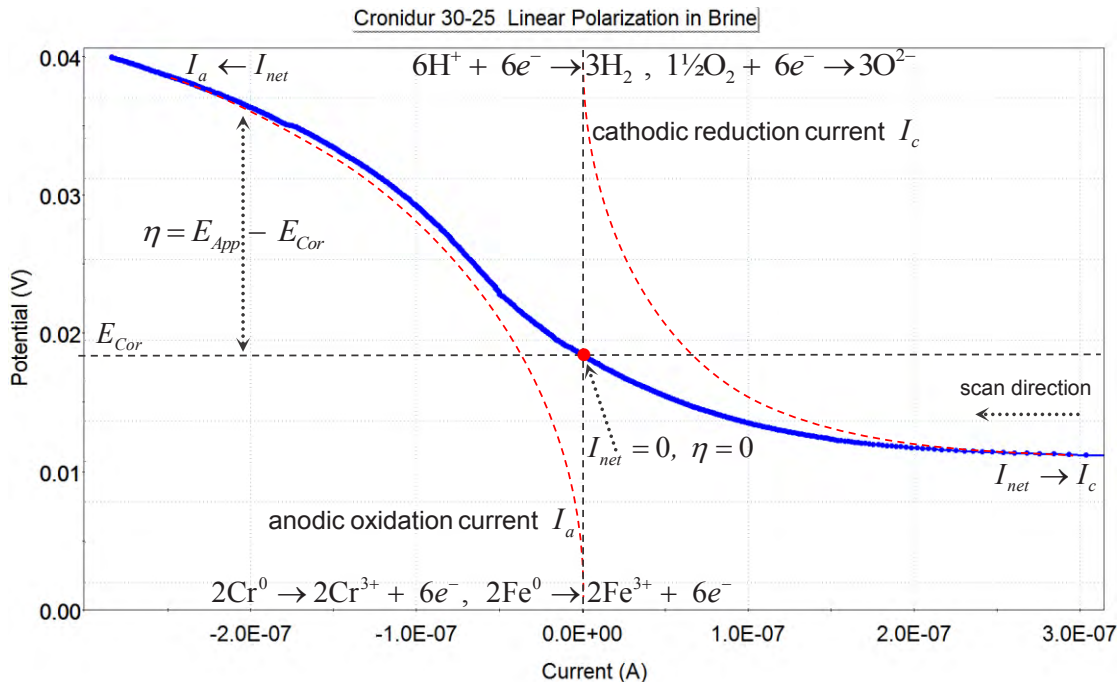


Figure A2: Current versus potential plot for one of the Cronidur samples showing anodic and cathodic branches.

Molecular congestion caused by the concentration of reactants and products along the metal-solution or oxide-solution interface may limit the current (and the transfer of electrons) since entities entering and leaving the reaction sites must diffuse through a thickened layer of solutes, reactants and products in a mass-transfer process across the adjacent solution. This is often referred to as ‘concentration polarization’ and the redox reactions are said to be diffusion-controlled. This should not be confused with the type of diffusion that occurs within the barrier and porous layers where other factors contribute to or affect the ion transfer process. The interfacial solution region of heavy concentration is referred to as the Nernst diffusion layer which can vary in thickness, composition, diffusivity and current-limiting attenuation anywhere along the polarization curve, or it may not be significant at all if the reactions are activation-controlled. Activation polarization is predominant when the redox reactions are not impeded by diffusional phenomena but proceed strictly in a charge-transfer process. In many cases, the actual process may be a mixture of activation and concentration polarization.

The symmetry of the anodic and cathodic segments relative to the point  $E_{Cor}, I_{net} = 0$  in Figure A2 may imply a small level of diffusion-controlled processes in the anodic region (where the passive layer is re-forming). A symmetry coefficient of 0.5 for both branches indicates an ideal activation-controlled situation which gives a perfect *sinh* curve form. The flat cell configuration in heated solution was pursued in this study in accordance with conditions utilized in previous studies. A rotating test sample would have facilitated a more uniform Nernst layer thickness with improved results. The apparent symmetry effects noted in Figure A2 may be more reflective of diffusional influences associated with the transport of species across the porous and barrier layers rather than concentration-limited transport within the adjacent solution. While the restricted transport of species through the fixed barrier and porous layers would likely be a combination of Darcy flow and Fickian diffusion, transport through the mobile Nernst layer would be exclusively Fickian in nature in accordance with Fick’s first law. However, widespread diffusional attenuations in this work appeared to be minimal in many cases.

#### A.4 The Butler-Volmer Equation

Examination of all the linear, Tafel and cyclic plots generated for this study indicated that the majority of redox reactions occurring in both branches for all six metals was heavily influenced by activation-dominated processes. Figure 16 actually gives a plot of the well-known Butler-Volmer (BV) equation<sup>[5]</sup> which is applicable to activation-controlled redox reactions occurring on the same electrode. The BV equation expresses the measured current density  $I_{net}$  in terms of the exchange current density  $I_e$  ( $\equiv I_{Cor}$ ), the overpotential  $\eta = E_{App} - E_{OC}$  (or  $E - E_{Cor}$ ), the number of electrons transferred during the redox reactions  $n$ , the cathodic and anodic symmetry coefficients  $s$  and  $(1 - s)$  respectively, the absolute temperature  $T$  (which is  $37^\circ\text{C} = 310\text{K}$  for our study), the gas constant  $R = 8.314 \text{ Jmol}^{-1}\text{K}^{-1}$ ) and the Faraday constant  $F = 96,485 \text{ C-Vmol}^{-1} \dots$

$$\begin{aligned}
 I_{net} &= I_c + I_a = I_c - |I_a| \\
 I_{net} &= I_e \exp\left(\frac{-snF}{RT} \eta_c\right) - I_e \exp\left(\frac{(1-s)nF}{RT} \eta_a\right)
 \end{aligned} \tag{1}$$

Note: The negative sign for the anodic current is due to physics sign conventions. For single metal polarization, the current is always flowing from the counter electrode to the test metal regardless of whether it is in the cathodic or the anodic region. The current in these configurations is understood to be positive throughout. However, in two metal

galvanic coupling configurations, the current can flow in either direction depending on which metal is the cathode and which is the anode. As will be shown later, the direction of current flow in these situations has special significance.

The left term in Eq(1) defines the cathodic current while the right term defines the anodic current. Together, they make up the entire polarization curve. To be precise, this expression would contain terms for each reaction occurring in the process but is shown in this incremental form for simplicity as it may apply to either redox reaction set indicated in Figure A2. If the overpotential  $\eta$  is greater than about  $\pm 50\text{mV}$  in either direction, one term dominates while the other becomes insignificant. Thus, the currents in the cathodic and anodic branches for large overpotentials are described respectfully by . . .

$$I_c = I_e \exp\left(\frac{-snF}{RT} \eta_c\right) \quad \text{and} \quad I_a = I_e \exp\left(\frac{(1-s)nF}{RT} \eta_a\right) \quad (2)$$

These expressions can be rearranged to give the well-known Tafel parameters for each branch. For the cathodic current . . .

$$\begin{aligned} \ln(I_c) &= \ln(I_e) - \frac{snF}{RT} \eta_c \\ 2.303 \log_{10}(I_c) &= 2.303 \log_{10}(I_e) - \frac{snF}{RT} \eta_c \\ \log_{10}\left(\frac{I_c}{I_e}\right) &= -\frac{snF}{RT} \eta_c \end{aligned}$$

from which . . .

$$\eta_c = \beta_c \log_{10}\left(\frac{I_c}{I_e}\right) \quad (3)$$

where the cathodic Tafel constant in volts is defined . . .

$$\beta_c = -\frac{2.303RT}{snF} = -\frac{0.0262}{sn}$$

Using Figure A2 as a rough guideline, if we let  $n = 3$  and  $s = \sim 0.75$ , (where  $s_c + s_a = 1$ ), the value of  $|\beta_c|$  comes out to 116 mV/decade compared to a value of 142 mV obtained for this particular sample during the experimental Tafel test run. Likewise, the anodic current becomes . . .

$$\ln(|I_a|) = \ln(I_e) + \frac{(1-s)nF}{RT} \eta_a$$

which leads to . . .

$$\eta_a = \beta_a \log_{10}\left(\frac{|I_a|}{I_0}\right) \quad (4)$$

where the anodic Tafel constant is defined . . .

$$\beta_a = \frac{2.303RT}{(1-s)nF} = \frac{0.0262}{(1-s)n} = 349 \text{ mV/decade}$$

This compares to a value of 416 mV obtained for this sample during the actual Tafel test run. Admittedly, there was a wide variation in the Tafel constant values determined throughout this work.

Now the Tafel expressions Eq(3) and Eq(4) are the so-called high-field approximations and can be written in slope-intercept form for future use . . .

$$\eta_c = a_c + \beta_c \log_{10}(I_c) \quad \text{where } a_c = -\beta_c \log_{10}(I_e)$$

and

$$\eta_a = a_a + \beta_a \log_{10}(|I_a|) \quad \text{where } a_a = -\beta_a \log_{10}(I_e)$$

By definition,  $\beta_c$  and  $\beta_a$  are the activation-controlled cathodic and anodic Tafel slopes or ‘beta’ values respectively and will become important parameters during Tafel analysis. Note that  $\beta_c$  represents a negative (cathodic) slope while  $\beta_a$  is a positive (anodic) slope.

And finally, the BV equation can be written in a more concise form . . .

$$I = I_{Cor} \left[ \exp\left(\frac{2.303\eta}{\alpha_a}\right) - \exp\left(\frac{2.303\eta}{\beta_c}\right) \right] \quad (5)$$

where  $\eta = E - E_{Cor}$  can represent the overvoltage in either direction.

## A.5 Faraday’s Law and Oxidation Rates

At the Steady State, oxidation and reduction rates are equal and the current associated with either reaction (the exchange current or so-called corrosion current  $I_e = I_{Cor}$ ) is a direct measure of the rates for these reactions. With strongly passivating metals such as the ones under evaluation here,  $I_e$  can be translated into the rates for base metal recession (penetration depth) and oxide thickness growth. While chemical reaction rates measure the mass quantity of products generated, recession and growth rates are volumetric in dimension. They share the same number of transferred electrons but different geometrical densities which results in unique weight and volumetric changes associated with recession into the base metal and the accompanying oxide growth which then occupies both the recessed metal volume and a certain protrusion height above the original metal line. While the total oxide volume occupies both of these areas, its height above the original metal surface is often the parameter of interest.

Since  $I_e$  (and hence the dimensional rates) cannot be measured directly they must be surmised by one of the linear methods covered in the next section. Once the exchange current is ascertained, a modification of Faraday’s famous law can be used to estimate the rates associated with weight and volume changes during the oxidation process. The premise can be stated that for a given reaction, the current  $I$  is directly proportional to the sample weight gained or lost over time  $W_{\Delta}/t$ , as well as the number of electrons

$n$  transferred during the reaction, and is inversely related to the molecular weight  $M_w$  of the electroactive species involved, where  $F$  is Faraday's constant . . .

$$\frac{IM_w}{nW_\Delta / t} = F$$

Recognizing that  $M_w/n$  is the equivalent weight  $W_{Eq}$  of the reacting species and utilizing its density  $\rho$ , weight and volume changes can be written respectfully in terms of the associated current, the equivalent weight and the density . . .

$$\frac{W_\Delta}{t} = I_{Cor} \frac{W_{Eq}}{F} \quad \text{and} \quad \frac{V_\Delta}{t} = I_{Cor} \frac{W_{Eq}}{F\rho}$$

The second expression is of importance in our study as it will permit determination of the respective metal recession and oxide growth rates  $k_{Met}$ ,  $k_{Ox}$  (both volumetric rates). By ascertaining the measured current, the equivalent weight of the base metal and composite oxide (which may be comprised of many components), and the mass density of the composite oxide, these rates become . . .

$$k_{Met} = I_{Cor} \frac{W_{Eq, Met}}{F\rho_{Met}} \square c \quad \text{and} \quad k_{Ox} = I_{Cor} \frac{W_{Eq, Ox}}{F\rho_{Ox}} \square c \quad (6)$$

where  $c$  is a conversion factor incorporated to express the rates in the desired units.

For this study, weight constituents are given in grams and densities in  $\text{g/cm}^3$  while the rates reported throughout this work are often given in Angstroms per day ( $\text{\AA}/\text{day}$ ) and mils per year ( $\text{mil}/\text{year}$ ) whose  $c$  values are respectfully,  $8.9588 \times 10^7 \text{ Eq}\cdot\text{sec}\cdot\text{\AA}/\text{C}\cdot\text{cm}\cdot\text{day}$  and  $1.2874 \times 10^5 \text{ Eq}\cdot\text{sec}\cdot\text{mil}/\text{C}\cdot\text{cm}\cdot\text{yr}$ . While the number of exchange electrons transferred from the metal must exactly equal the number of electrons transferred to the oxide, the equivalent weights (and volumes) of these two phase are definitely not equal. During the course of these studies, special approaches were formulated for estimating the  $W_{Eq}$  associated with the base metals *and* their corresponding composite oxides. Of particular interest here is determination of the oxide  $W_{Eq}$  values which is unconventional. These concepts will be covered later.

## A.6 Estimation of Currents and Rates

Before leaving Figure A2, one last concept should be explored centering on the point  $E_{Cor}$  at  $I = 0$  (the red marker). Below  $E_{Cor}$ , the sample acts as a cathode, above  $E_{Cor}$ , the sample becomes an anode as it changes polarity. A technique developed by Stern and Geary (SG) many years ago provides a simple approach for estimating the exchange current (density) and hence, the rates for corrosion, metal recession and oxide growth. They introduced the term of 'polarization resistance'  $R_{Pol}$  (or  $R_{Cor}$ ) in analogy to Ohm's law or more precisely, they demonstrated that an inverse relationship exists between  $I_{Cor}$  and  $R_{Cor}$  when very small overpotentials are applied relative to  $E_{Cor}$  (scan ranges such as  $-20\text{mV}$  to  $+20\text{mV}$  or smaller are typical) and that the slope of the polarization curve in this region  $dE/dI = R_{Pol}$  describes a straight line



as it passes through  $I_{Cor} = 0$  (for cases with minimal linearity, the tangent line at this point can be used). Their work resulted in the following simple but very useful relationship . . .

$$I_{Cor} = \frac{B}{R_{Cor}} \quad (7)$$

where  $B$  is a proportionality parameter based on the Tafel constants in units of volts.

Historically, the SG equation has been utilized and experimentally validated many times since its introduction in the early 1900's. Validation of this approach can also be demonstrated mathematically through its relationship with the BV equation, and then the constant  $B$  can be determined. Utilizing the series expansion identity,  $e^x = 1 + x + x^2/2! + x^3/3! + \dots$ , and neglecting the higher terms for low overpotentials, Eq(5) can be written and rearranged . . .

$$I = I_{Cor} \left( \frac{2.303\eta}{\beta_a} - \frac{2.303\eta}{\beta_c} \right)$$

from which . . .

$$\frac{dI}{dE} = 2.303(\beta_a^{-1} - \beta_c^{-1})I_{Cor} \quad \text{where we let } \eta = dE \text{ and } I = dI$$

and then . . .

$$I_{Cor} = \frac{1}{2.303} \left( \frac{\beta_a \beta_c}{\beta_a + \beta_c} \right) \frac{dI}{dE} = \frac{B}{R_{Cor}}$$

where . . .

$$B = \frac{1}{2.303} \left( \frac{\beta_a \beta_c}{\beta_a + \beta_c} \right)$$

The SG method is the so-called low-field approximation since only a very small scan range is applied. The approach is based on the assumptions that (a) all the reactions are reversible, (b) they are activation-controlled, (c) the energy barriers for the forward and reverse reactions are symmetrical, and (d) the results pertain only to general corrosion/oxidation events, providing no information regarding activity associated with localized pitting or crevice corrosion. The range of applied potential is so small that the test is nondestructive and results are obtained very quickly. This method is useful for long-term continuous corrosion monitoring in field structures. An example of the SG technique applied to one of the Hastelloy C276 samples in Concentrated Pretreat solution was given in Figure 5 earlier and is reproduced here for convenience in Figure A3.

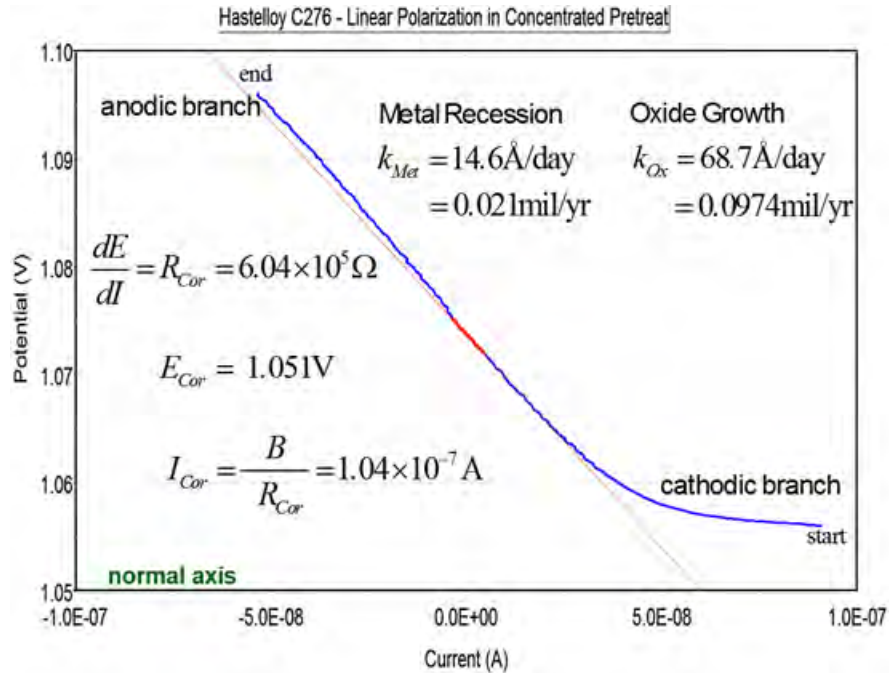


Figure A3: Linear polarization test plot and analysis for Hastelloy C276 in Concentrated Pretreat.

Again, the total oxide thickness includes recession depth plus outward growth. The Tafel constants applied to the Linear calculations in A3 were taken from subsequent Tafel testing. Note that the plot in Figure A3 utilizes normal ordinate or linear axes for both dimensions. If this same data were re-plotted in semi-log form, converting the  $x$  axis (the current) into the corresponding  $\log_{10}$  values, a low-field Tafel plot would be obtained. Thus, a Tafel test run is essentially a Linear test that is applied over a wider potential range and plotted on semi-log axes. Since the Current (or  $x$ -axis) can often change magnitude over several orders in a single run, the log version of this data field is useful for examining variations in the plot. It is standard industry practice to plot both Tafel and Cyclic data on semi-log axes during each experiment run. Later on, it will be shown how specialized information can be extracted from just the normal Tafel and Cyclic plots, but for the present, classical Tafel evaluations utilizing the SG and BV approaches are provide an abundance of information, including the rates for corrosion, recession and passivation. An example of one of the Tafel experiments with analysis was given in Figure 6 earlier and is reproduced here for convenience in Figure A4.

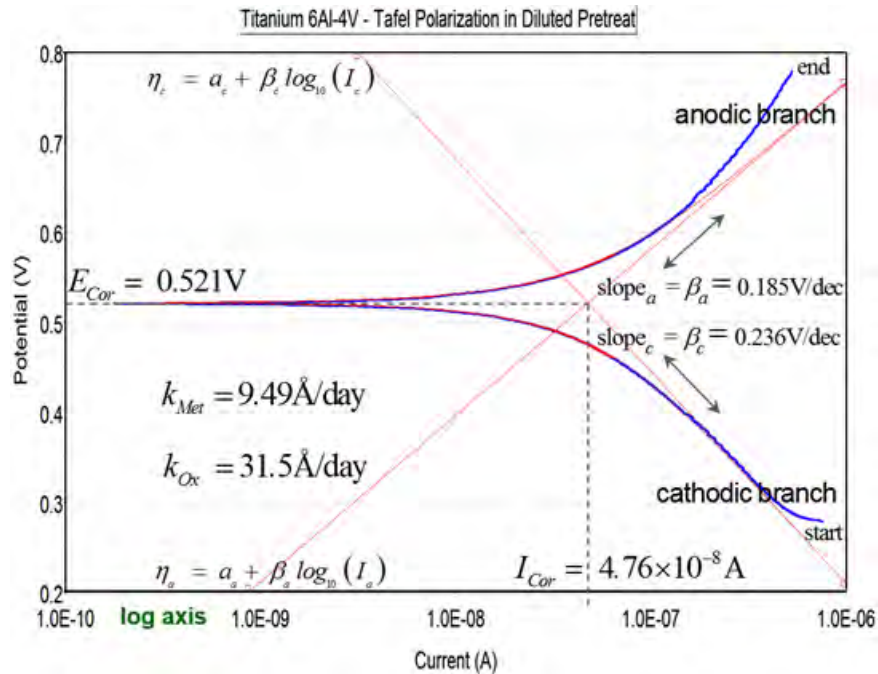


Figure A4: Semi-log Tafel polarization test plot and analysis for Titanium 6Al-4V in Diluted Pretreat.

In practice, a typical Tafel test run is scanned over a wider potential range than Linear scans in order to capture a greater portion of the anodic and cathodic branches. In this format,  $I_{Cor} = 0$  coincides with the log inflection point and provides the key to determining all the other critical parameters in the Tafel plot. In essence, both of these techniques can be considered linear polarization, and they both provide essentially the same results. However, when the semi-log version is utilized, the Tafel method utilizes a different analytical approach by applying linear fits along the straight portions of each branch, which together form a basic Evans diagram, and whose intersection analytically identifies both  $E_{Cor}$  and  $I_{Cor}$ , and then the desired recession-oxidation rates can be computed from  $I_{Cor}$ . This approach is illustrated in Figure A4. For the UWMS study, in all cases, the results obtained from Linear analysis were essentially identical to those derived from Tafel analysis. Thus, the two techniques employ different approaches for analysis but provide complimentary outcomes that reinforce the confidence level of the data obtained.

The primary dominating metal constituents in the three alloy candidates evaluated in this study included Titanium (Ti) in the Titanium 6Al-4V candidate, and Chromium (Cr) and Nickel (Ni) in both the Inconel 625 and Hastelloy C276. While a number of reactions are possible with the alloying components, the fate of primary constituents within acidic media will generally involve oxidation of the metal, reduction of hydrogen ion and molecular oxygen, precipitation of the metal oxide and hydrolytic dissolution of the oxide in the acidic test solution. These processes are illustrated in Figure A5 for the three metal constituents of interest.

Unless noted otherwise, theories, mechanisms and illustrations provided in the following sections are the perception and handiwork of the author. No guarantees are given regarding correctness or accuracy.

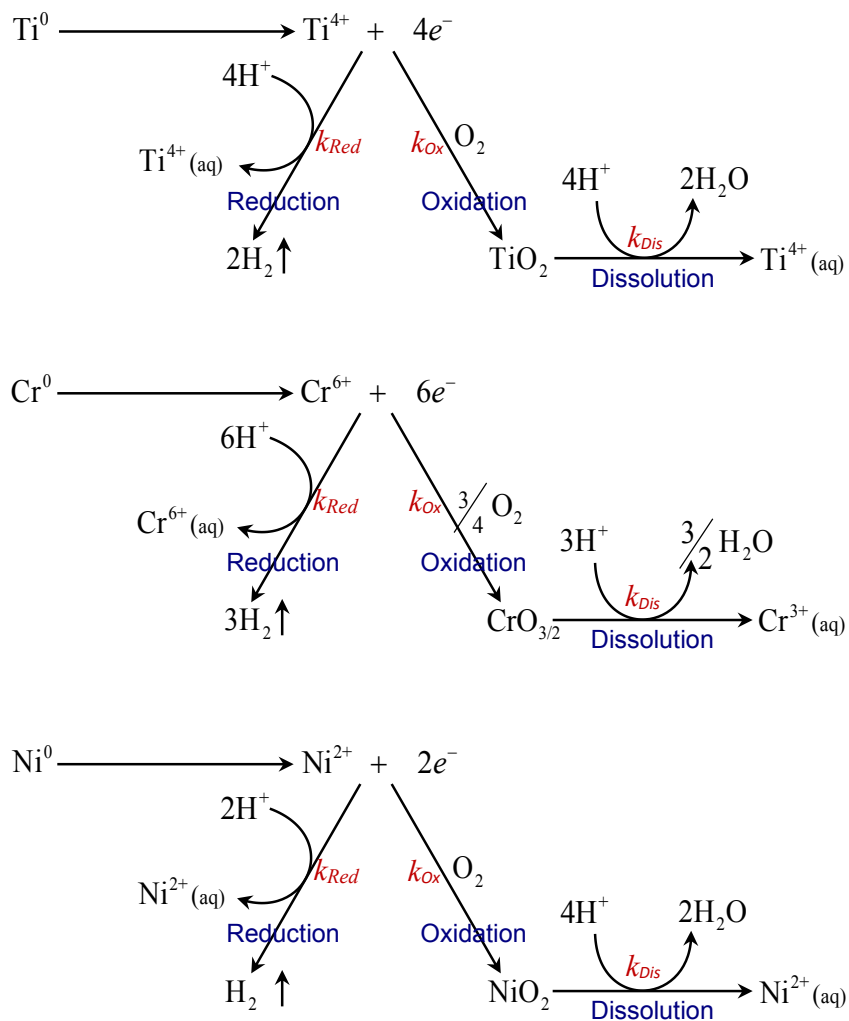


Figure A5: Possible pathways of Titanium, Chromium and Nickel in acidic solution.

Figure A5 depicts a simplified summary of the reactions for oxidation, reduction and dissolution across the metal-oxide/hydroxide-solution interface for the three metals of interest in this study, Ti, Cr and Ni. The diagrams illustrate the specific reactions associated with (A) the reduction of  $H^+$  to form  $H_2$  (resulting in a pH increase), (B) oxidation of the base metal to form its passive oxide utilizing aqueous oxygen within the media, and (C) dissolution of the passive oxide product via acid hydrolysis which ejects metal ions into the solution. At a Steady State equilibrium condition, the rates for oxidation, reduction and dissolution are all equal,  $k_{Ox} = k_{Red} = k_{Dis}$ . Under dynamic anodic conditions, electrons are flowing out of the metal-oxide system as the rate of metal oxidation increases which in turn increases the rate of passive oxide generation while the rate of steady state oxide dissolution remains about the same. During cathodic situations, electrons are flowing into the metal-oxide system. In this case, oxidation of the base metal does not occur so the rate of oxide generation either becomes dormant or goes negative as it begins to undergo reduction, resulting in the production of water and molecular hydrogen as the rate of steady state dissolution remains about the same. However, the removal of oxide is greatly accelerated as it undergoes both reductive dissolution and hydrolytic dissolution resulting in cathodic stripping of the

oxide. In any given cathode-anode situation, if the  $pH$  of the media decreases (becoming more acidic), the rate of oxide dissolution increases which in turn increases the rate of oxide generation and base metal oxidation. Conversely, these decrease as the  $pH$  becomes less acidic.

## A.7 Analysis of Cyclic Polarization Curves

Information pertaining to general corrosion and oxidation is obtained during the linear methods previously covered. While general corrosion/oxidation aspects can be acquired or substantiated during subsequent cyclic test runs, the most valuable information obtained is related to the tendency for corrosive pitting, crevicing or etching. In general, cyclic polarization is a destructive test as the surface of the sample is disturbed, sometimes with visible results. Most cyclic polarization test runs start out by applying a linearly increasing voltage ramp that begins in the negative cathodic area (same as a Tafel scan), increasing through the Tafel region and then up into the anodic region, beyond the passivation zone and through the breakdown potential of the passive oxide to a pre-selected potential where the voltage scan reverses as it ramps back down toward the cathodic region. A hysteresis loop is usually generated. Several key points and regions are realized in the cyclic scans conducted on the subject metals.

- (a)  $E_{Cor1}$  – As covered earlier. This is the primary polarity switching point from cathode to anode when passivation just begins during the up-scan and pertains to general corrosion/passivation.
- (b) The Tafel region – As covered earlier,  $E_{Cor1}$  and  $I_{Cor}$  are represented by the intersection of the Tafel beta line slopes pertaining to possible general corrosion/oxidation events.
- (c)  $E_{Pas}$  – The primary passivation potential taken at the apex (the tangent) of this curve section provides  $E_{Pas}$  and sometimes  $I_{Pas}$  which represent the maximum passivation potential and passivation rate attained before oxide growth begins to end or level off.
- (d) The passive region or plateau – The passive oxide may strengthen a little after passing through  $E_{Pas}$  but then weaken with possible metastable pitting as the breakdown point is approached.
- (e)  $E_{Brk}$  – The oxide breakdown potential is analogous the dielectric strength of the oxide and pertains to the point where the oxide structure can be breached possibly followed by pitting initiation or general etching (depending on the solution composition). Behavior of the plot just after  $E_{Brk}$  may be indicative of the metal's susceptibility to pitting/etching initiation.
- (f)  $E_{Ver}$  – The scan reversal potential or so-called vertex is a user-selected point where the increasing voltage ramp reverses and begins to decrease (same rate as the up-ramp). Behavior of the plot just after  $E_{Ver}$  can provide unique insight regarding the metal's repassivation capability to provide protection against sustained pitting or etching.
- (g)  $E_{ReP}$  – The repassivation potential is represented by the apex of the return curve where repassivation is winding down and the recovery process is near completion. Techniques to surmise maximum rates for pitting penetration and repassivation growth will be discussed later.

The repassivation region provides further information regarding the repassivation process and the degree of protection attainable. The direction and area of the hysteresis loop reflects the strength or robustness of the metal's self-protection mechanism against sustained pitting. For strong passivating metals, the instant  $E_{Ver}$  is passed, any signs of possible pit initiation immediately vanish as the metal rapidly begins repassivation, oxide regeneration and system recovery at a maximum repassivation rate.

(h)  $E_{Cor2}$  – This is the polarity switching point from anode back to cathode during the down-scan after repassivation is complete. Pertains to general corrosion/oxidation and general repassivation.

Cyclic plots and graphical analysis for one of the Hastelloy and Cronidur samples are given in Figures A6 and A7 as examples to help illustrate some of these parameters and concepts.

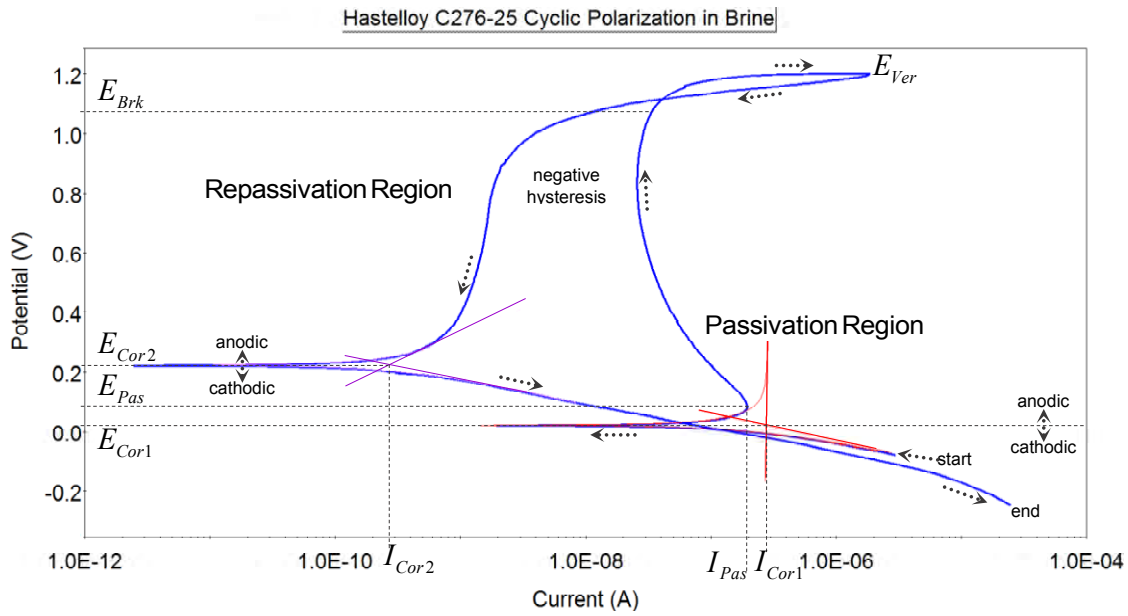


Figure A6: Cyclic polarization test results and analysis for Hastelloy in brine.

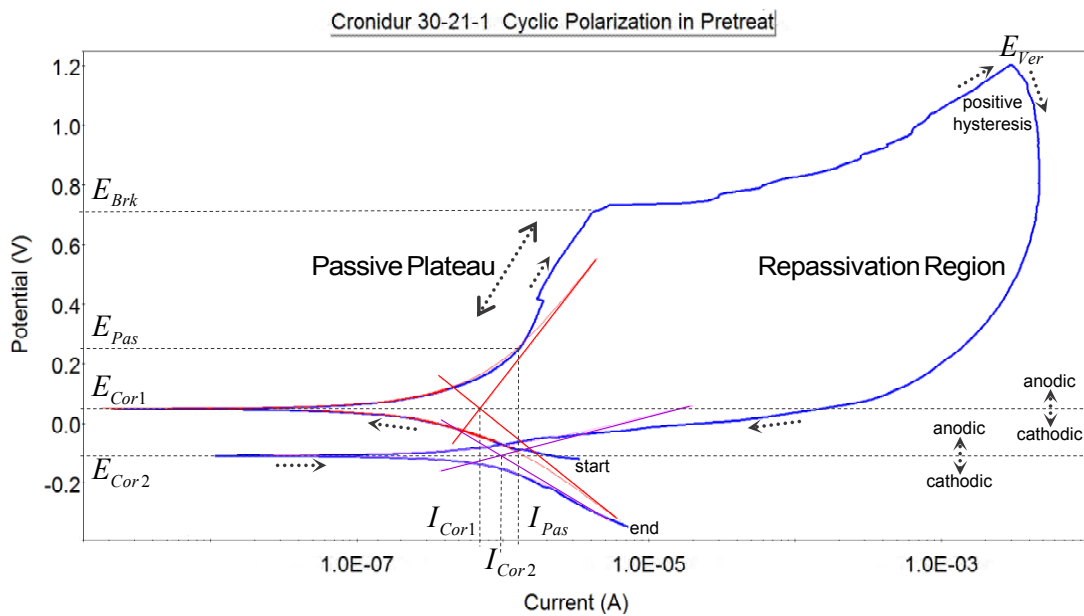


Figure A7: Cyclic polarization test results and analysis for Cronidur in pretreat

The cyclic curve form displayed for Hastelloy in Figure A6 is reflective of most of the plots for the other Hastelloy samples as well as most of the Inconel samples in both solutions. It also bears significant similarity to most of the Titanium plots. While the Cronidur plots contain the same parameters, regions and points, the curve shapes and ranges were notably different than the other metals. Approaching  $E_{Brk}$ , metastable pitting becomes possible. Between  $E_{Brk}$  and  $E_{Ver}$ , the oxide might be compromised and active pitting could be taking place. After passing  $E_{Ver}$ , the oxide either (a) repairs itself very rapidly and all vestiges of pitting completely vanish or (b) the oxide repairs itself slowly while sustained (or metastable) pitting attempts to survive. Case (a) describes all the Inconel, Hastelloy and Titanium samples where the slope of the curve following  $E_{Ver}$  immediately rebounds as the current decreases sharply and the repassivation forces completely overwhelm any possible traces of pitting that may have existed. This also results in negative hysteresis (since the down-ramp data is now tracking behind the up ramp).

On the other hand with case (b), there is a forward component observed in the Cronidur plot just after  $E_{Ver}$  is passed (positive hysteresis) which implies that pitting may still be occurring after the voltage reversal point. This is depicted in Figure A7. In general,  $E_{Ver}$  is likened to a sort of relief point in the voltage-driven breakdown process where a robust self-repairing mechanism has the opportunity to swiftly rebuild broken structural links in the oxide lattice, but Cronidur shows weaknesses in this aspect with a very high positive hysteresis area. Thus, negative hysteresis implies strong repassivation protection forces while positive hysteresis is indicative of poor pitting protection. This is one of the primary differences between Cronidur and the other metals. There are other disparities.

Note: Many of the techniques and concepts introduced in this and the following sections were empirically developed as extensions to ASTM G102 and may be considered as original approaches for evaluating and characterizing corrosion, pitting and oxidation phenomena. While these techniques have seemed to work well throughout these studies, no guarantee can be given regarding their validity or accuracy in other applications.

The higher the potential required to locally damage or breakdown the passive oxide  $E_{Brk}$ , the higher the resistance to pitting. Consider the potential height of  $E_{Brk}$  or rather the potential difference between  $E_{Brk}$  and the primary passivation potential  $E_{Pas}$  in Figures A6 and A7. For the Hastelloy sample, the difference  $E_{Brk} - E_{Pas}$  is over one volt, while this same distance on the Cronidur plot is about a half a volt. In the pretreat test solution, this potential ranged from about 800-900mV for the Inconel, Hastelloy and Cronidur samples. In the Brine test solution, a similar range was obtained for the Inconel and Hastelloy samples but the Cronidur samples were lower, ranging from about 400-700mV. The Titanium materials ranged from about 1300-1500mV in both solutions. These results tend to support the evidence that Cronidur is relatively more susceptible to pitting in the brine solution than the other metals and that all the Titanium metals are superior in both solutions. The potential difference  $E_{Brk} - E_{Pas}$  provides insight regarding the tendency of pits to form that is, the susceptibility of pitting initiation which is a unique characteristic for each of these metals. Special methods for estimating initiation and sustainment susceptibilities are covered later.

Now, examine the relative locations of  $E_{Cor1}$  and  $E_{Cor2}$  with respect to the potential axis in Figures A6 and A7. Note that  $E_{Cor1}$  (same as  $E_{Cor}$  in previous discussions) and  $E_{Cor2}$  are both dominated by general corrosion effects, but  $E_{Cor2}$  may also be influenced by events associated with pitting which can lead to a general repassivation regeneration process terminating at  $E_{Cor2}$ . Also, recall that  $E_{Cor1}$  marks the beginning of the primary passivation process when the sample switches from cathode to anode and oxide growth accelerates in order to protect the metal from the solution, while  $E_{Cor2}$  marks the end of the repassivation growth process after the oxide has completed all the rebuilding and repair steps, switching from an anode

back to a cathode. The higher that  $E_{Cor2}$  is on the potential axis (and the closer it is to  $E_{Brk}$ ), the sooner the oxide regeneration process is completed and the more resistant the base metal becomes to general and pitting corrosion, even though it is adequately protected well before reaching  $E_{Cor2}$ . Nevertheless, note that for the Hastelloy plot,  $E_{Cor2}$  is higher than  $E_{Cor1}$  while on the Cronidur scan,  $E_{Cor2}$  is lower than  $E_{Cor1}$ . Indeed, for all the Inconel, Hastelloy and Titanium samples,  $E_{Cor2}$  is above  $E_{Cor1}$ , but for all the Cronidur scans,  $E_{Cor2}$  is below  $E_{Cor1}$  in both solutions. For most of the Titanium samples in this study,  $E_{Cor2}$  was very high and very close to  $E_{Brk}$ , further supporting the premise that Titanium and its alloys are extremely resistance to both pitting and general corrosion in these solutions.

## A.8 Semi-Log vs. Normal Cyclic Polarization Plots

Behavior of the curve in the  $E_{Brk}$ - $E_{Ver}$ - $E_{ReP}$  region is critical. If the experimental scan is tailored appropriately so that the  $E_{Brk}$  region is captured well below  $E_{Ver}$ , the net current along the slopes preceding and following  $E_{Ver}$  can be evaluated. Along the slope preceding  $E_{Ver}$ , the current balance is dominated by pitting (metal recession) with a resistance  $R_{Pit}$ , while along the slope following  $E_{Ver}$ , the current is dominated by repassivation (oxide regeneration) with a resistance  $R_{ReP}$ . Since  $E_{Brk}$  is associated with  $R_{Pit}$  and  $E_{ReP}$  is associated with  $R_{ReP}$ , the following rudimentary expressions can be suggested . . .

$$\left| \frac{dE}{dI} \right|_{Pit} \sim R_{Pit} \sim \frac{E_{Brk}}{I_{Pit}} \quad \text{and} \quad \left| \frac{dE}{dI} \right|_{ReP} \sim R_{ReP} \sim \frac{E_{ReP}}{I_{ReP}}$$

These ideas are illustrated in Figure A8 for one of the Inconel samples showing how pinpoint values for  $E_{Pit}$ , and  $E_{ReP}$  can be acquired along with quantitative representations for the maximum pitting rate and the maximum repassivation rate via slope and tangent analysis using the normal plots.

Note in Figure A8 that the tangent point for  $E_{ReP}$  is not visibly apparent on the log plot. Also, the intersection of the scan lines on a log plot are often mistaken to represent the pitting or repassivation current. For most of the Cronidur samples, the maximum pitting rate exceeded the maximum repassivation rate, but for all the other metals, any possible traces of pitting were completely subdued by the oxide regeneration process. This implies that pitting into the base metal of Cronidur could conceivably be the net result under extreme environmental conditions. As revealed during testing, pitting was visibly evident in most of the Cronidur samples after cyclic polarization. The extent and depth of pits in Cronidur samples tested in brine solution were well pronounce. Such results may be related to the repassivation-pitting rate ratio which is a direct result of the extremely low repassivation potential  $E_{ReP}$  that was characteristic of Cronidur scans in both solutions.



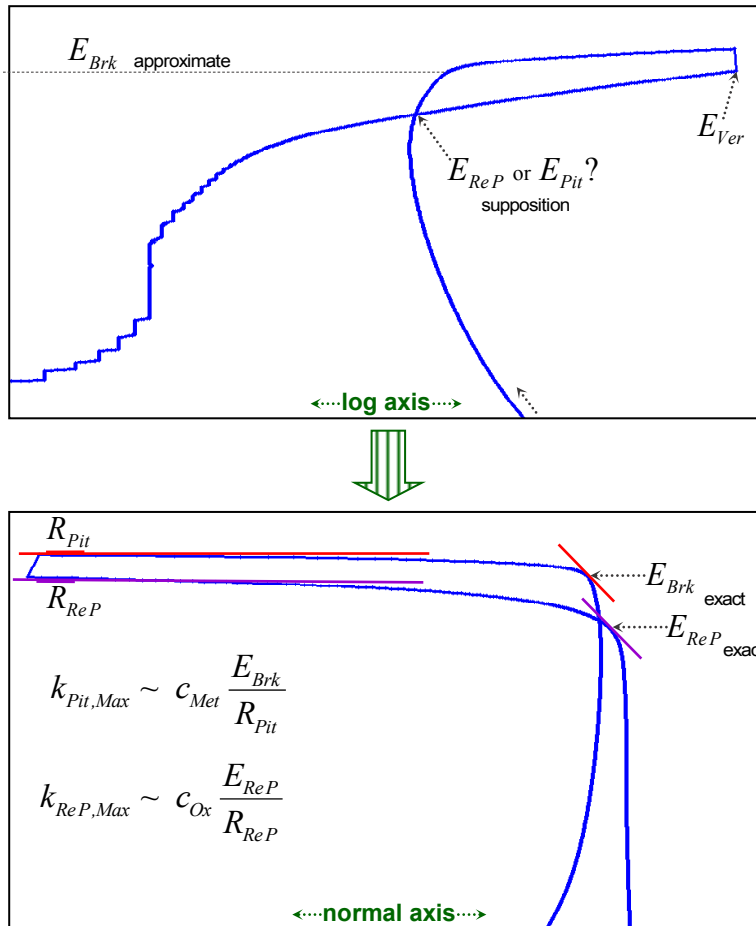


Figure A8: Method for evaluation of critical pitting and repassivation parameters using semi-log and normal plots.

## A.9 Special Method for Determination of Electron Exchange Equivalents

Calculation of equivalent weights ( $W_{Eq}$ ) for metals and alloys subjected to polarization measurements is required in order to determine corrosion/oxidation rates. Estimation of  $W_{Eq}$  values derived purely from base metal compositional ratios is common practice. However, this may not be the best approach due to selective oxidation of the various alloy components. The concept of selective oxidation is mentioned in ASTM G102 but not elaborated on. In fact, there has been ample data published utilizing depth profiling via XPS (ESCA), SIMS and Auger analysis confirming that selective oxidation does indeed occur. Clearly, differences in oxidation susceptibilities between the alloying elements in a metal mixture are substantial, and the relative fractions of metals comprising cation sites within the oxide lattice are rarely the same as those in the base metal itself. In most cases, the ratio of metals in the substrate and the oxide phase are not even close. Estimation of electron equivalents and equivalent weights utilizing base metal compositions is inaccurate. Depth profiling results of the oxide layers for a couple of relevant alloys are given in Figure A9. There are many more such analyses throughout the literature.\

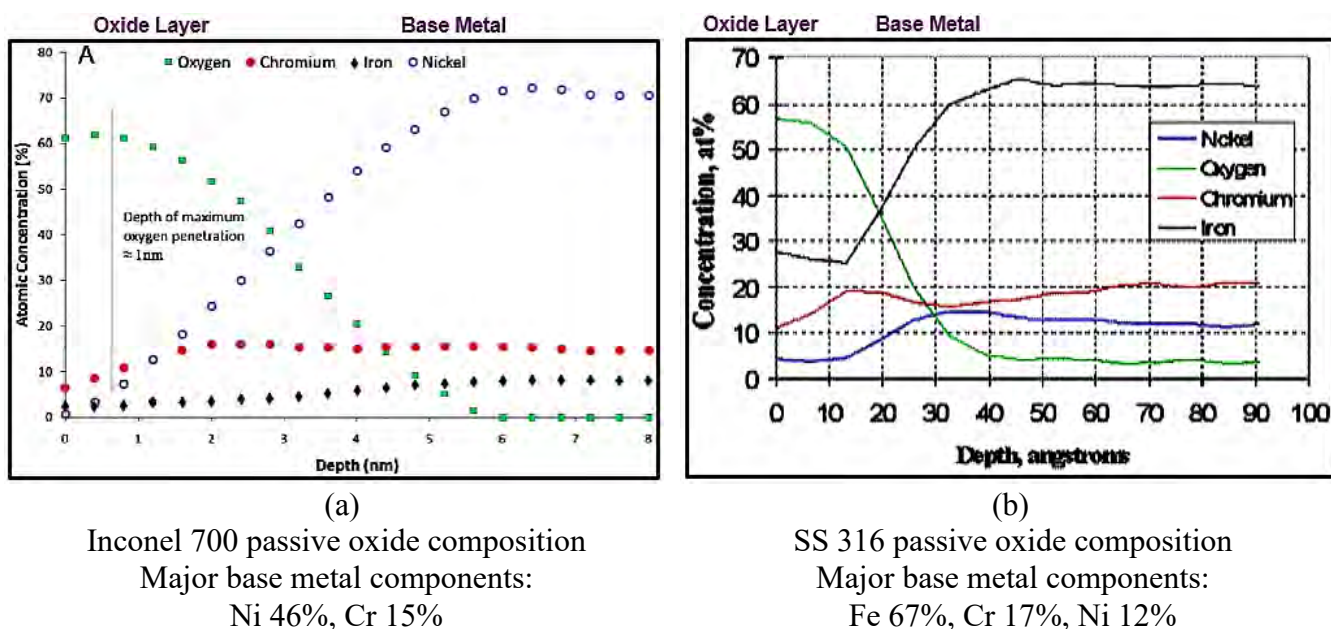


Figure A9: (a) Depth profile of the passive layer on Inconel 700 contrasting the relative metallic concentrations in the base metal and the passive oxide<sup>[11]</sup>. (b) Depth profile of the passive layer on 316 stainless steel contrasting the relative metallic concentrations in the base metal and the passive oxide<sup>[12]</sup>.



The intersection points between oxygen and the primary base metal constituent roughly indicate the center of the metal-to-oxide transition zone. When comparing the percentages of metal components in the oxide (particularly the outer layers of the oxide) and deep within the base metal, it becomes obvious that, at least for passivating metals, estimations involving the transfer of electron equivalents during the oxidation process cannot be precisely represented by assuming that the base metal constituents adequately represent the metallic constituents in the oxide layer. Indeed, in order to be specific, the net number of electrons extracted from the metal during the oxidation process must equal the net number of electrons consumed to form the oxide.

The following approach is proposed as an extension to ASTM G102. Reiterating, the number of electrons transferred from the base metal during corrosive oxidation must equal (exactly) the number of electrons transferred to produce the alloy oxide (in accordance with the conservation laws). Recognition of certain factors associated with the formation and composition of the oxidation product are key to estimating how many exchange electrons are actually generated. It is well known that the various metals in an alloy will oxidize at different rates according to their Gibbs free energy of formation. For example, Cr<sub>2</sub>O<sub>3</sub>, with a known formation energy of  $\Delta G_f = -1053$  kJ/mol) is five times more likely to form than NiO whose formation energy is documented to be  $\Delta G_f = -212$  kJ/mol. The  $\Delta G_f$  values clearly reflect this. Thus, we can state that the Relative Ease of Oxide Formation according to the respective free energies of formation can be tabulated and ordered. For example . . .

Nb <sub>2</sub> O <sub>5</sub>	>	Al <sub>2</sub> O <sub>3</sub>	>	V <sub>2</sub> O <sub>3</sub>	>	Cr <sub>2</sub> O <sub>3</sub>	>	TiO <sub>2</sub>	>	Fe <sub>2</sub> O <sub>3</sub>	>	MoO <sub>3</sub>	>	NiO
-1866		-1582		-1139		-1053		-890		-742		-668		-212

The more negative the value, the more likely the oxide will form from its elements. A rather extensive database was compiled for this study by tabulating, averaging and evaluating established Handbook values and a multitude of historically documented experimental values obtained throughout the research industry to obtain average representative values for the formation energies, bulk densities, skeletal densities, dielectric constants, and various other material properties for the composite oxides of interest in this study. There would be perhaps too many citations to note here and each input available was taken under consideration only as part of the surmised average, not utilized directly. While bulk compositions and electrochemical properties of the solution-formed oxides are different than the simpler passive layers that form in the air, metal contents are not all that different. Much research, supplementary estimations and educated guesswork were put into this effort in order to better understand, semi-quantify and ascertain the most likely composite oxide compositions and associated net property estimates expected for each of the six metals under evaluation in the subject test solutions. An spreadsheet example of one of the metals processed in this manner is illustrated in Figure A10

**Hastelloy C276 Base Metal Wrought Composition, As-Received – In Air**

	Raw Wt%	Est Wt%	Mol. Wt.	Atomic %	# Eq. e <sup>-</sup>	N <sub>Ae</sub> <sup>-</sup> /g
Ni	58.9%	59.3%	58.69	63.1%	0.67	1.14E-02
Cr	16.1%	16.2%	52.00	19.5%	2.72	5.24E-02
Mo	15.3%	15.4%	95.94	10.0%	0.55	5.75E-03
Fe	5.6%	5.6%	55.85	6.3%	0.39	6.92E-03
W	3.4%	3.4%	183.84	1.2%	0.10	5.18E-04
<hr/>		99.3%	100.0%	<hr/>		100.0%
					<b>4.42</b>	13.0 g/mol
						Net Equivalent Weight
Density	8.89 g/cc		8.77 g/cc			
	measured		estimated			
						

**Hastelloy C276 Composite Oxide Composition – In Acidic Test Solution**

	Mole %	Atomic %	Less H <sub>2</sub> O	# Eq. e <sup>-</sup>	N <sub>Ae</sub> <sup>-</sup> /g	
Cr <sub>2</sub> O <sub>3</sub>	32%	Cr 21%	23%	2.031	1.34E-02	
CrO <sub>3</sub>	8.9%			0.558	5.58E-03	
CrOOH	0.48%			0.015	1.79E-04	
CrOOH <sub>2</sub> <sup>+</sup>	3.7%			0.118	1.37E-03	
NiO	10.5%	Ni 6.8%	7.2%	0.221	2.96E-03	
Ni <sub>2</sub> O <sub>3</sub>	4.1%			0.259	1.57E-03	
NiOOH	0.60%			0.019	2.06E-04	
NiOOH <sub>2</sub> <sup>+</sup>	5.3%			0.168	1.82E-03	
MoO <sub>3</sub>	6.6%	Mo 2.5%	2.6%	0.416	2.89E-03	
MoO <sub>2</sub>	0.53%	<b>Protonated Oxide Surface</b>		0.022	1.73E-04	
MoO <sub>2</sub> (OH) <sub>2</sub>	0.20%			0.012	7.70E-05	
MoO(OH) <sub>2</sub> <sup>+</sup>	1.6%			0.102	6.24E-04	
Fe <sub>2</sub> O <sub>3</sub>	4.6%	Fe 3.5%	3.7%	0.289	1.81E-03	
FeO	0.08%			0.002	2.28E-05	
Fe <sub>3</sub> O <sub>4</sub>	0.94%			0.074	3.20E-04	
FeOOH	0.08%			0.002	2.68E-05	
FeOOH <sub>2</sub> <sup>+</sup>	0.60%			0.019	2.11E-04	
WO <sub>2</sub>	0.61%	W 0.47%	0.50%	0.026	1.18E-04	
WO <sub>3</sub>	0.87%			0.055	2.37E-04	
WO <sub>2</sub> (OH) <sub>2</sub>	0.03%			0.002	6.59E-06	
WO(OH) <sub>2</sub> <sup>+</sup>	0.21%			0.013	5.25E-05	
<hr/>				<b>4.42</b>	<b>Total Metal Equivalents</b>	
H <sub>2</sub> O	17%	O 65%	63%	<b>4.42</b>	<b>Total Oxygen Equivalents</b>	
<hr/>		100.00%	100.00%	100.00%		29.8 g/mol
						Net Equivalent Weight
						4.00 g/cc
						estimated density

Figure A10: Average model composition and equivalents for the Hastelloy-oxide system in acidic solution.

Note in Figure A10 that the total number of electrons transferred from the base metal to the proposed metal oxide mixture are identical, as they should be. Identifying this value effectively permits estimation of the corresponding equivalent weights involved for both the base metal and its unique composite oxide. Also note that the metallic atomic concentrations in the oxide mixture are compliant with expectations via XPS, SIMS, Auger, etc... If the calculations were conducted utilizing strictly base metal compositions and the typical number of valence electrons one normally assumes, estimated equivalent weights for this metal would be on the order 23-25g/mol. However, the proposed approach provides equivalent weights which are unique to both the base metal and the composite oxide and which are connected by the net number of electron equivalents transferred between the two phases. This opens the door to more elaborate endeavors regarding oxide growth phenomena and passivation mechanics that are specific and exclusive to a given alloy under study. At present, estimation of electron and weight equivalents via oxide formation is complex, tedious and time-consuming. Even with the aid of Pourbaix and Ellingham diagrams, certain assumptions must be made and errors are likely without due diligence, but it is the correct way to determine the number of electrons transferred during the oxidation process.

Finally, note that most of the oxides of interest here are amphoteric in nature with pendant hydroxyl groups protruding along the surfaces prior to immersion into the acidic solution. Immediately upon immersion, these hydroxyl groups become protonated (positively charged) during formation of the electrical double layer (EDL). Then, as the EDL evolves, positive sites along the surfaces of the porous and barrier layers begin to attract anions that are present in the solution such as chlorides, sulfates, phosphates, carboxylates, urates, hydrolases, etc... These associations may comprise the outer Helmholtz plane or slip layer as steric hindrance increases diffusivity factors while disrupting access of reactants and products into the oxide/hydroxide macrostructures and ultimately to the base metal. This activity plays a role in the actual levels of specific secondary and tertiary oxides and oxyhydroxides that initially develop from each metallic component as it interacts with the solution.

#### **A.10 Model Development for Pitting Rates and Penetration Depths Over Time**

The variety of shapes, depths and surface openings characterizing pits are essentially infinite, and attempting to account for the density of pits across a given surface at any given time can make the measurement of pitting events even more complex. There is an abundance of resources available that cover pitting phenomena and several standards providing instruction pertaining to pit measurement and characterization (ASTM G46 provides an excellent description of pitting morphologies). Those concepts will not be explored here at this time. It is not the intent here to delve into all the intricacies of pitting science, but rather to explore a simplistic approach to envision how pitting rates and penetration/recession depths that might vary under certain circumstances, should pitting corrosion occur.

While general recession/oxidation rates sometimes appeared to be higher in the pretreat environment, pitting susceptibilities seemed to be more prominent in the brine solution. In all likelihood, this is a result of the higher chloride content in the concentrated brine media. It should be emphasized that under normal operating conditions, it is believed that pitting is highly improbable in either solution with any of these metal candidates, including Cronidur. The observed pitting on Cronidur samples during polarization testing occurred under aggressive and accelerated test conditions where damaging voltages were applied. While small voltages may simulate accelerated life conditions to a degree, higher voltages

tend to promote side reactions, degradation effects and anomalies not associated with actual corrosion events and would not occur normally occur under average field conditions.

Caution must be applied when interpreting pitting and repassivation information from the upper anodic regions of cyclic polarization curves. As presented in previous reports, the maximum achievable pitting recession rates can be extrapolated from the lowest possible slopes in the region following the breakdown point  $E_{Brk}$  prior the vertex (assuming the vertex is tailored into the test run appropriately). Additionally, relative time periods from  $E_{Brk}$  to the maximum pitting slope can be extrapolated from the scan data and are unique for each metal. In short, these extrapolated values become critical factors in simulating how pitting rates and recession depths might change or evolve over time. If pitting happens to initiate and sustained growth follows, what would the growth profile look like?

Early on, it was envisioned that pitting recession rates rise rapidly after initiation, reach a peak rate (that is, a maximum pitting rate) and then decline slowly to zero as oxide product increasingly blocks the pit entrances, while penetration/recession depths increase pseudo-parabolically over time and then level off at some maximum plateau. Hard field data has confirmed that this perception is indeed what happens. There are a number of published works over the last 40-50 years in which sample weight losses and penetration depths were physically measured at regular time intervals over several years. In particular, field data presented in a couple of interesting studies examining low alloy steels, stainless steels and an Inconel alloy were utilized for the work efforts in the current project. These results have revealed some very compelling curve forms or profiles describing the evolution of recession depths and rates over longer time periods which are believed to be characteristic of essentially all metals.

It has been established during these efforts that changes in penetration depths  $p$  over time  $t$  closely follow a modified exponential or Weibull-type function which starts out at zero and increases to a plateau as the maximum penetration depth is achieved and pitting ceases . . .

$$p_{pit} = p_{\infty} - a_1 \exp(-b_1 t^{c_1})$$

where  $p_{\infty}$  becomes the theoretical maximum pit depth attainable and  $a_1$ ,  $b_1$  and  $c_1$  are constants that control the shape of the profile. The time derivative of this function gives the penetration rate over time  $k_{pit}$  which ascends to a maximum rate under activation control and then decreases to zero under diffusion control. It has been found to closely correspond to a Hoerl power function . . .

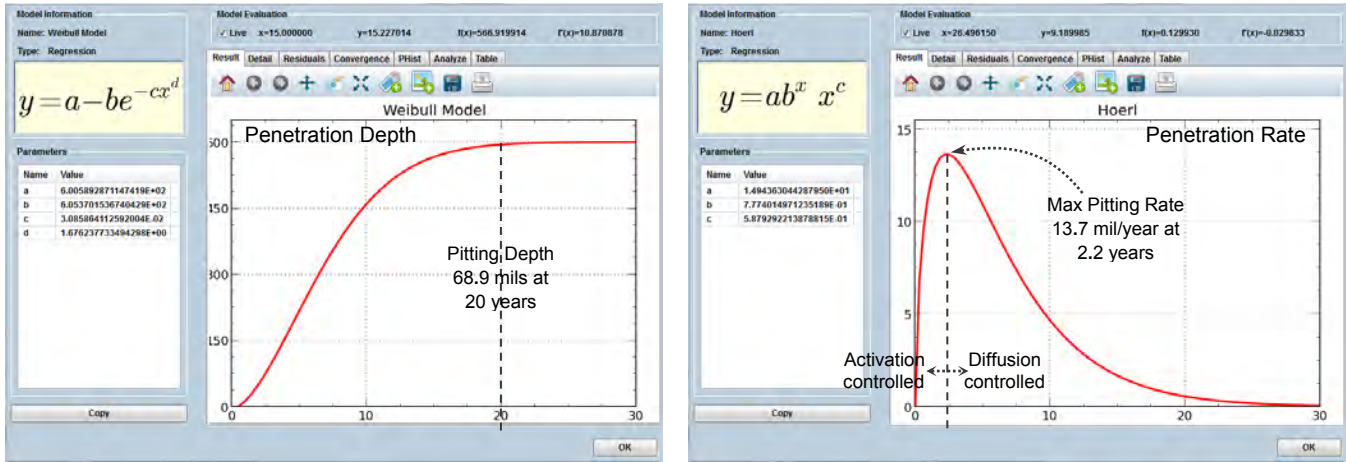
$$\frac{dp}{dt} = k_{pit} \cong a_2 b_2^t t^{c_2}$$

where  $a_2$ ,  $b_2$  and  $c_2$  are profile shaping constants.

Model profiles describing penetration depths and rates were established for each of the six metals in both test solutions utilizing the maximum pitting rate estimates and  $E_{Brk}$  times obtained from the polarization scans. In addition, average pitting shapes were based on conic-type volumes (for simplicity) which penetrate about 5 times deeper than general recession. These results are considered only to represent possible depths and rates in an unlikely worst-case scenario in which the repassivation protection

mechanism for each metal is overcome, inhibited or otherwise ignored. Graphical results for two of the subject metals are given in Figure A11 as examples of the technique applied to all candidates.

### Cronidur 30 in Brine



### Titanium LI in Pretreat

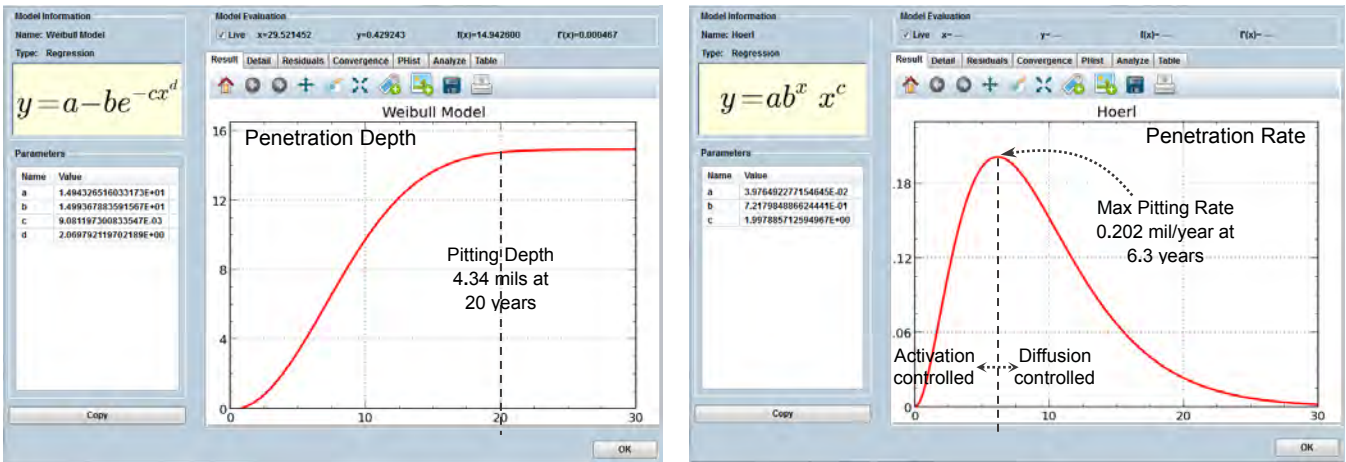


Figure A11: Example of modelled pitting penetration depths and rates for Cronidur 30 and Titanium LI.

Maximum penetration rates and the corresponding time periods estimated for six previously tested metals in Pretreat media were (1) Titanium CP: 0.181 mpy at 5.4 years, (2) Titanium LI: 0.202 mpy at 6.3 years, (3) Titanium 6-4: 0.268 mpy at 7.2 yrs, (4) Inconel 625: 2.47 mpy at 3.2 yrs, (5) Hastelloy C276: 2.08 mpy at 3,2 yrs, (6) Cronidur 30: 6.0 mpy at 2,5 yrs, and in Brine media, (1) Titanium CP: 0.326 mpy at 6.0 yrs, (2) Titanium LI: 0.296 mpy at 6.7 yrs, (3) Titanium 6-4: 0.332 mpy at 6.8 yrs, (4) Inconel 625: 3.19 mpy at 3.2 yrs, (5) Hastelloy C276: 3.67 mpy at 3.1 yrs, and (6) Cronidur 30: 13.7 mpy at 2.2 yrs (where mpy = mil/year).

It should be noted that the current corresponding directly with  $E_{Brk}$  on a typical Cyclic polarization plot can often be identified as the ‘metastable pitting current’ where pitting (metal recession) and repassivation (oxide regeneration) may be occurring simultaneously at the same opposing rates. Unfortunately, a correct interpretation of pitting rates cannot be obtained from some coincidental point

where the scan lines happen to intersect on a cyclic polarization plot. More importantly, there is no ‘average’, ‘stable’ or ‘constant’ pitting rate and there is no single value that represents the pitting rate because . . . pitting rates are always changing! A pitting rate life cycle goes from zero up a long ramp over time, through a momentary maximum, and then back down over even longer ramp to an asymptotic zero. In a cyclic run, pitting rates vary from a low metastable condition around  $E_{Brk}$  to a maximum rate somewhere from 0.05-0.5V beyond  $E_{Brk}$ . In real world situations, after pits have initiated and the conditions are favorable for continued (sustained) pitting, rates increase exponentially, reach a peak (a maximum pitting rate  $I_{Pit,Max}$ ) and then gradually diminish to zero as corrosion products fill the pit volume and diffusional blockage eventually inhibits further reactions into the active pit area.

### A.11 Increasing Solution pH Over Time

What happens when a passivating metal is immersed in an acidic solution and why does the pH increase over time? Prior to immersion, these metals develop very thin, highly protective oxide layers on their surfaces within seconds after fresh machining, surfacing or etching as peripheral metal atoms rapidly interact with atmospheric oxygen. Typical layer thicknesses are 2-5 nanometers. Transition zones comprise the bondlines between metal substrate and oxide layer. For a constant environment, the process is self-limiting as O<sub>2</sub> molecules diffuse through the oxide structure where they oxidize Cr atoms leading to inward recession of the base metal and inward/outward growth of the oxide phase. A simple illustrated of passivation in air is given in Figure A12.

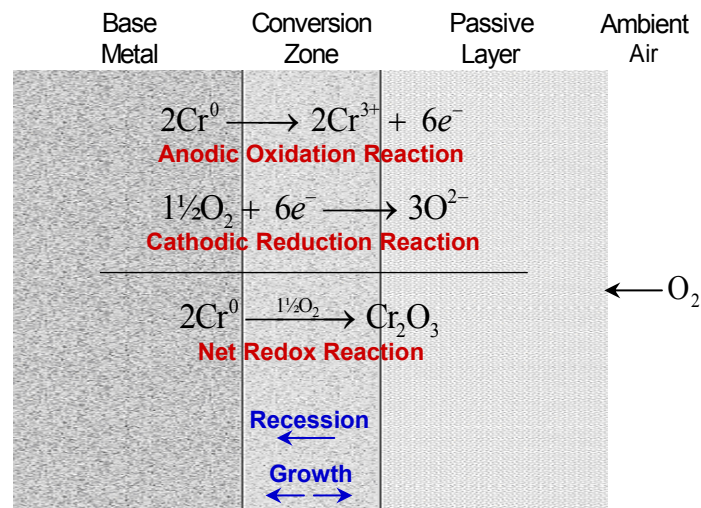
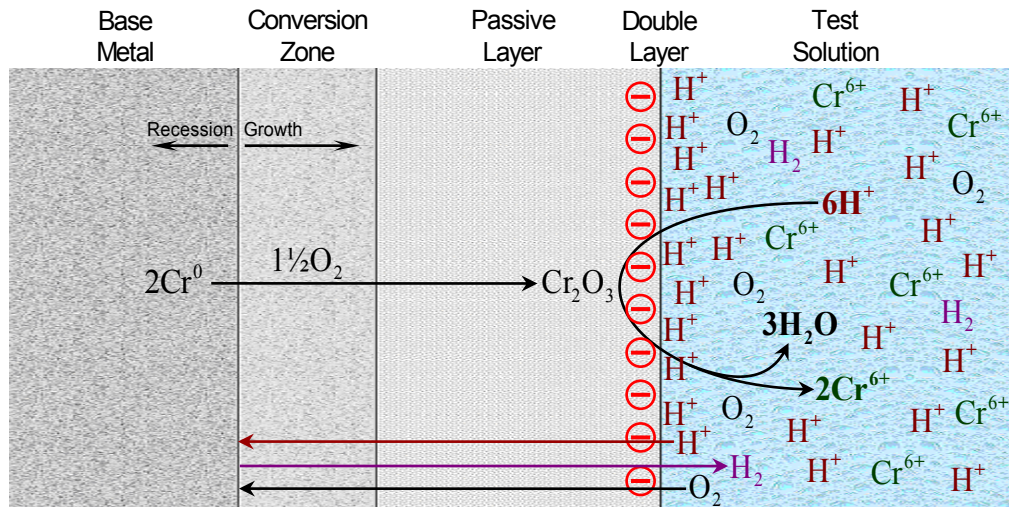


Figure A12: Simplified depiction of passive layer formation on a chromium alloy in air.

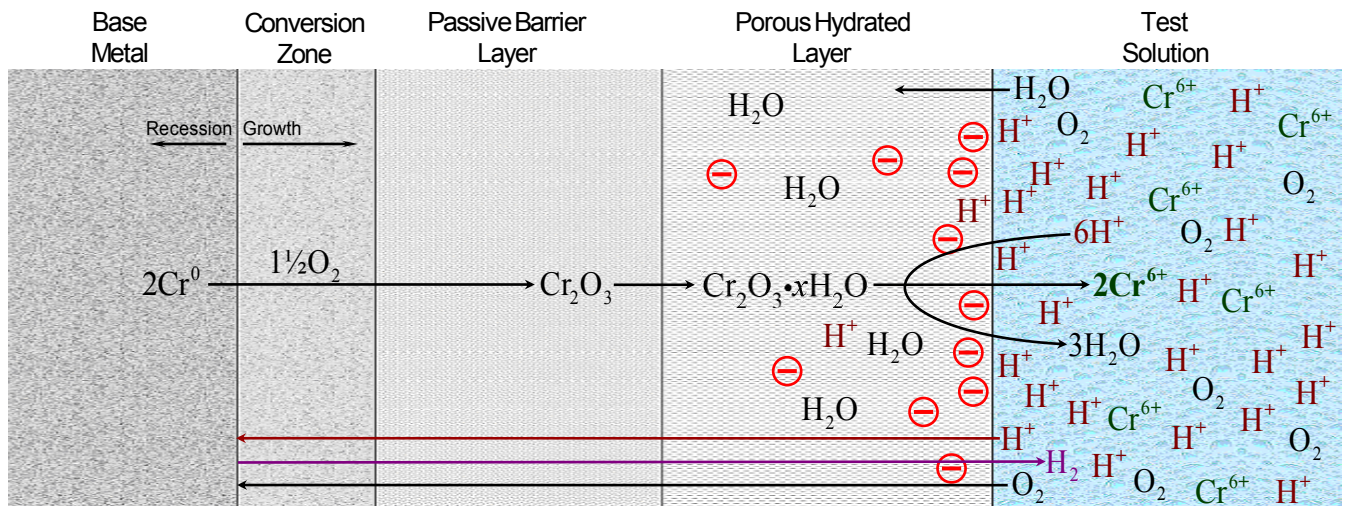
Upon immersion in electrolytic media, an electrical double layer (EDL) quickly forms as the oxide surface adapts to the new environment. In addition, oxygen-rich, acidic media begins to slowly dissolve the oxide layer while Cr<sup>6+</sup> ions are ejected into the solution and H<sup>+</sup> ions are reduced to H<sub>2</sub>, which bubbles away. This more advanced situation is shown in Figure A13.





A13: Illustration of a passivated chromium alloy a few seconds after immersion in an acid electrolyte

In response, the oxide regenerates itself very quickly and it also develops a thick, porous, hydrated layer on the outside facing the solution which tends to generalize the EDL across space. The system remains neutral throughout. This is depicted in Figure A14.



A14: Illustration of a chromium alloy several minutes after immersion

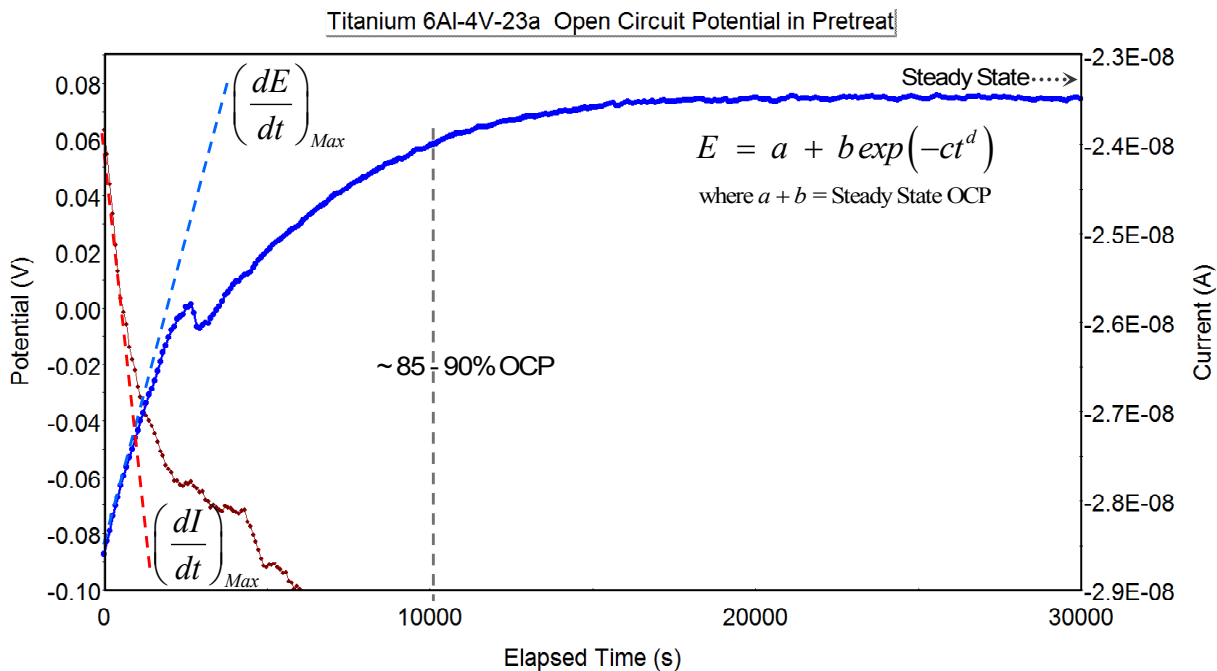
Relevant reactions include (A) anodic oxidation of the base metal (resulting in metal recession and oxide growth), (B) cathodic reduction of hydrogen ions  $H^+$  to  $H_2$  in the local solution, and (C) dissolution of the metal oxide. All three reactions eventually reach equilibrium along a plateau at Steady State where  $k_A \Gamma k_B \Gamma k_C$ . During the reduction and dissolution reactions,  $H^+$  ions are consumed to form molecular  $H_2$  and water as shown in reactions B and C. The  $H_2$  bubbles away as a gas while  $H^+$  ions are depleted. Thus,

the concentration of  $H^+$  ions in the solution decreases as the passive layer dissolves and replenishes. The rates for hydrogen reduction and oxide dissolution are both kinetically-favored. However, these reactions are attenuated due to the diffusion-controlled rate of oxidation in the metal-oxide conversion zone as reactants and products must travel through the nonporous oxide barrier to reach the metal surface. It should be noted that in a large, flowing ECLSS reservoir, slight pH changes would likely be trivial. In contrast, the small test bins used in our experiment were configured to contain minimal amounts of test solution and the exposure was conducted under entirely stagnant conditions at room temperature. In this case, the pH drop is expected to be more noticeable. Due to its high viscosity, reactions within the concentrated stabilizer will tend to be diffusion-limited while those in the diluted version will tend to be kinetic-controlled.

Dispersed charges in the growing conductive porous layer decrease the capacitance of the system while contributions associated with the insulative barrier layer (primary barrier) become negligible. The differential capacitance can be defined as a function of the change in charge build-up at the EDL interface,  $dq = Idt$ , to the change in voltage  $dE$  and is inversely related to the thickness  $L$  of the coating (roughly) which is comprised mostly of the porous layer . . .

$$C_d = \frac{Idt}{dE} \propto \frac{1}{L}$$

Initial slopes in the original Open Circuit Potential plot may provide clues regarding the relative growth rates for these two layers. As an example, consider the plot given in Figure A15. At the onset, the relative rate of the porous layer (as reflected by  $dE/dt$ ) increases substantially at the expense of the primary barrier layer (indicated by  $dI/dt$ ).



A15: Example Open Circuit Potential curve obtained from previous studies.

## A.12 Special Method for Estimating Corrosion Susceptibilities

The concepts of susceptibility defined for this study are rudimentary and should be considered as extensions to the topics covered in ASTM G102. They are purely creations of the author which seemed to work well for the current study. No guarantee is given regarding their validity, correctness or accuracy in any other application. Since these are evolving concepts at this point, it is perhaps best to consider all susceptibility definitions as ‘relative’ to the group of metals under evaluation in this study.

Before the porous layer precipitates and coats the solution-oxide surface, an electrical double layer (EDL) develops which contributes the majority of the capacitance exhibited by the combined surface layers. As the porous layer grows and widens, contributions from the EDL capacitance decrease, and when positive (anodic) voltage is applied, the EDL charges up as the capacitance increases. Now the barrier oxide layer itself also produces a small capacitance due to the separation of charges at the barrier-porous interface and charges along the metal surface (or within the conversion zone) with the barrier oxide acting as the dielectric. Generally, the oxides studied here are all ceramic dielectric insulators, but most of them exhibit point defects characteristic of *n*-type semiconductivity where cation interstitials ( $\text{Cr}_i^{3+}$ ,  $\text{Ti}_i^{4+}$  and  $\text{Fe}_i^{3+}$ ) and oxygen vacancies ( $V_{O''}$ ) become the primary charge carriers leading to metal ion ejection into the solution as hydrolytic dissolution takes place. When the applied voltage exceeds a threshold voltage, which is generally prior to the breakdown potential  $E_{Brk}$ , the behavior transitions over to *p*-type conductivity. Beyond  $E_{Brk}$ , conduction may occur by tunneling or avalanche effects (nickel oxide NiO itself is a *p*-type conductor throughout and will be addressed later).

During open circuit exposures and external polarization fields, the dielectric barrier layer evolves in thickness along with corresponding changes in barrier layer capacitance  $C = q/E_{App} = \epsilon_0 \epsilon_r A/t$ , surface charge density,  $\sigma = q/A = \epsilon_0 \epsilon_r E_{App}/t$  and electric field strength,  $\mathcal{E}_{Pol} = \sigma/\epsilon$  (in accordance with Gauss’ law). Here,  $q$  is the charge transferred from the base metal to the oxide to the solution,  $E_{App}$  is the applied test voltage (the potential difference across the oxide),  $A$  is the sample test area (fixed at 1 cm<sup>2</sup> throughout),  $t$  is the barrier layer thickness,  $\epsilon_0$  is the vacuum permittivity constant and  $\epsilon_r$  is the relative permittivity of the oxide (that is,  $\epsilon_r$  is the dielectric constant of the oxide while  $\epsilon_0 \epsilon_r = \epsilon$  is the absolute permittivity).

Now recognize that  $\mathcal{E}_{Pol} = \sigma/\epsilon = CE_{App}/A\epsilon$ , or  $E_{Pol}\epsilon = CE_{App}t/A$ , from which a representative breakdown indicator specific to that oxide layer can be envisioned. The product  $E_{Brk} \cdot \epsilon_r$  carries a special significance indicating the tendency of the oxide to resist the breakdown forces and protect itself by virtue of its inherent properties. The value of the breakdown potential  $E_{Brk}$  provides information regarding the propensity of the oxide to fail with subsequent pitting into the base metal, while  $\epsilon$  is a relative indicator of the oxide’s dielectric capability. If both of these factors are high, there is a very low probability that the oxide will succumb to the breakdown forces. One factor can compensate for the other. If one is high and the other low, the oxide can still be protected. But if both factors are low, the susceptibility is high and breakdown is imminent. To be more proper, consider the height of  $E_{Brk}$  above another potential of interest, say the primary passivation potential, that is . . .  $(E_{Brk} - E_{Pas})\epsilon_r$ . This is reasonable since the greater the voltage difference between  $E_{Brk}$  and  $E_{Pas}$ , the lower the propensity that breakdown will occur. Conversely, an argument can be made regarding the repassivation potential, since the higher and closer it is to  $E_{Brk}$ , or rather the smaller the difference between  $E_{Brk}$  and  $E_{Rep}$ , the higher the chance that repassivation will protect the recovering metal surface, that is . . .  $(E_{Brk} - E_{Rep})/\epsilon_r$ . These insights are consistent with real world perceptions and are in accordance with recognized interpretations of cyclic polarization curves.

In a more comprehensive and decorous approach it is proposed that the relative susceptibilities for the initiation (nucleation) and sustainment (unabated growth) of pitting can be represented respectively by the following arguments . . .

$$(E_{Brk} - E_{Pas})\epsilon_r \quad \text{and} \quad (E_{Brk} - E_{ReP})\epsilon_r^{-1}$$

Formal definitions can then be proposed for the relative susceptibilities to Pitting Initiation  $S_{PiI}$  and Pitting Sustainment  $S_{PiS}$  in exponential form, respectively . . .

$$S_{PiI} = 1 - \exp\left[\left((E_{Brk} - E_{Pas})\epsilon_r\right)^{-1}\right] \quad \text{and} \quad S_{PiS} = 1 - \exp\left[\left((E_{Brk} - E_{ReP})\epsilon_r^{-1}\right)^1\right]$$

Thus, when  $S_{PiI}$  is low,  $E_{Brk}$  and  $E_{Pas}$  are far apart, and when  $S_{PiS}$  is low,  $E_{Brk}$  and  $E_{ReP}$  are close together. Likewise, the higher the relative permittivity constant for a given oxide  $\epsilon_r$ , the lower the susceptibility. Figure A16 shows example susceptibility plots for three of the subject test metals which indicates the stark differences between these metals in terms of pitting initiation. Delta potentials for Cronidur in pretreat solution ranged from about 0.5 to 1V while those of Inconel ranged from about 0.7 to 1.1V and for Titanium CP, 1.4 – 1.7V. These potential ranges are numerically descriptive of the estimated susceptibilities for each of the metals and are emphasized in Figure A16. As one might expect, the Titanium metals possess strong protection mechanisms across the board, especially in the measured test range, while Cronidur appears to exhibit an elevated level of susceptibility towards pitting, and the Inconel samples indicate susceptibilities that are in between but closer to Cronidur. These results were also reflected in the actual data summary and results for those studies.

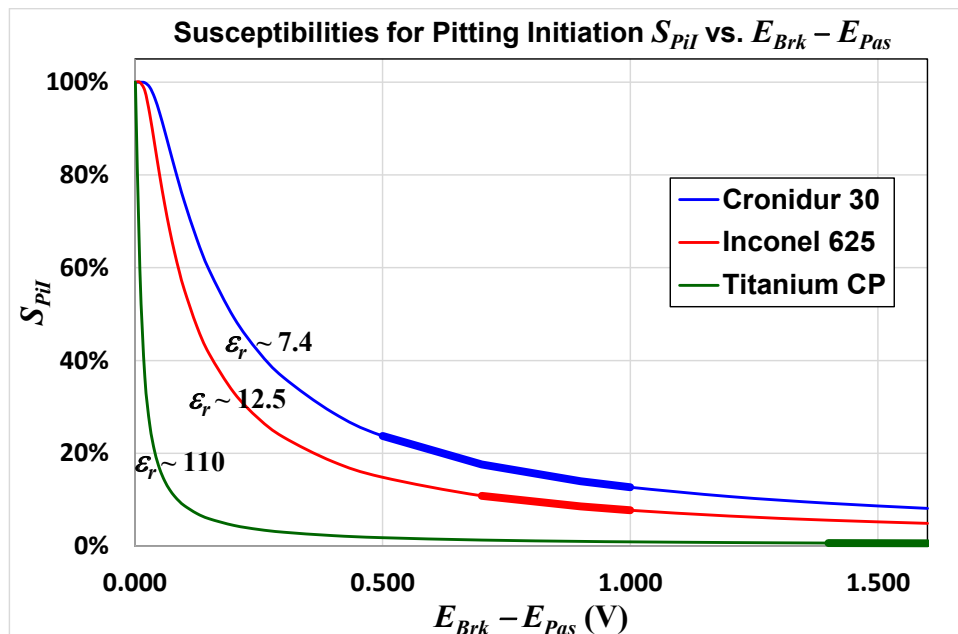


Figure : .

Figure A16: Pitting initiation plots for three of the test metals in pretreat showing the respective active areas.

For further consideration, consider two contrasting cases taken from typical Titanium and Cronidur cyclic runs obtained during previous studies. These are depicted in Figures A17 and A18 which illustrate a few key factors associated with susceptibility, hysteresis and semi conductivity.

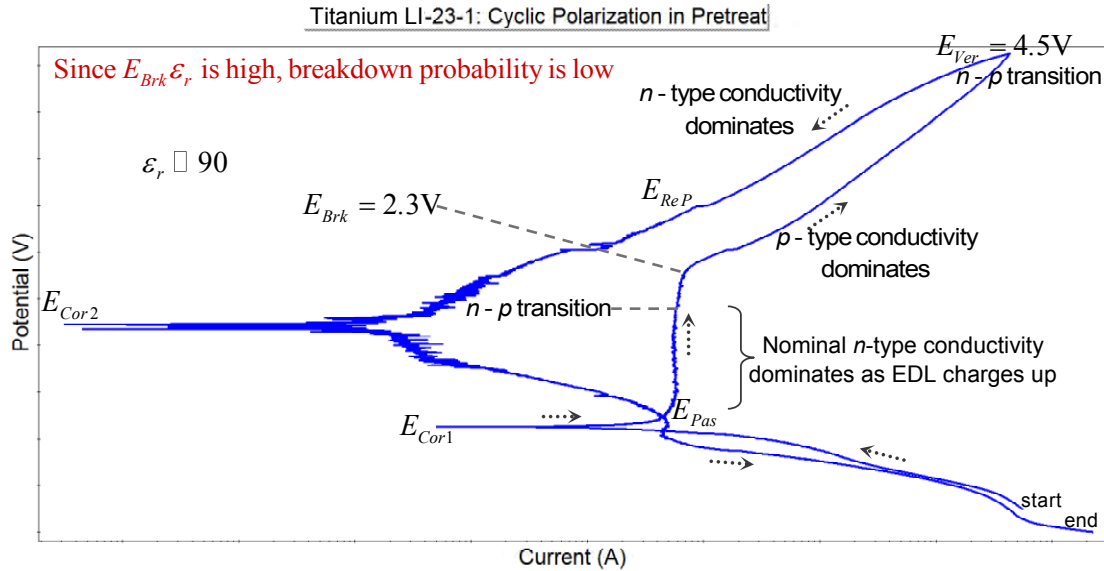


Figure A17: Cyclic plot for Titanium LI showing possible relationships between conductivity and susceptibility.

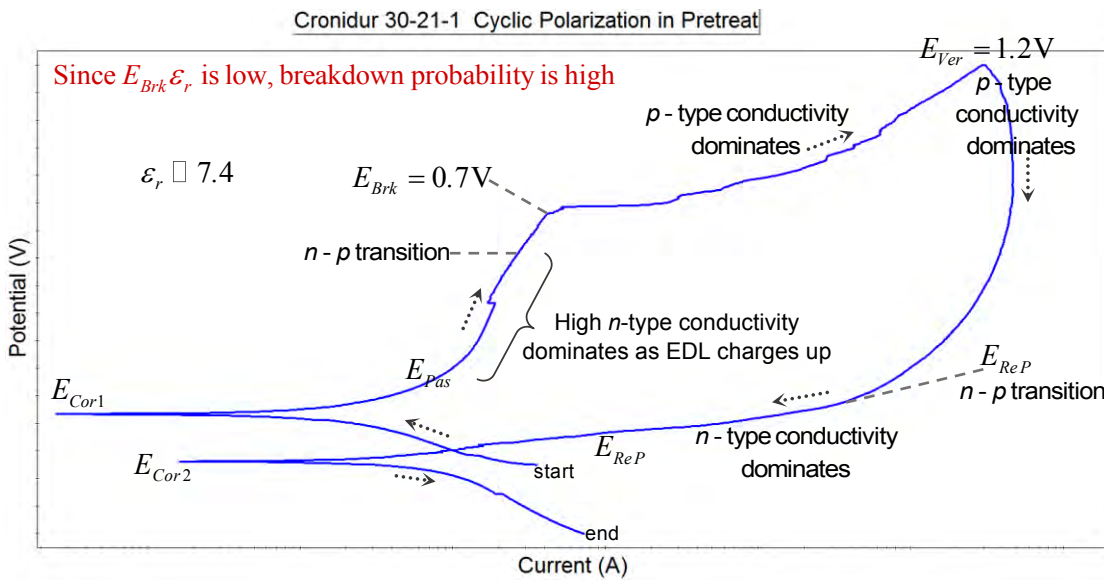


Figure A18: Cyclic plot for Cronidur 30 showing possible relationships between conductivity and susceptibility.

After the potential changes polarity (from cathodic to anodic) at  $E_{Cor1}$ , the passivation rate accelerates. When most of the growth is complete at  $E_{Pas}$ , the curve passes ‘onto the passive plateau where  $n$ -type conductivity accommodates the charge accumulation along the EDL. At the threshold voltage, conductivity switches from  $n$ -type to  $p$ -type as metal cations are ejected into the solution and cation vacancies become the major charge carriers. After  $E_{Ver}$ , oxide regeneration is accompanied by restoration of  $n$ -type conduction. The greater the regions of  $n$ -type behavior during anodic charging, the lower the corresponding  $S_{Pil}$ , and the smaller the  $n$ -type range during anodic discharging, the lower the  $S_{PiS}$ .

The methods outlined earlier for estimating  $S_{Pil}$  and  $S_{PiS}$  can be extended to provide similar representations possibly representing general corrosion susceptibility pertaining to  $E_{Cor}$  by making use of certain thermodynamic equivalences. Again, standard values for the Gibbs free energy change of formation  $\Delta G_f^0$  have been utilized for each component comprising the passive oxide layers on the metals evaluated. From these results, complex averages were developed for each composite oxide, all of which are part of the special materials property database developed for this study. With this approach, the relative susceptibility for general corrosion during OCP measurements and Linear polarization analysis can be roughly estimated . . .

$$S_{Cor} = 1 - \exp \left[ \left( (E_{Cor} - E_f^0) \varepsilon_r \right)^{-1} \right]$$

where  $E_f^0$  is the corresponding potential change associated with the free energy change of formation  $\Delta G_f^0$  which follows from the Nernst equation, that is . . .  $G_f^0 = -nFE_f^0$ .

Values for  $S_{Cor}$  were provided earlier in the report when the data for OCP and Linear/Tafel analysis was presented. During analysis of the galvanic couple configurations, differences between the couple potential  $E_{OCG}$  and original open circuit potential  $E_{OCI}$  were computed utilizing the factor  $(E_{OCG} - E_{OCI})\varepsilon_r$ . Overall, while these susceptibility concepts may seem simplistic, they appear to have work quite well for these studies, providing good representations of the relative corrosive tendencies for each test metal as they combine inherent material properties with actual test data. For informational purposes, average values developed for the dielectric constants and the Gibbs free energy potentials associated with each of the composite oxides examined in this study are given in Table A1.

Table A1: Average representative values utilized for  $\varepsilon_r$  and  $\Delta E_f^0$  during estimation of relative susceptibilities.

	Inconel 625	Hastelloy C276	Titanium CP	Titanium 64	Titanium LI	Cronidur 30
$\varepsilon_r$	12.46	11.43	110.0	90.22	90.40	7.38
$\Delta E_f^0$	-2.68 V	-2.35 V	-2.91 V	-3.17 V	-3.18 V	-2.89 V

### A.13 Passive Films as Pseudo-Capacitors and Semiconductors

Several models have been developed to describe the oxide growth process on passive metals including the High Field Model, the Place Exchange Model and the Point Defect Model. Of these, the Point Defect Model (PDM) developed by D.D Macdonald appears to account for all the experimental observations regarding the structure and behavior of passive films. The methodologies and calculations involved in the PDM are intensive, and it is beyond the scope of this paper to present all the associated concepts here. However, for qualitative purposes, it will be interesting to explore some of the possible reactions responsible for the conduction of ions across the oxide layer as well as growth and dissolution of the layer itself. A representative scenario is illustrated in Figure A19 utilizing chromium as an example and making use of Kröger-Vink notation.

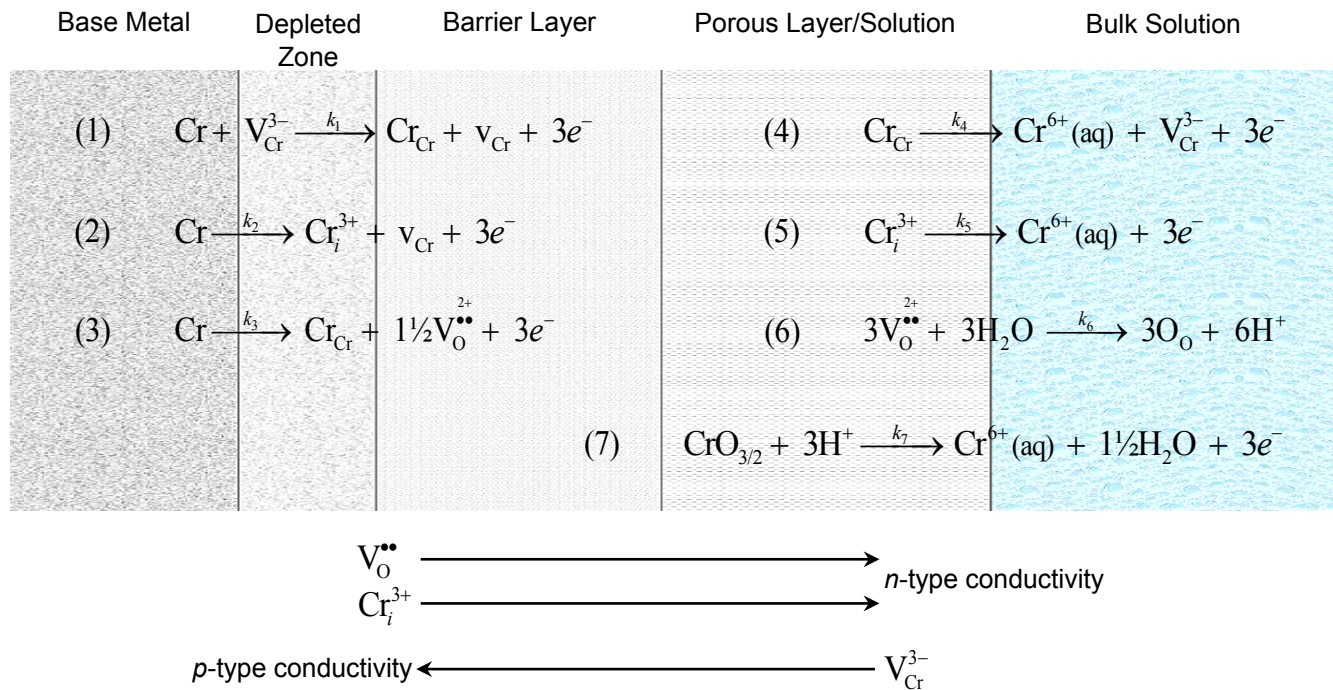


Figure A19: Possible reactions for a chromium substrate leading to conduction, oxide production and dissolution. Cr = metal atom in base metal,  $\text{V}_{\text{Cr}}^{3-}$  = cation vacancy in oxide lattice,  $\text{Cr}_{\text{Cr}}$  = metal cation at cation site in oxide lattice,  $\text{v}_{\text{Cr}}$  = vacancy in base metal,  $\text{Cr}_i^{3+}$  = interstitial cation in oxide lattice,  $\text{V}_\text{O}^{2+}$  = oxygen vacancy in oxide lattice,  $\text{Cr}^{6+}(\text{aq})$  = fully oxidized metal cation in solution,  $\text{O}_\text{O}$  = oxygen anion in oxygen lattice, and  $\text{CrO}_{3/2} = \frac{1}{2} \text{Cr}_2\text{O}_3 = \text{Cr}_{\text{Cr}} + 1\frac{1}{2} \text{V}_\text{O}^{2+}$ .

The theory is based on the activity of Schottky point defects associated with *n*-type conductivity as described by reactions (2) and (5), and reactions (3) and (6), and Frenkel point defects associated with *p*-type conductivity as described by reactions (1) and (4). Furthermore, transmission of ions through the barrier layer are inferred to occur exclusively by the motions or fluxes of vacancies and interstitials which are created at one of the interfaces (either the metal-oxide interface or the oxide solution interface) and then annihilated or depleted at the opposite interface. The nonconservative reactions (3) and (5) lead to growth and dissolution of oxide respectively and are responsible for movement of the oxide boundaries. At steady state, certain reactions are in equilibrium, that is,  $k_1 = k_4$ ,  $k_2 = k_5$  and  $k_3 = k_6 = k_7$ .

The barrier layers on Cronidur, Titanium and its alloys are known to exhibit *n*-type conductivity at lower potentials and then transition to *p*-type at some point just prior to  $E_{Brk}$ . This implies that conduction across these oxides is accomplished by the movement of oxygen vacancies  $V_O^{\bullet\bullet}$  (or holes) and cation interstitials  $Cr_i^{3+}$ , both of which become electron donors that are annihilated (or depleted) at the solution interface. However, in the nickel-based alloys Inconel 625 and Hastelloy C276, the nickel oxide (NiO) component behaves as a *p*-type conductor throughout and is characterized by the movement of cation vacancies  $V_{Ni}^{2-}$  which become electron acceptors that would be depleted at the metal interface. If phase separation happens to occur between the  $Cr_2O_3$  and NiO fractions, a *p-n* heterojunction is established along their common interface. This phenomena is explored further in the next section.

#### A.14 Anomalies on Nickel Alloys under Extreme Test Conditions

During previous testing in ECLSS brine solutions, some of the Inconel and Hastelloy samples exhibited unusual effects during abnormal cyclic polarization in pretreat media when cyclic starting voltages were significantly cathodic (negative). Some of the test samples were pre-conditioned at strong negative potentials during the beginning of the cyclic scan in order to test the extremes and to explore the possible ramifications. Figure A20 gives an image of one of the Hastelloy samples evaluated during these prior tests which was conditioned at  $-0.75V$  for five minutes at the beginning of the cyclic polarization scan. Observational notations are also given.

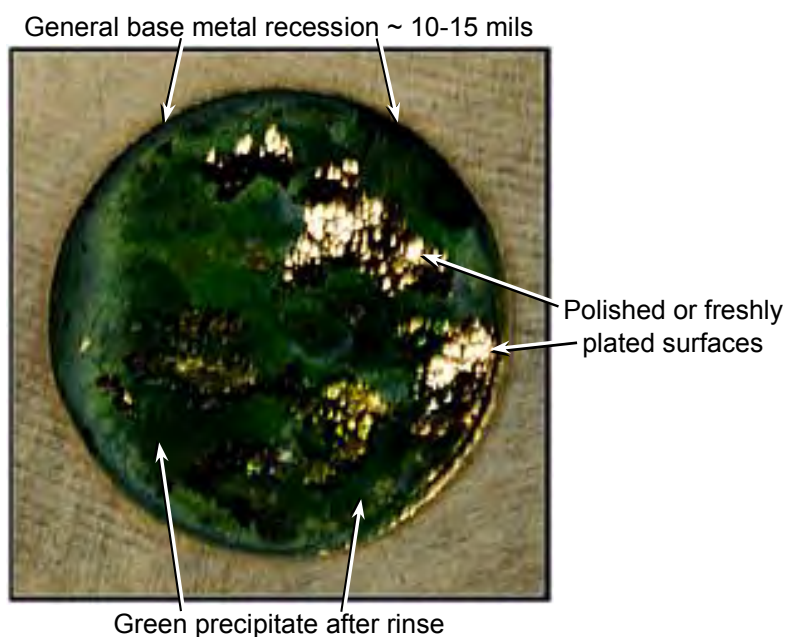


Figure A20: Hastelloy sample surface after cyclic polarization scan in pretreat with  $-0.75V$  cathodic conditioning.

It should be realized that these types of results were obtained only under very extreme test conditions during exposure to brine solution concentrate. This could be related to the lower level of associated ion pairs in the fresh acid solution along with a condition of high activation-controlled access to the metal surface as compared to the viscous brine media in which chemical reactivity may be limited



by concentration diffusional effects. Testing showed that cathodic stripping can begin at potentials as high as  $-0.2\text{V}$ . Likely causes for the green precipitate will be addressed first.

It is suggested that at the end of the polarization scan, the concentration of dissolved nickel ions near the sample surface is very high. When the sample was quickly removed from the solution and gently rinsed in pH 7 water, regions of green precipitate remained. It was shown that continued rinsing and/or more aggressive rinsing would wash away these precipitated remnants. It is believed that the green precipitates are comprised of nickel hydroxide  $\text{Ni}(\text{OH})_2$ , nickel oxyhydroxide  $\text{NiOOH}$  and complexed nickel hydroxide/hydrates derived from the semi-organic brine test solution. While  $\text{Ni}(\text{OH})_2$  crystals are generally light-to-pale green in form, the organic complexes in this precipitate are believed to be responsible for the rich green appearance. Factors leading to recession of the base metal, electrolytic polishing and/or metallization ('back-plating) on the interim surface require a more intensive analysis.

In short, it is surmised that following cathodic stripping of the air-formed passive layer, anodic regeneration of the new passive layer facilitated migration, concentration and/or separation of the nickel oxide (NiO) phase toward the periphery of the layer placing it in direct contact with the solution. The NiO outer layer acted as a barrier to inward oxygen flow and begin to trap electrons within the  $\text{Cr}_2\text{O}_3$  core which underwent reduction (cathodic weakening of the crystal structure) until the outer NiO barrier layer failed at or after  $E_{Brk}$ . This condition exposed the unprotected base metal to the acid solution at high anodic voltage inducing rapid etching into the metal. Metallization effects could have been facilitated by the high concentration of  $\text{Ni}^{2+}$  ions local to the surface following the voltage reversal at  $E_{Ver}$ , and/or electrolytic polishing effects could have taken place during the repassivation process following  $E_{Rep}$ .

There are standard industry practices for stripping the passive layers from metal surfaces which can be performed under cathodic voltages or in acid solutions or both. Mixtures of phosphoric and chromic acid have been used for this purpose (same acids in the pretreat solution). Thus, it is reasonable to understand how cathodic conditioning prior to or at the beginning of a polarization scan can easily result in stripping of the passive layer. If left under cathodic control in an acid solution for very long, etching of the base metal will begin. In weak chromic/phosphoric etching solutions at  $\sim -0.75$  to  $-1\text{V}$ , the oxide layer may be completely stripped away in a matter of a seconds or minutes. After the passive layer anodically re-forms up to  $E_{Pas}$  and along the passive plateau, electrolytic polishing of the oxide surface may take place. Again, such concepts are common practice in the metal finishing industry.

Unfortunately, chemical analysis of the samples and Electrochemical Impedance Spectroscopy (EIS) were not conducted during these studies due to scheduling and cost constraints. Surface compositional analysis may have provided information regarding the nature and possible factors leading to formation of the observed products, while Mott-Schottky capacitance-potential plots obtained via EIS would have facilitated estimations of the respective charge carrier concentrations during the voltage sweep. Thus, the mechanisms proposed in the descriptions and explanations given in the following paragraphs are primarily hypothetical at this time.

A number of researchers have confirmed the formation of  $p-n$  type barrier bilayers under anodic conditions on nickel-rich alloys consisting of chromium oxide  $\text{Cr}_2\text{O}_3$  cores underneath nickel oxide NiO outer layers. Furthermore, it has been historically recognized that NiO films act as diffusion barriers, effectively preventing the inflow of reactive species. More recently, it has been experimentally

demonstrated that that NiO layers completely block the electrochemical reactions and the transmission of charge carriers in the depletion region. These findings help to corroborate the proposed theory.

In general, the subject metals with their passive layers are analogous to pseudo- $n$ -type Schottky diodes or barriers in which the oxides act as lightly doped  $n$ -type semiconductors due to the intrinsic impurities present from natural contaminants when the layer initially develops. Under steady state conditions, no current is drawn (the diffusion current and drift current are equal and opposite) but a small voltage drop is established across the metal-oxide junction, the so-called 'built-in' voltage  $V_{bi}$ . This is analogous to the larger galvanic potential difference exhibited between dissimilar metals which are in contact and is proportional to the difference between their work functions. The built-in voltage that electron energies must surpass in order to flow corresponds to the Schottky energy barrier height  $qV_{bi}$ . For a metal- $n$ -type interface or junction, the depletion region occurs only in the oxide phase which creates a space charge electric field where charges  $q$  can be stored and hence, a small level of pseudo-capacitance exists. When the passivated metal is placed in an electrolyte, an electrical double layer (EDL) forms and the capacitive space charge widens along with the depletion region as discussed earlier.

In a typical potentiodynamic scan, current is always flowing into the sample while electrons are always flowing outward. When the immersed sample is first subjected to a negative cathodic voltage, an excess of electrons flows outward weakening and disintegrating the initial passive oxide layer in the process as it dissolves in the acidic solution. If held too long in this region, general etching of the base metal will occur. As the potential is increased toward  $E_{Cor}$ , the number of excess electrons diminishes and finally goes to zero at  $E_{Cor}$ . When the applied potential begins to increase above  $E_{Cor}$  into the anodic region, valence electrons are then extracted from the metal as the oxide starts to re-form on the surface. As the anodic (positive) voltage continues to increase, the new oxide layer grows under a 'reverse bias' condition through  $E_{Pas}$  and into the passive region.

A reverse bias is imposed on the metal- $n$ -type junction since the energy barrier for current flow through the oxide layer is increased and the potential across the junction increases. Under this condition, the depletion region expands and the diffusion of electrons attempting to cross the junction is greatly reduced. As long as the applied reverse voltage is in effect and continuing to increase, the total potential across the junction continues to increase toward the built-in voltage while the electric field also increases. A small reverse saturation current is maintained during this segment of the process (for a while). The almost constant reverse current is sustained across the passive plateau as a nominal diffusion of charge carriers continues until the  $E_{Brk}$  region is approached. This is representative of the Titanium example given in Figure A21 which depicts four possible responses during anodic polarization of metals. With the Cronidur example in Figure A21, the diffusion current overwhelms the reverse current. For nonpassivating metals, there is no resistance to electron flow and the process is activation-controlled with ideal Tafel behavior. The nickel fraction in the passive layer of alloys such as Inconel and Hastelloy can produce some interesting effects not seen with the other metals.

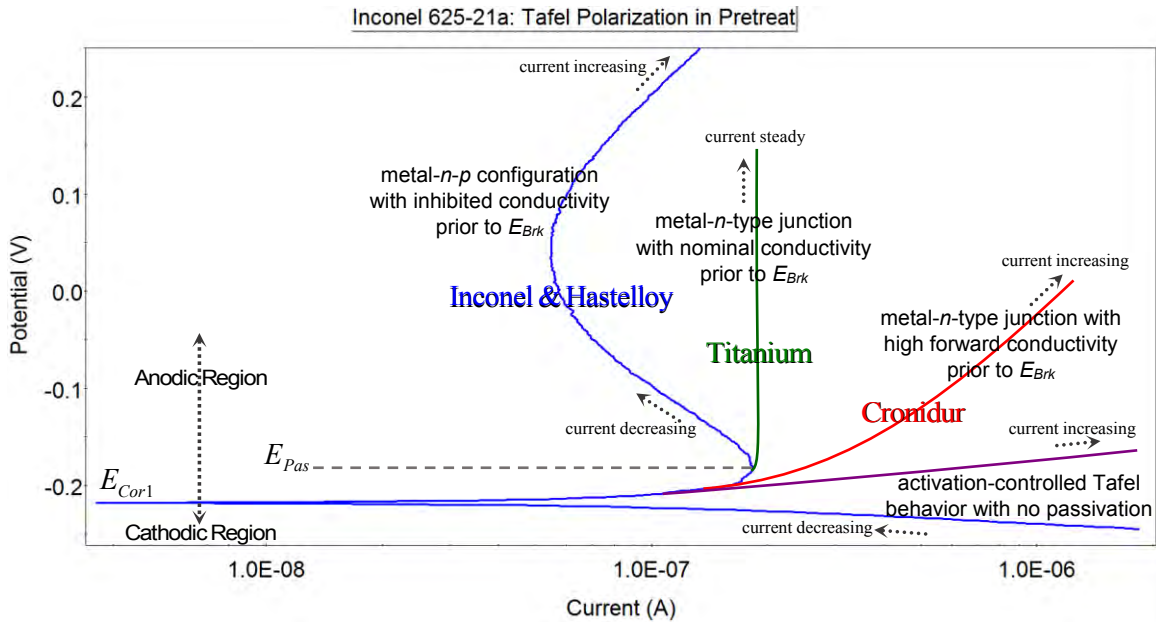


Figure A21: Illustration of possible polarization paths during and after primary passivation.

A couple of points should be emphasized here. The arrows indicate the direction of the scan. However, changes in the value of the current at any given time are not reflective of the direction that the current is flowing. As stated earlier, throughout all these polarization scans, current is always flowing into the sample while electrons are always flowing outward. This is due to the fact that the applied voltage drop across the cell is always forcing electrons to flow out of the sample. In cathodic regions (prior to  $E_{Cor1}$  and after  $E_{Cor2}$ ), excess conduction electrons are flowing outward while during the anodic segments (after  $E_{Cor1}$  and prior to  $E_{Cor2}$ ), valence electrons flow outward. For corroding metals, the current is generally increasing throughout the passive zone (however, forward current does not necessarily mean that corrosion is taking place). A steady current after  $E_{Pas}$  implies that the oxide layer is a tenacious semiconductor with a high  $E_{Brk}$  while an increasing current could infer a lower  $E_{Brk}$ . In single metal scans, particularly for rate estimation purposes, current values are always treated as positive quantities. Outside of the  $\pm 50\text{mV}$  linear range, the slope of the scan may be an indicator of whether the current is increasing or decreasing. In general, whenever the current is directed away from the log inflection point, it is increasing and whenever the current is directed toward the inflection point, it is increasing.

The polarization behaviors depicted in Figure A21 for Titanium and Cronidur are well substantiated. However, due to the high nickel content in Inconel and Hastelloy, conduction and electrochemical activity throughout the passivation region is quite different. The ‘bowing’ feature shown in this plot seems to be characteristic of high nickel alloys as it reflects the abrupt and opposite changes in current that occur after  $E_{Pas}$ . The degree of bowing has been seen to vary during different test runs with the largest exaggerations occurring for samples which were cathodically conditioned. While the other metals are known to exhibit single metal- $n$ -type Schottky junctions, the nickel alloys are believed to possess a multi-layer or multi-junction film which possess the characteristics of a bipolar metal- $n$ - $p$ -type barrier configuration. This feature is believed to be directly associated with the extent of phase separation that occurs within the  $\text{Cr}_2\text{O}_3$ -NiO layer.

While Cr<sub>2</sub>O<sub>3</sub>-NiO bilayers likely form to some degree in almost all electrochemical situations, the effects of cathodic conditioning appear to exacerbate the phase separation process as indicated throughout this work. Under ambient conditions, undoped NiO is more of an insulator than a semiconductor with a resistivity on the order of 10<sup>-13</sup> Ω-cm and very few charge carriers. These properties are key in determining the extent that NiO will behave as a diffusion barrier. Consider the activities illustrated in Figure A22 as a high Ni-Cr metal undergoes anodic passivation under reverse bias conditions.

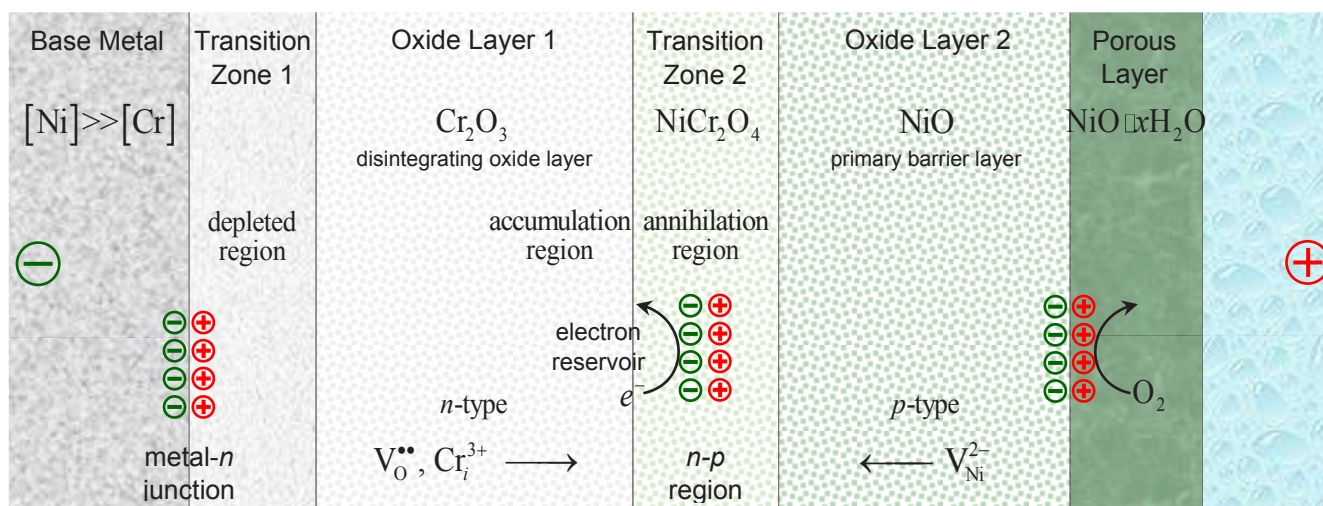


Figure A22: Illustration of possible processes during anodic passivation of Ni-Cr alloys under reverse bias.

The Ni-Cr substrate is highly conductive metal that provides a Schottky-type ohmic contact to the *n*-type Cr<sub>2</sub>O<sub>3</sub> oxide region (which includes Transition Zone 1 for the most part). However, the applied negative potential to metal side causes an increase in the energy barrier against electron flow through the metal-*n*-type junction into the Cr<sub>2</sub>O<sub>3</sub> layer. This leads to the accumulation of electrons on the other side of the Cr<sub>2</sub>O<sub>3</sub> layer. Transition Zone 1 is the gradient transition region between metal and oxide. Electrons are also depleted in this zone so creation of the primary charge carriers is restricted. As iterated earlier, the majority carriers in the *n*-region are electron donors which have been identified as oxygen vacancies V<sub>O</sub><sup>••</sup> and interstitial chromium cations Cr<sub>i</sub><sup>3+</sup> that flow toward Transition Zone 2. This zone is first created by reactions between Cr<sub>2</sub>O<sub>3</sub> and NiO during the initial passivation process, and it is shrinking as the NiO outer layer increases in thickness.

In the *p*-type NiO phase, the majority carriers are nickel cation vacancies which flow toward Transition Zone 2 from the other direction. Collisions between opposing charge carriers creates an annihilation region which prevents the flow of electrons into the NiO phase. Thus, inbound current and outbound electron flow are essentially cut off, similar to a *p-n-p* bipolar transistor in ‘cut-off’ mode where very little current flows. Since the number of donors and acceptors in both regions is severely limited, annihilation activity is minimal while an excess of electrons become trapped within the Cr<sub>2</sub>O<sub>3</sub> layer. In essence, the external NiO layer acts as a barrier, limiting the diffusion of oxygen from the outside and trapping the outflow of electrons from the inside. This condition creates a chemical reduction environment within the Cr<sub>2</sub>O<sub>3</sub> region that destabilizes the oxide structure with increasing detrimental effects as the

applied voltage continues to increase (analogous to cathodic disintegration). For additional clarity, Figure A23 gives the cyclic polarization semi-log scan for the sample depicted in Figure A20.

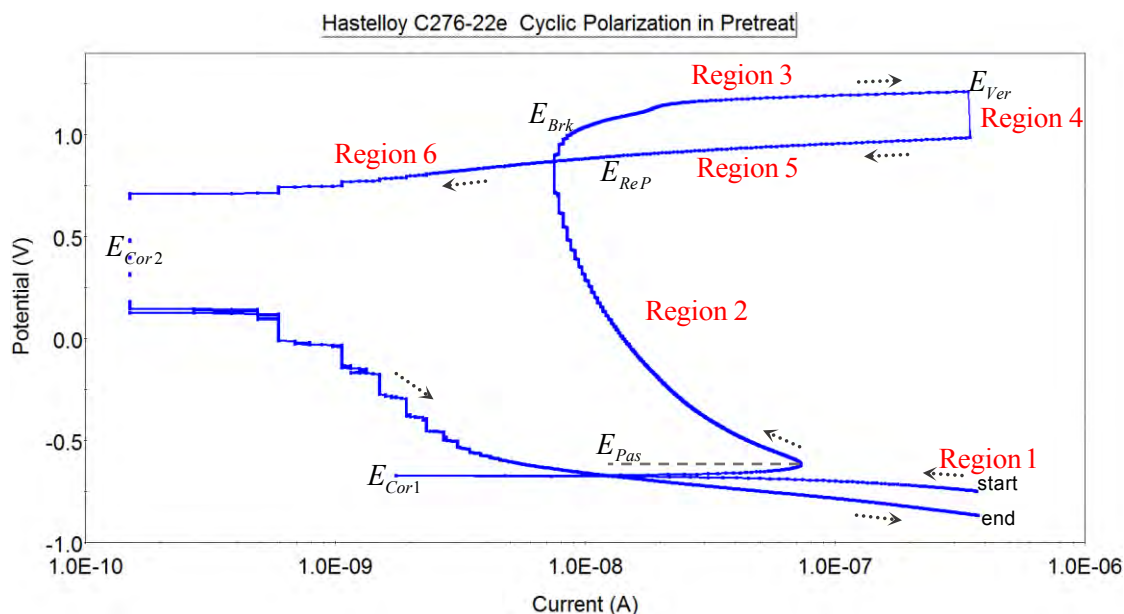


Figure A23: Cyclic polarization scan for the anomalous Hastelloy sample shown in Figure 35.

As iterated earlier, current is always flowing inward while electrons are always flowing outward. The arrows map-out the scan direction but they may also indicate the relative increases and decreases in electron flow. When polarization starts in the cathodic region, the sample is a positively charged cathode that is becoming less cathodic as the potential increases and approaches  $E_{Cor1}$ . At  $E_{Cor1}$ , the sample reverses polarity and becomes a negatively charged anode. For metals containing semiconductive passive layers, this corresponds to an applied reverse bias on the sample throughout the anodic branch. Forward bias occurs during the cathodic branches (prior to  $E_{Cor1}$  and after  $E_{Cor2}$ ) where reductive cathodic dissolution of the oxide layer is possible.

Region 1 in Figure A23 marks the beginning of this test at  $-0.75V$  just after constant cathodic conditioning was applied for five minutes. The applied potential (vs. Ag/AgCl) is negative in this region. It is suspected that most, if not all, of the original air-formed oxide layer was removed before the forward scan begin. At the start, there was an abundance of free electrons (excess conduction electrons) supplied by the power source. As the potential is increased, these electrons are rapidly ejected as  $E_{Cor1}$  is approached. At  $E_{Cor1}$ , the sample polarity reverses and becomes positive while all the excess electrons are depleted. As  $E_{Cor1}$  is surpassed, the current continues increasing while anodic oxidation (passivation) of the metal surface commences and valence electrons (bound atomic electrons) begin to flow outward. The specific value of  $E_{Cor}$  attained is unique to the metal and its interaction with the particular solution. Between  $E_{Cor1}$  and  $E_{Pas}$ , the  $Cr_2O_3$  layer begins to form almost immediately followed by formation of the  $NiCr_2O_4$  and  $NiO$  layers. Under increasing reverse bias conditions, the actual time lapse between development of the Cr-rich sublayer and the Ni-rich outer layer is greatly reduced. By the time  $E_{Pas}$  is reached, a heavy Ni-rich layer has developed in the outer regions of the passive layer which leads to the 'bowing' effect seen on the plot.

In Region 2, just beyond  $E_{Brk}$ , the current decreases as the applied voltage continues to increase up to the threshold potential just prior to  $E_{Brk}$ . This indicates that the outflow of electrons has become blocked by the outer NiO barrier. Additionally, the NiO layer inhibits the inflow of oxygen from the outside which reduces the passivation reactions at the metal substrate and essentially ‘cuts off’ the growth of protective  $Cr_2O_3$ . This imposes strong reduction forces on the  $Cr_2O_3$  layer as the outer NiO layer then becomes the primary protection barrier. The NiO layer is essentially acting as a MOS capacitor. Accumulation of electrons in the  $Cr_2O_3$  layer leads to a condition where the  $Cr_2O_3$  structure becomes cathodically weakened. As the potential continues to increase toward the threshold point, the shielded  $Cr_2O_3$  lattice likely undergoes chemical reduction and possibly cathodic weakening. Mobile chromium particles and oxygen may be produced in this space prior to  $E_{Brk}$ .  $Cr_2O_3 \longrightarrow Cr^0 + 1/2O_2\uparrow$ , and outgassing may increase the pressure inside the volume beneath the NiO layer. For this particular run, the intersecting scan lines happen to correspond roughly to both the threshold potential and the repassivation potential  $E_{ReP}$ .

The indicated breakdown potential probably pertains to or is dominated by the NiO phase. At  $E_{Brk}$ , an abrupt increase in the current occurs as electrons begin tunneling through the layer followed by avalanche outflow. At the beginning of Region 3 (i.e... at  $E_{Brk}$ ), anodic disintegration of NiO commences and nickel cations are ejected into the solution,  $Ni_{Ni} \longrightarrow Ni^{2+}(aq) + V_{Ni}^{2+} + 2e^-$ , as the NiO layer begins to break apart and dissolve in the acid,  $NiO + 2H^+ \longrightarrow Ni^{2+}(aq) + H_2O$ . Since the  $Cr_2O_3$  layer is depleted when the NiO layer ruptures and dissolves, the base metal is instantly exposed to the highly anodic acid solution. Throughout Region 3 ( $E_{Brk}$  to  $E_{Ver}$ ), rapid and aggressive etching of the base metal takes place which temporarily overwhelms the metal’s repassivation protection mechanism,  $Ni^0 + 2H^+ \longrightarrow Ni^{2+}(aq) + H_2\uparrow$  and  $Cr^0 + 6H^+ \longrightarrow Cr^{6+}(aq) + 3H_2\uparrow$ . Etching ceases at  $E_{Ver}$  (the relief point) where the increasing voltage ramp reverses and begins to decrease.

The short vertical segment depicted by Region 4 reflects a small time period, just before repassivation begins, when the current change is almost nil. Due to the heavy concentration of  $Ni^{2+}$  ions in close proximity to the surface, it is possible a small degree of metallization or back-plating may have occurred. Once repassivation initiates, this very thin, shiny Ni deposit would be stabilized. Regions 5 and 6 represent the reactions associated with repassivation, oxide regeneration and recovery of the Ni-Cr surface. Recall that  $E_{ReP}$  is the point where the repassivation rate rapidly starts tapering off. It is usually not visible on the log plot but is quite pronounced on the normal plot. It has been observed with these metals that after the voltage ramp reverses, repassivation is usually swift and powerful. Along Region 5, new oxide is rapidly being deposited, and then following  $E_{ReP}$ , electrolytic polishing of the surface may take place which could also impart a shiny appearance as seen in the photo. Positively charged Ni complexes and hydrates saturate the adjacent solution within the Nernst layer. They are attracted to and neutralized along the negative oxide surface. At  $E_{Cor2}$  (the polarity reversal point), these products become loosely bound. Beyond  $E_{Cor2}$ , the damaged sample area is completely covered with new oxide and green Ni precipitates as it becomes increasingly more cathodic until the scan ends. While there is no solid corroborating evidence to support this scenario at this time, it does explain the observed phenomena to a reasonable degree.

## References

1. “ECLSS Sustaining Metal Materials Compatibility Final Report, Electrochemical and Crevice Corrosion Test Results”, R.E. Lee, NASA/CR—2015–218208, April 2015, Contract NNM12AA41C
2. “ECLSS Sustaining Metal Materials Compatibility Final Briefing, Electrochemical and Crevice Corrosion Test Results”, October 6, 2014, Randy Lee
3. “Corrosion Protection for Space Flight Hardware”, NASA Technical Standard NASA-STD-6012, March 8, 2012

REPORT DOCUMENTATION PAGE			Form Approved OMB No. 0704-0188		
<p>The public reporting burden for this collection of information is estimated to average 1 hour per response, including the time for reviewing instructions, searching existing data sources, gathering and maintaining the data needed, and completing and reviewing the collection of information. Send comments regarding this burden estimate or any other aspect of this collection of information, including suggestions for reducing this burden, to Department of Defense, Washington Headquarters Services, Directorate for Information Operation and Reports (0704-0188), 1215 Jefferson Davis Highway, Suite 1204, Arlington, VA 22202-4302. Respondents should be aware that notwithstanding any other provision of law, no person shall be subject to any penalty for failing to comply with a collection of information if it does not display a currently valid OMB control number.</p> <p><b>PLEASE DO NOT RETURN YOUR FORM TO THE ABOVE ADDRESS.</b></p>					
1. REPORT DATE (DD-MM-YYYY) 01-11-2018		2. REPORT TYPE Contractor Report		3. DATES COVERED (From - To) August 2017-September 2018	
4. TITLE AND SUBTITLE  ECLSS Universal Waste Management System (UWMS) Metal Materials Compatibility Study Elgiloy: Electrochemical and Crevice Corrosion Evaluation			5a. CONTRACT NUMBER NNM12AA41C		
			5b. GRANT NUMBER		
			5c. PROGRAM ELEMENT NUMBER		
6. AUTHOR(S)  R.E. Lee			5d. PROJECT NUMBER		
			5e. TASK NUMBER		
			5f. WORK UNIT NUMBER		
7. PERFORMING ORGANIZATION NAME(S) AND ADDRESS(ES) Jacobs ESSSA Group/Bevilacqua Research Corporation Marshall Space Flight Center, Huntsville, Alabama			8. PERFORMING ORGANIZATION REPORT NUMBER M-1477		
9. SPONSORING/MONITORING AGENCY NAME(S) AND ADDRESS(ES) George C. Marshall Space Flight Center Huntsville, AL 35812			10. SPONSORING/MONITOR'S ACRONYM(S)		
			11. SPONSORING/MONITORING REPORT NUMBER NASA/CR-2018-220127		
12. DISTRIBUTION/AVAILABILITY STATEMENT Unclassified-Unlimited Subject Category 26 Availability: NASA STI Information Desk (757-864-9658)					
13. SUPPLEMENTARY NOTES Prepared for the Materials & Processes Laboratory, Engineering Directorate Technical Monitor: Jon Street					
14. ABSTRACT  Electrochemical evaluations were conducted on samples of Elgiloy in support of the materials compatibility program for the Environmental Control and Life Support System. Results were compared alongside three previously tested metals: Titanium 6Al-4V, Inconel 625, and Hastelloy C276. Titanium exhibited the best results of all the metals, indicating superior corrosive nobility and galvanic protection properties. Elgiloy demonstrated anti-corrosion behavior which appeared to be superior to the two nickel-chromium alloys. For this current effort, the results have clearly shown that Elgiloy possesses excellent corrosion protection properties and is galvanically compatible with the other three metals in the subject test media.					
15. SUBJECT TERMS corrosion, electrochemical, polarization, ECLSS, Elgiloy					
16. SECURITY CLASSIFICATION OF:			17. LIMITATION OF ABSTRACT	18. NUMBER OF PAGES	19a. NAME OF RESPONSIBLE PERSON
a. REPORT	b. ABSTRACT	c. THIS PAGE			STI Help Desk at email: help@sti.nasa.gov
U	U	U	UU	74	19b. TELEPHONE NUMBER (Include area code) STI Help Desk at: 757-864-9658





National Aeronautics and  
Space Administration  
IS02  
**George C. Marshall Space Flight Center**  
Huntsville, Alabama 35812

---